# REACTIVE REPLACEMENT AND ADDITION OF CATIONS IN BIOCLASTIC SILICA AND CALCITE

A Thesis
Presented to
The Academic Faculty

By

Shawn Michael Allan

In Partial Fulfillment
Of the Requirements for the Degree
Master of Science in Materials Science and Engineering

Georgia Institute of Technology

August, 2005

REACTIVE REPLACEMENT AND ADDITION OF CATIONS IN BIOCLASTIC SILICA AND CALCITE

Approved by:

Dr. Kenneth H. Sandhage, Advisor
School of Materials Science and Engineering
*Georgia Institute of Technology*

Dr. Thomas H. Sanders, Jr.
School of Materials Science and Engineering
*Georgia Institute of Technology*

Dr. Joe K. Cochran, Jr.
School of Materials Science and Engineering
*Georgia Institute of Technology*

Dr. Robert L. Snyder, Chair
School of Materials Science and Engineering
*Georgia Institute of Technology*

Date Approved: May 16, 2005

## ACKNOWLEDGEMENT

This work would not have been possible without the encouragement, support and presence of many people in my life from my family and old friends to faculty and new friends at Georgia Tech. I greatly appreciate the financial support for my project from the Air Force Office of Scientific Research and from the Boeing Corporation Fellowship Program. I must thank Ken Sandhage, my advisor, for the opportunity to take on this project as well as for support in pursuing new ideas in research which led to the work presented in Chapters 2, 4 and 5. Several members of my research group have lent valuable assistance in my efforts to become a better materials scientist, especially Helene Rick, Ben Church, Mike Weatherspoon, Matt Dickerson, Sam Shian and Philip Graham.

In my time at Georgia Tech I became involved in two great extracurricular organizations, ORGT and Chamber Choir thanks to my good friends Michael Middlemas and Matt Taylor. Their help in getting me out of the lab now and then made my experience in work and out that much more worthwhile, and opened my eyes to the great things happening in student life at Tech and the awesome serenity of North Georgia.

And of course my family's encouragement, especially from my mother, Linda, has guided me through these past two years of learning and personal growth.

## TABLE OF CONTENTS

## LIST OF TABLES

## LIST OF FIGURES

## LIST OF SYMBOLS or ABBREVIATIONS

| | |
|---|---|
| °C | Degree Centigrade |
| ADC | Ammonium dichromate |
| APM | Ammonium para-molybdate |
| APT | Ammonium para-tungstate |
| atm | Atmosphere (pressure) |
| BaSIC | Bioclastic and Shape-preserving |
| $BaTiO_3$ | Barium titanate |
| BET | Brunauer, Emmett and Teller (surface area analysis method) |
| $CaCrO_4$ | Calcium chromate |
| $CaMoO_4$ | Calcium molybdate |
| $CaWO_4$ | Calcium tungstate |
| $Cl_2$ | Chlorine (gas) |
| cm | Centimeter |
| EDS | Electron dispersive spectroscopy |
| g | Gram |
| HCl | Hydrochloric acid |
| hr | Hour |
| $LI_2O$ | Lithium oxide |
| $Li_2SiO_3$ | Lithium silicate |
| $Li_2SiO_4$ | Lithium silicate |
| µm | Micrometer or micron |
| m | Meter |
| $Mg_2Si$ | Magnesium silicide |
| $Mg_3N_2$ | Magnesium nitride |
| $MgCl_2$ | Magnesium chloride |
| MgO | Magnesium oxide |
| $MgWO_4$ | Magnesium tungstate |
| NaOH | Sodium hydroxide |

| | |
|---|---|
| nm | Nanometer |
| PLZT | Lead lanthanum zirconium titanate |
| r | Density |
| RIR | Relative Intensity Ratio |
| RWP | Recreational Water Products |
| s.s.a. | Specific surface area |
| SEM | Scanning Electron Microscopy |
| Si | Silicon |
| SiO | Silicon monoxide |
| $SiO_2$ | Silicon dioxide |
| TEM | Transmission Electron Microscopy |
| TGA | Thermogravimetric Analysis |
| TIG | Tungsten inert gas (welding) |
| $TiO_2$ | Titanium dioxide (anatase, rutile) |
| V | volt |
| XPS | X-Ray Photoelectric Spectroscopy |
| XRD | X-Ray Diffraction |
| $ZrO_2$ | Zirconium dioxide |

## SUMMARY

Numerous organisms produce ornately detailed inorganic structures (often known as shells) with features on length scales from 50 nm to several centimeters. One class of such organisms are the diatoms; microscopic algae that form silica frustules. Another group of algae, the coccolithophorids, produce similar calcium carbonate structures. Over 100,000 species comprise these two classes of algae, every one of which is endowed with a unique cytoskeleton structure.

Using various types of displacement reactions, the chemistry of the original structure can be modified to produce a new material. Magnesium vapor has been found to displace the silicon in diatom frustules to yield an MgO structure. The conversion has been reported at temperatures from 650°C to 900°C. In the current work, the conversion and processing of silica frustules to MgO was examined in depth. The effect of reaction temperature on grain size and extent of conversion was evaluated. With the goal of obtaining high purity MgO structures, various methods for removing the silicon products of reaction were investigated. Wet chemistry and high temperature vapor etches were evaluated. The MgO reaction served as an intermediate step in the production of magnesium tungstate diatoms, which were imbued with photoluminescent properties.

Reactions were identified to allow the conversion of calcium carbonate (calcite) structures to alternative chemistries. Calcite sand-dollars were converted to calcium tungstate or calcium molybdate by aqueous solution chemistry. In this process, sand dollar tests (shells) and coccolithophore frustules were reacted with ammonium para-

molybdate or ammonium para-tungstate. The reactions were evaluated for shape preservation, phase purity, and photoluminescence of the structures.

# CHAPTER 1

# THE MAGNESIUM OXIDE DIATOM CONVERSION PROCESS

## 1.1 Introduction

Numerous methods have been developed to form high temperature or complex ceramics via low temperature processes so as to develop fine-grained microstructures. In hydrothermal, combustion synthesis and sol gel processes, complex and fine grained ceramic powders are formed at remarkably low temperature in high pressure water vapor[1-4]. A wide range of deposition techniques have been developed by the semiconductor industry for low temperature fabrication of complex planar structures with an almost infinite selection of materials[5, 6]. Only a few commercially viable methods have been developed to directly fabricate complex three dimensional structures[7-9]. A recently developed process, BaSIC (Bioclastic and Shape-preserving Inorganic Conversion), added to the library of microfabrication techniques by facilitating the development of three dimensional structures of various materials through a biomimetic approach that uses biologically created templates (i.e., the inorganic shells of microscopic algae)[10].

Just in the class of algae known as diatoms, an astounding variety of self-assembled, rigid micro and nanostructures are generated. The estimated 100,000 diatom species correspond to an equal number of uniquely-shaped silica ($SiO_2$) nanoparticle-based microshells called frustules. The morphologies available through extant species include (among many other things) pill box shaped structures, hollow cylinders, disks, interlocking 'barbs', trigonal structures and high aspect ratio needles. In most species

these frustules are perforated by regular arrays of pores of relatively uniform size, shape and placement. An excellent review of the diversity of the diatom genera is found in Round's book, The Diatoms: Biology & Morphology of the Genera[11]. Under favorable growth conditions, natural reproduction of a few diatoms can quickly yield enormous numbers of frustules[11-15]. The genetic precision and high reproduction rate of such three dimensional nanoparticle self-assembly are highly attractive for device, catalysis, high surface area sensor, and filtration applications.

The remains of diatoms (diatomaceous earth) have been mined and used for centuries in filtration, and more recently stabilization of shock-sensitive chemicals and a wide range of other applications[16]. The uniform nanopore structure, microchannels, chemical inertness, and silica microcrystal structure of the frustules suggest many nanoscale applications[17]. In filtration and catalysis applications, in which a material other that silica would be preferred, retention of frustule shape would be favorable to preserve the high surface area of the original frustules that is so desirable in applications currently using silica diatoms. More recently diatoms have been considered for use in microdevices for their ability to produce enormous quantities of complex shapes at relatively low cost[18, 19].

In order to increase the attractiveness of diatom structures in new realms of application, processes have been developed to alter the silica-based chemistry of diatom frustules to produce new compositions possessing a variety of properties. Low-temperature gas-silica displacement reactions have been used to convert silica-based diatom frustules into other simple oxides (titania, magnesia, calcia, etc.) while preserving the original morphology[10, 20].

The MgO-conversion process may be significant for many applications. An MgO diatom structure with opposite surface charge of silica could be attractive for filtration systems where a high surface area, positively charged filter is desired. Contaminants of some heavy metals in effluent water streams may be absorbed by MgO filters. The MgO frustule provides a chemistry that may serve as an intermediate step for producing structures in other materials such as $MgWO_4$, which would not be attainable directly from a $SiO_2$ template. Furthermore, MgO provides a substrate for various functional materials including barium titanate and PLZT, both of which can be used for sensing, actuating, and luminescent applications[6, 21-23]. MgO is already common as a catalyst support and the high surface area and low bulk density of diatom structures provides an ideal structure for catalysis[24, 25]. Other potential applications for nano-crystalline MgO include catalyst supports for reduction of $H_2S$ emissions, scrubbing of $SO_2$ emissions, chlorofluorocarbon decomposition, petrochemical catalysis, fertilizers, drug delivery and fillers for refractories, plastics and ceramic-matrix composites[25-41]. Nanocrystalline MgO often exhibits enhanced properties for many such applications, particularly in catalysis and in the treatment of effluent in waste streams[42].

In earlier work on the reaction to produce MgO, two silicon-based products were identified, elemental silicon (Si) and magnesium silicide ($Mg_2Si$)[43]. The microstructural evolution during conversion at 650°C was evaluated using high-resolution TEM. The studies focused on temperature, time, and the ratio of magnesium to silica influence on the type of silicon co-product and its morphology. At low reaction temperature, the silicon products remained contiguous with the MgO but at higher temperature the silicon products coarsened and segregated to the surface of the frustule. Thus at low

temperatures of reaction, nanocomposites of MgO and Si were created[44-46]. Other authors have proposed using the magnesium displacement reaction to produce high purity polycrystalline silicon[47-49] from the silica ash of rice husks, however shape preservation was not a consideration in those studies. Our vapor process has shown that the structural continuity of the MgO in the frustule provides a shape tailored support for nanocrystalline Si.

In this thesis the impact of temperature on the MgO reaction on the resulting particle size and surface area has been examined in the range of 550°-900°C. The conversion of flame-polished (crystalline) diatoms was compared with that of higher surface area raw (amorphous) diatomaceous earth.

The role of reaction intermediates in the reduction of silica by Mg vapor from 650°C to 900°C was considered in this work. Previous authors identified intermediate reactions in the reduction of silica by magnesium vapor. Wynnyckyj, *et. al*., suggested forsterite ($Mg_2SiO_4$), enstatite ($MgSiO_3$) and silicon monoxide (SiO) as products in the reduction process conducted at 1100°C[50]. Several of the following reactions were considered to be active when reaction is performed at high temperatures. Banerjee et. al., reported an increased incidence of intermediate magnesium silicate phases in the magnesiothermic reduction of silica as reaction temperature is increased[48]. In the study on MgO frustule formation, the samples were surveyed for magnesium silicate intermediates. Cutler, *et. al.,* proposed the intermediate reaction of Mg with $SiO_2$ to form SiO as low as 580°C in their work on producing silicon carbide by a thermite reaction where Mg vapor initiates reaction between $SiO_2$ and carbon[51]. As SiO lacks a crystalline

form, its presence was neither confirmed nor rejected, but is discussed in a qualitative manner in Chapter 5.

$$Mg + SiO_2 \rightarrow MgO + SiO \quad (1)$$[51]

$$2SiO_2 + 2Mg \rightarrow Mg_2SiO_4 + Si \quad (2)$$

$$2SiO_2 + Mg \rightarrow MgSiO_3 + SiO \quad (3)$$

$$3SiO_2 + 2Mg \rightarrow Mg_2SiO_4 + SiO \text{ or } 2MgSiO_3 + Si \quad (4)$$

$$Mg_2SiO_4 + 2Mg \rightarrow 4MgO + Si \quad (5)$$

Assumptions for the preparation of MgO frustules are based on the reaction as follows where [Si] represents either Si or $Mg_2Si$:

$$2Mg + SiO_2 \rightarrow 2MgO + [Si] \quad (6)$$

## 1.2 Experimental Materials and Procedure

Silica diatom frustules (flame polished *Aulacoseira* from Recreational Water Products, Scottdale, GA; raw mined *Melosira* from DiaSource Inc., Westfall, OR) were reacted with the vapor generated by heating 99.8% pure magnesium granules (Alfa, m.p. 650°C) at temperatures in the range of 550°-900°C in 20 cm long by 2.5 cm diameter, 1020-iron tubing (TW Metals), that was sealed shut by TIG welding in air. For 800° to 900°C runs, the iron ampoule was also used as a substrate for 0.6 grams of silica diatoms and for varying amount of Mg granules at the opposite end of the ampoule. The depth of the diatom silica powder bed did not exceed 5 mm. The ampoule was crimped into an inverted "V" shape to segregate the solid Mg and diatom silica reactants (Figure 1). For runs at and below 650°C, 0.1 grams of silica diatoms were arranged in a boat made of 1008 iron foil (ASTM A109), 0.76 mm thick (McMaster Carr), 30 mm long, 20 mm wide,

with 3 mm tall walls to retain the diatoms. The ampoule length was shortened to 10 cm for runs at and below 650°C, and the iron boat was placed on top of the bed of Mg granules. The depth of the diatom silica bed in the iron boat did not exceed 1 mm for runs at and below 650°C.

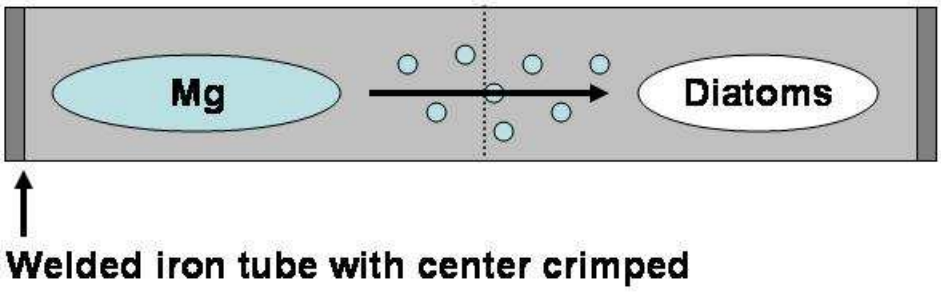


Figure 1.1. Schematic of reaction ampoule for the production of MgO diatom frustules. As the ampoule is heated, the vapor pressure of Mg increases, which facilitates the transport of Mg to the $SiO_2$ diatom side of the tube. The schematic is shown top down, where the dashed line represents the "Λ" shaped crimp.

Because the ampoules were sealed in air, excess Mg was included in the reaction ampoules to serve as a getter for the $O_2$ and $N_2$. The internal volume of the 20 cm long reaction ampoules was determined to be approximately 35 ml, corresponding to 1.1 mmole $N_2$ and 0.30 mmole of $O_2$. Formation of $Mg_3N_2$, magnesium nitride, and MgO from the air in the ampoule required 0.096 gram of Mg in addition to the Mg intended for reaction with the silica diatoms. Gettering the $O_2$ and $N_2$ was necessary from a physical perspective for runs at 900°C to avoid swelling of the ampoules due to pressure build up. This swelling would undo the crimp in the ampoule and possibly cause direct contact of liquid Mg with silica diatoms to occur. The inclusion of excess Mg for de-airing the ampoule resulted in a starting ratio of 2.45 moles Mg to 1 mole $SiO_2$ (0.6 grams of each). For reactions at and below 650°C, the ratio of Mg to $SiO_2$ was increased; the size of the powder bed reduced; and the ampoule length was shortened to 10 cm. All this was done

to facilitate transport of Mg vapor to the silica diatom powder bed at reduced Mg vapor pressure.

The crystallite size and morphology of the reacted frustules was investigated by scanning electron microscopy (SEM) (LEO-1530, S-800, Hitachi, Japan). The composition of the frustules was studied with X-ray diffraction (PW-1800, Philips, The Netherlands) and X-ray photoelectron spectroscopy (XPS) and electron dispersive spectroscopy (EDS). Particle size was calculated from SEM and TEM micrographs, and where data was available, by using the Williamson Hall method of extracting crystallite size information from XRD peak widths, which does not require the use of a coarse-grained standard material[52]. In the Williamson Hall method, the XRD pattern peak width (B) is measured for all peaks in a phase, preferably up to high values of 2θ. The term, B*cos (θ), is plotted versus the term, sin (θ). A linear regression is used to fit the points. The particle size and strain were then calculated from the y-intercept and slope of the linear fit respectively. The particle size is given as D and the strain is given as (Δd/d).

$$B*\cos(\theta) = (0.9\lambda/D)\sin(\theta) + 2(\Delta d/d)$$

The transmission electron microscopy characterization was performed on samples converted at 650°C and 550°C. The transmission electron microscope (Model 4000EX, JEOL, Tokyo, Japan) was operated at a voltage of 400 kV. Thermogravimetric analyses (TGA) were performed on the starting diatom materials in the Netzsch Jupiter (STC 440) in air, with a heating rate of 5°C/min from 25°C to 600°C. Surface area analyses were performed using a Quantachrome BET surface area analyzer (BET) (ASAP 2000, Norcross, GA).

## 1.3 Results and Discussion

### 1.3.1 Analysis of Starting Diatom Frustules

XRD analyses indicated that the flame polished diatoms were crystalline while the DiaSource diatoms were amorphous (Figures 1.2a and 1.3a). The crystalline silica was identified as primary cristobalite that was devitrified in the flame polishing process, but traces of tridymite were also found, as a small side peak just to the left of the main cristobalite peak. Tridymite is a metastable phase of silica that is indicative of alkaline impurities, as it is not considered to be a stable phase of pure silica[53, 54]. In fact, chemical analysis from suppliers of diatomaceous earth often report both magnesium and calcium present in small quantity in the silica, as well as aluminum (Figure 1.4a and 1.4b). DiaSource reported impurity levels of 1.12 to 4.40 % aluminum, 0.22 to 0.53 % calcium, 0.14 to 0.31 % magnesium and 0.63 to 1.1 % iron[55]. Aluminum was often identified in small amounts in converted MgO diatoms and was noted in previous work[43]. TGA of the two starting materials showed a rapid loss of mass indicative of absorbed and adsorbed water in the DiaSource material, but only a minor weight change was observed in the flame polished diatoms (Figure 1.5). SEM showed more variation in the size and aspect ratios of the *Melosira* material than in the *Aulacoseira*, in Figure 1.4c and 1.4d. BET surface analysis gave specific surface areas of 1.35 (0.19) $m^2/g$ for the flame polished *Aulacoseira* and 61 $m^2/g$ for the *Melosira* material. The significant difference in the starting material underscores our interest in exploring the resulting characteristics of both materials after undergoing the MgO conversion reaction.

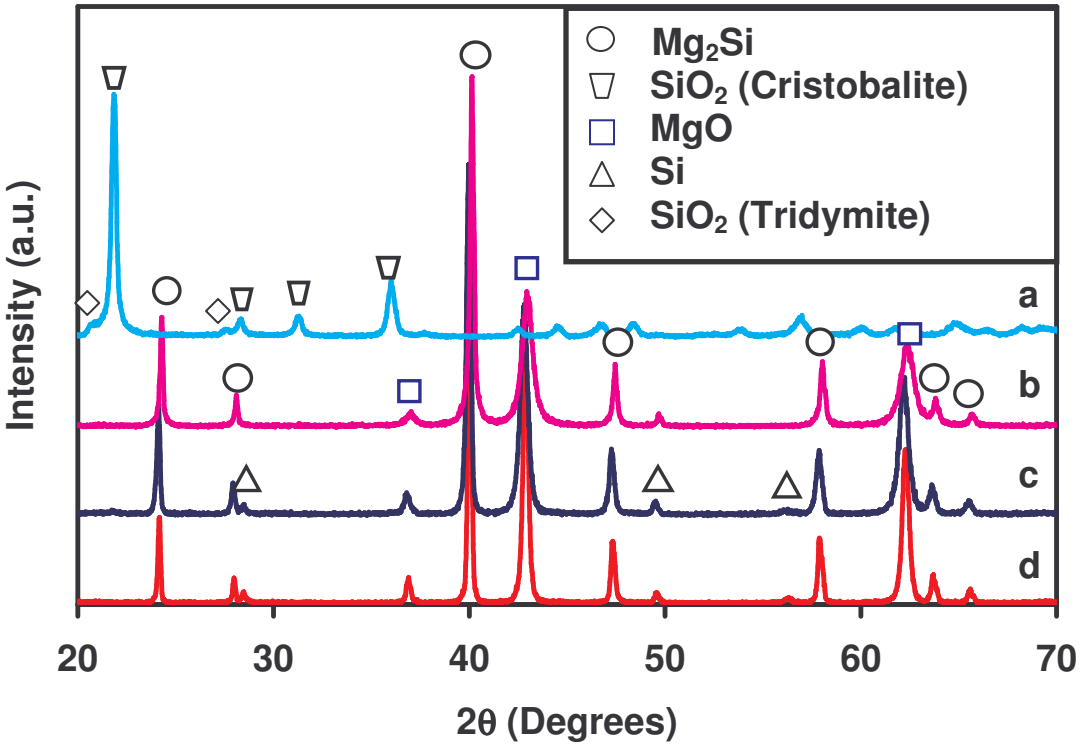


Figure 1.2. XRD of *Aulacoseira* diatom frustules (a) prior to conversion, (b) converted to MgO at 600°C in 3 hr, with 10:1 Mg to $SiO_2$ ratio, (c) converted at 800°C in 2 hr with 2.45:1 ratio, (d) converted at 900°C in 1.5 hr with 2.45:1 ratio. Peak broadening of the main MgO peak due to the effect of decreaseing particle size is visible as reaction temperature decreases. The sharpness of the $Mg_2Si$ peaks at all reaction temperature indicates coarse particle sizes regardless of process temperature.

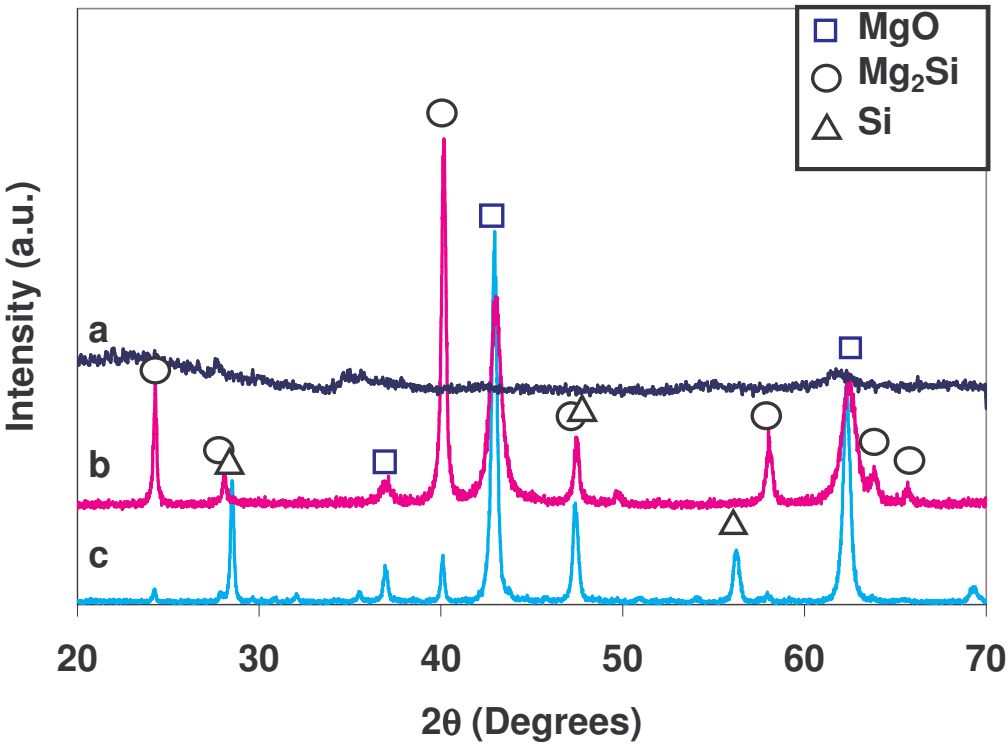


Figure 1.3. Amorphous *Melosira* diatom XRD. a.) starting silica, b.) 650°C, 1.5 hr, 10:1, with primarily $Mg_2Si$ byproduct, c.) 900°C, 1.5 hr with 2.45:1 ratio, yielding both Si and $Mg_2Si$ byproducts. The narrowing of the primary MgO peak at approximately 43° 2θ from (b) to (c) indicates an increase in particle size of the MgO with the increase in reaction temperature.

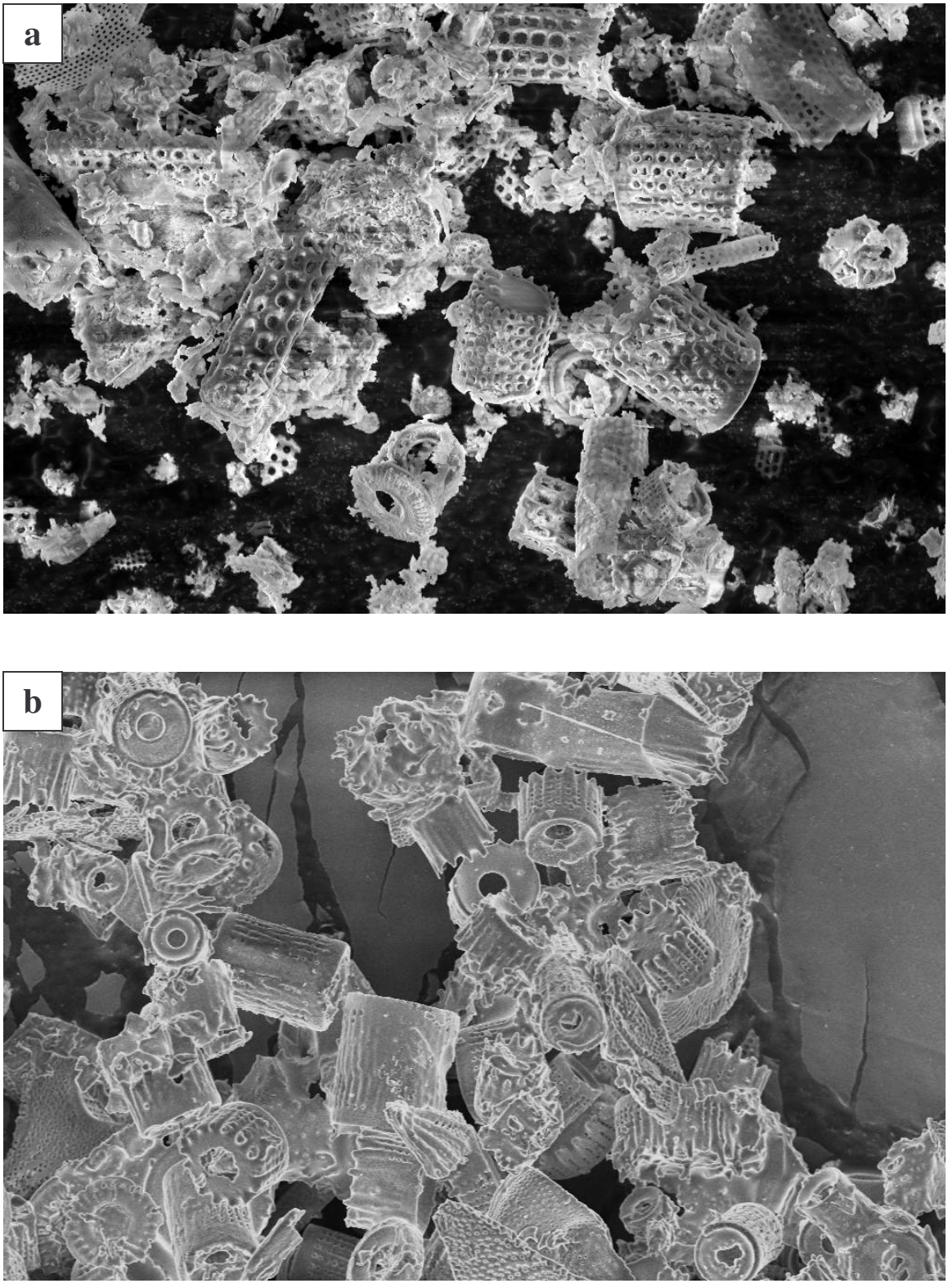


Figure 1.4. SEM of silica (a) *Melosira* (as-mined amorphous) and (b) *Aulacoseira* (flame polished cristobalite) diatom frustules.

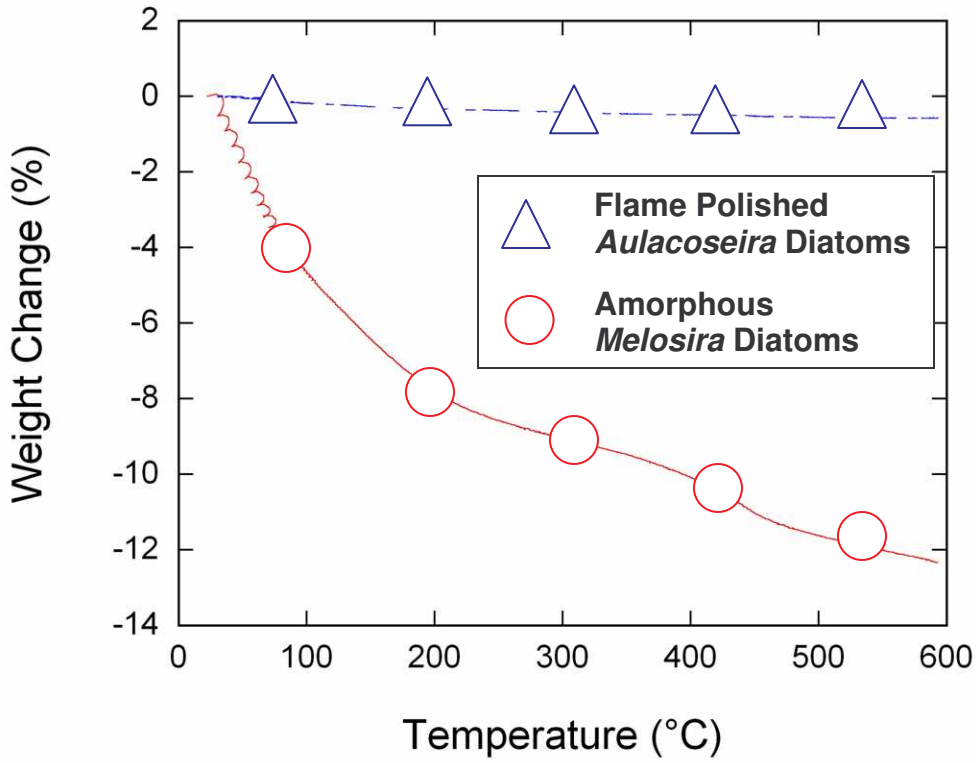


Figure 1.5. TGA of flame polished *Aulacoseira* and amorphous *Melosira* diatomaceous earth as received from suppliers. Heating rate was 5°C/minute to 600°C, performed in air with a powder depth of 2 mm.

### 1.3.2 Phase Control of MgO Conversion Process

The MgO reaction products were characterized by visual observation of color, XRD and SEM. A black or blue color in the diatom powder bed indicated 'complete conversion' to MgO, meaning conversion of $SiO_2$ to Si had occurred. The color black corresponded to elemental Si and the color blue related to the presence of $Mg_2Si$. In some cases, a brown region was observed on at the opposite end of the powder bed from the blue zone. Silicon monoxide is reported in literature as a brown colored material[54, 56, 57]. The ordering of colors in reacted powder beds (indicated in Figure 1.6a) fit a trend of decreasing Mg content from the silicide zone (4 Mg to 1 $SiO_2$) to the silicon zone (2 Mg to 1 $SiO_2$) and finally to the brown (possibly SiO) zone (1 Mg to 1 $SiO_2$). In many runs, a brown deposit was found coating the inside of the reaction ampoules, characteristic of condensed amorphous silicon monoxide[54]. A starting Mg:$SiO_2$ mole ratio of 2.45:1, reacted at 900°C for 1.5 hour yielded primarily MgO with Si byproduct (Figure 1.6b). Some $Mg_2Si$ was observed along the upper surface of the powder bed. At a ratio of 3.7:1 Mg:$SiO_2$ a distinct blue zone of MgO diatom frustules with $Mg_2Si$ byproduct was observed in the diatom powder bed closest to the Mg vapor source (Figure 1.6c). A black zone was observed farther from the Mg source, bearing a sharp boundary with the $Mg_2Si$ zone. MgO diatom frustules with Si byproduct comprised the black zone. At higher ratios of Mg to $SiO_2$, such as 12:1, the entire diatom powder bed was converted to MgO with $Mg_2Si$ byproduct (Figure 1.6d). XRD was used to confirm the relationship of color to the product compositions (Figure 1.6). An Mg:$SiO_2$ ratio of 2:1 resulted in incomplete reaction of the silica diatoms.

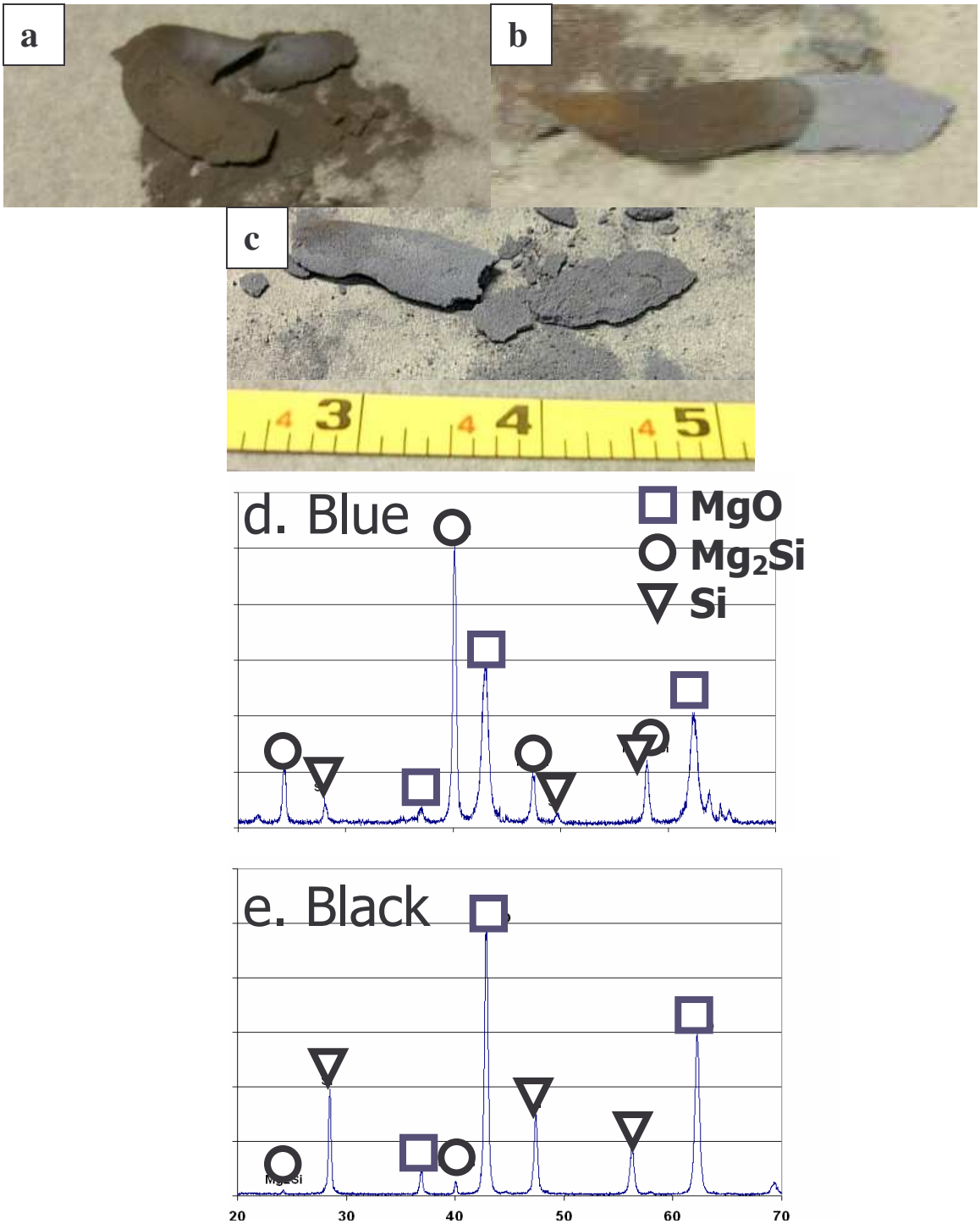


Figure 1.6. Optical images of MgO-converted diatom powder beds at 900°C for 2 hours with increasing molar ratio of Mg to $SiO_2$. (a) 2.45:1 – nearly all Si byproduct, (b) 3.7:1 – half Si, half $Mg_2Si$ byproduct, (c) 12:1 – all $Mg_2Si$ byproduct. XRD patterns, (d) and (e), show the phase composition of selected samples of "blue" ($Mg_2Si$ bearing) and "black" (Si bearing) MgO diatom frustules.

The excess Mg required for complete reaction (associated with the earlier mentioned 2.45:1 mole ratio required for complete reaction) was responsible for gettering the $N_2$ and $O_2$ from the air sealed inside the ampoule. The air was condensed as $Mg_3N_2$ and MgO, as confirmed by XRD analysis of material retrieved from the Mg end of an ampoule after reaction (Figure 1.7). The removal of air prevented the swelling of the ampoules during heating, which commonly occurred if the ampoules were sealed in argon.

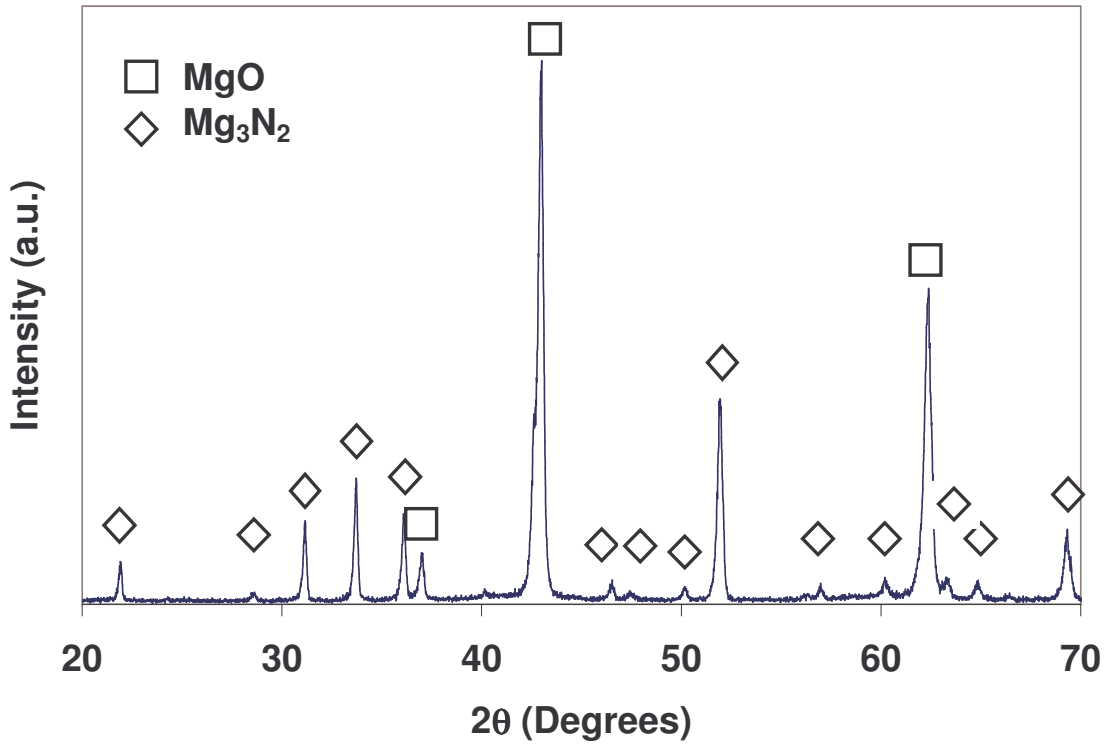


Figure 1.7. XRD of Mg by-product, magnesium nitride and magnesium oxide obtained from a 900°C, 1.5 hr sample with 2.45:1 starting mole ratio of Mg and $SiO_2$.

Control over the silicon by-product phase appeared more dependent on kinetics of the Mg vapor both to and through the powder bed than simply on the reactant ratio for reactions performed at 650°C and below. Using a smaller powder bed (0.1 gram silica diatoms) with a depth of approximately 1 mm, distinct byproduct zones of $Mg_2Si$ and Si were visible and could be carefully separated for SEM study. However, while a batch of MgO containing entirely $Mg_2Si$-byproduct could be easily produced by using an over abundance of Mg reactant, control over the reactant ratio failed to produce a uniform batch of Si and MgO frustules.

Treated at or below 650°C and using a 20 cm ampoule length, diatom frustules nearest the surface of a powder bed (0.1 gram) would fully convert to MgO with $Mg_2Si$ byproduct after 120 minutes. By adjusting the reaction design for lower temperature runs, *i.e.*, placing the diatom powder bed (in an iron boat) directly atop the Mg source in a 10 cm long ampoule, the onset of reaction was accelerated, and full reaction could be achieved in 1.5 hour. An XRD time series (Figure 1.8) of reaction at 650°C using a 10:1 molar ratio of Mg to $SiO_2$ in 20 cm ampoules showed no reaction in the first hour at the reaction temperature, however in a high temperature XRD scan performed with argon cover gas and a special graphite reaction cell, the onset of magnesiothermic reduction was immediate (Figure 1.9).

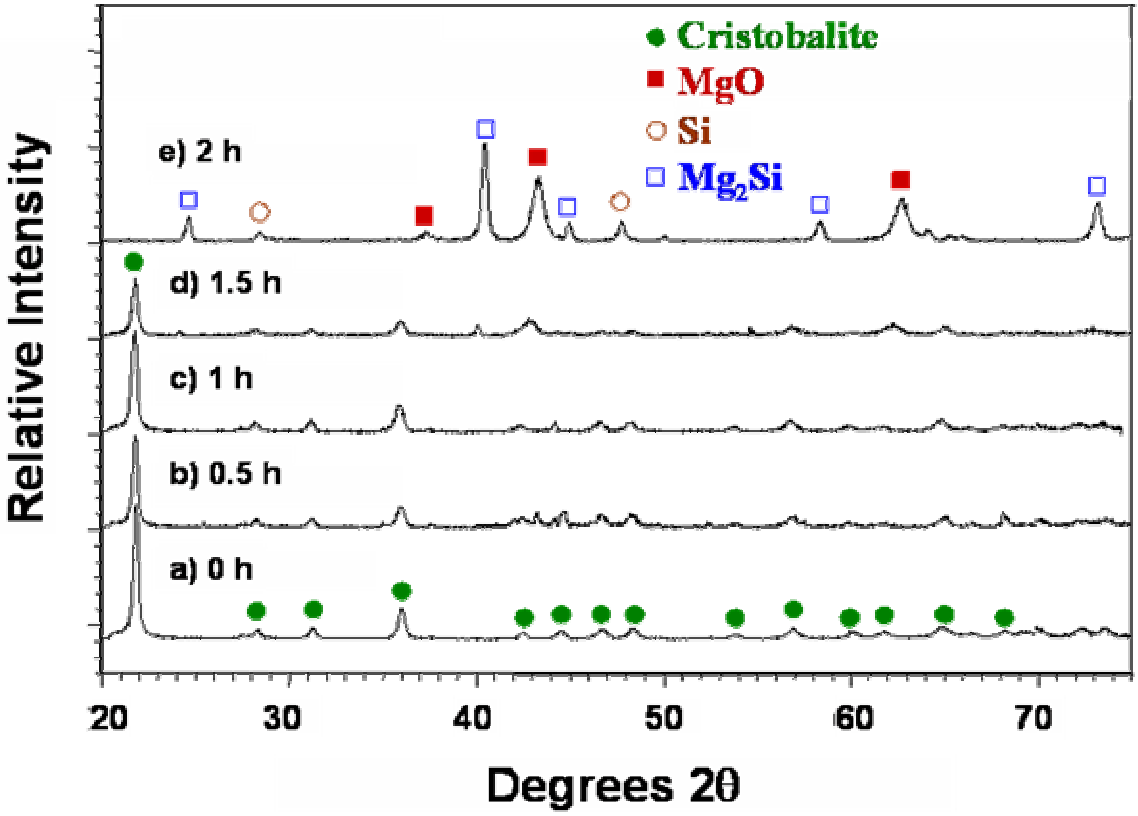


Figure 1.8. Time series of MgO reaction performed at 650°C showing conversion of silica diatoms (cristobalite) to MgO, Si and $Mg_2Si$. The ratio of the Mg and silica reactants was 10:1 molar.

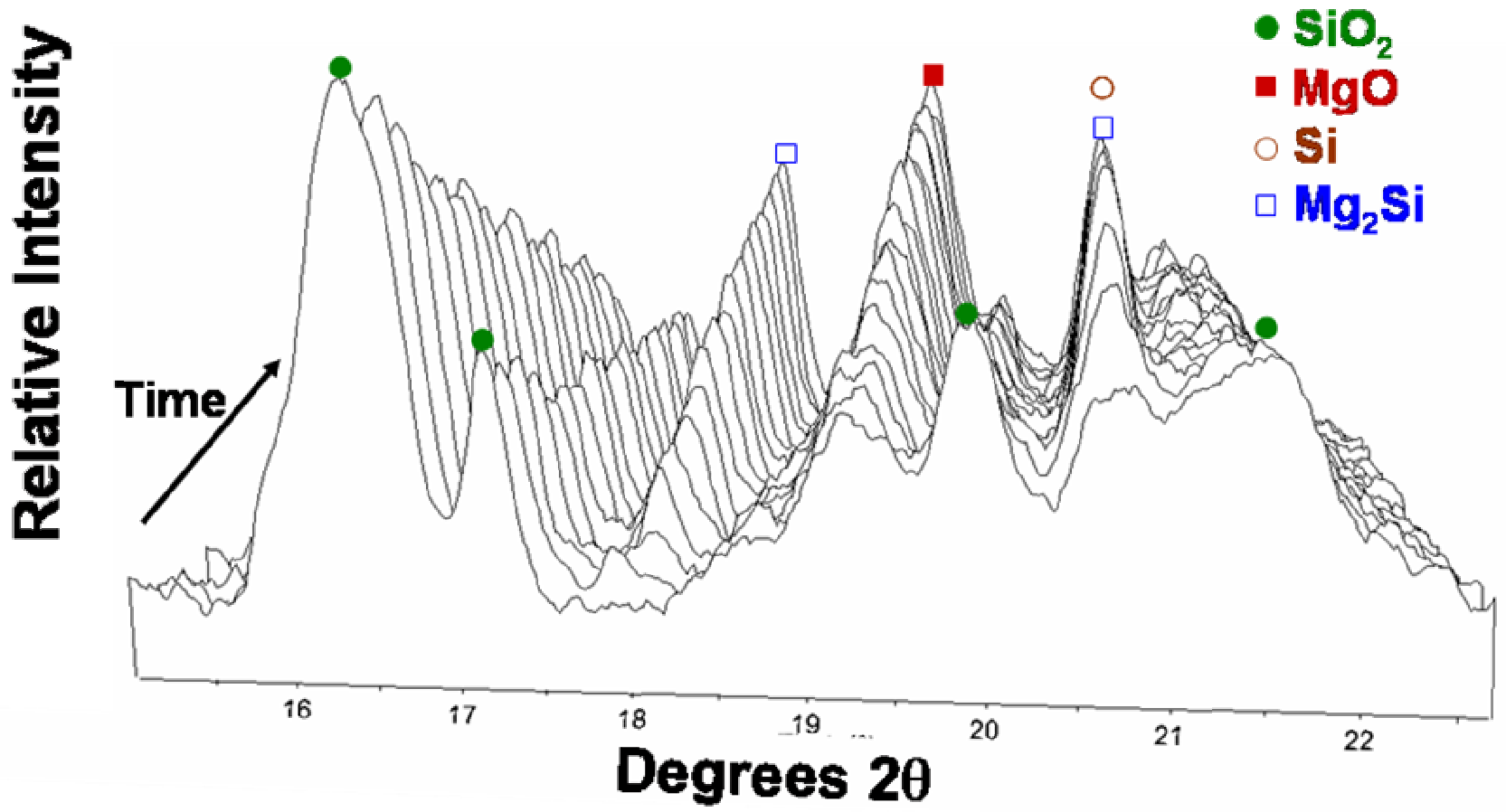


Figure 1.9. High temperature XRD of MgO reaction upon reaching 650°C in argon showing the progression of the reaction in 5 minutes intervals. Measurement performed by Michael Haluska, PhD.

To help overcome the low vapor pressure of Mg at 650°C (3.21 torr[58]), the Mg to $SiO_2$ ratio was increased to 10:1. For example at 900°C, where the equilibrium vapor pressure of Mg is 120 torr[58], 0.6 grams of silica diatoms, 5 mm deep, using 2.45:1 Mg:$SiO_2$, are converted to MgO in 1.5 hours. At a reaction temperature of 650°, with an equilibrium Mg vapor pressure of 3.21 torr[58], a 0.1 gram, 1 mm deep powder bed with a 10:1 Mg:$SiO_2$ ratio required 1.5 hour for complete reaction. At 600°C the equilibrium vapor pressure is reduced further to 0.62 torr[58] requiring 3 hours to fully convert a 0.1 gram, 1mm deep powder bed using a 10:1 mole ratio of Mg:$SiO_2$. Even at 550°C, well below the melting point of magnesium (638.6°C[58]), sufficient vapor pressure was available to convert a 0.1 gram powder bed after 6 hours. The efficiency of the conversion process is described graphically in Figure 1.10 as the ratio of the mass of diatoms processed to the time required to process (grams per reaction vessel per hour). The values obtained apply only for the range of powder bed sizes used in this study and are only meant to illustrate the general trend, that longer process time was required to convert less material when the reaction temperature is decreased. In other words, lower temperatures slow the rate of reaction. Vapor diffusion and/or the chemical reaction kinetics were considered as probable rate limiting factors contributing to the increased process time associated decreasing temperature, despite simultaneously decreased powder bed size.

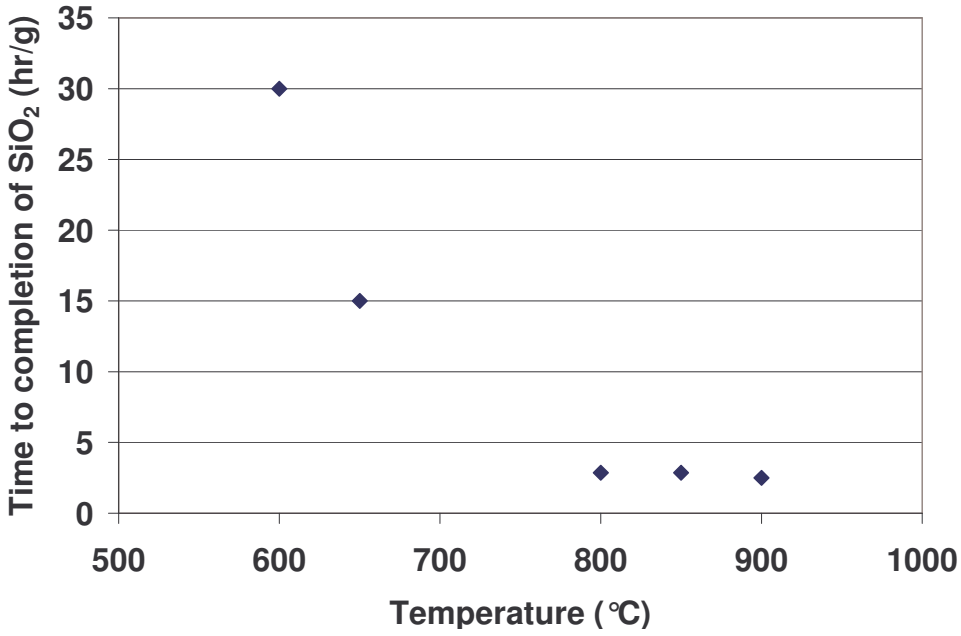


Figure 1.10. General trend of the time for complete conversion of silica diatom powder bed to MgO relative to batch size as a function of temperature. The time to completion was determined as the minimum time required to convert a particle bed of a given size such that no $SiO_2$ was found in the XRD after conversion. At 600° and 650°C, the powder bed size was 0.1 gram $SiO_2$. For 800° to 900°C, the powder bed used was 0.6 gram. The area of the powder bed was held constant for all temperatures such that only the depth of the powder bed increased with increased mass of $SiO_2$.

In any case where sufficient Mg was present to completely convert the $SiO_2$ to MgO, the presence of magnesium silicates as intermediates in the conversion of silica to MgO was not detected. When less than a 2.45:1 molar ratio of Mg was used, minor amounts of the magnesium silicate, $Mg_2SiO_4$ (forsterite), were detected by XRD in the product material (Figure 1.11). Like with the $Mg_2Si$ byproduct described earlier, which formed as a secondary process by the reaction of Mg vapor with Si, independent of the magnesiothermic reduction of silica, the forsterite detected here may have formed by reaction of MgO and $SiO_2$ as a secondary reaction, rather than as an intermediate.

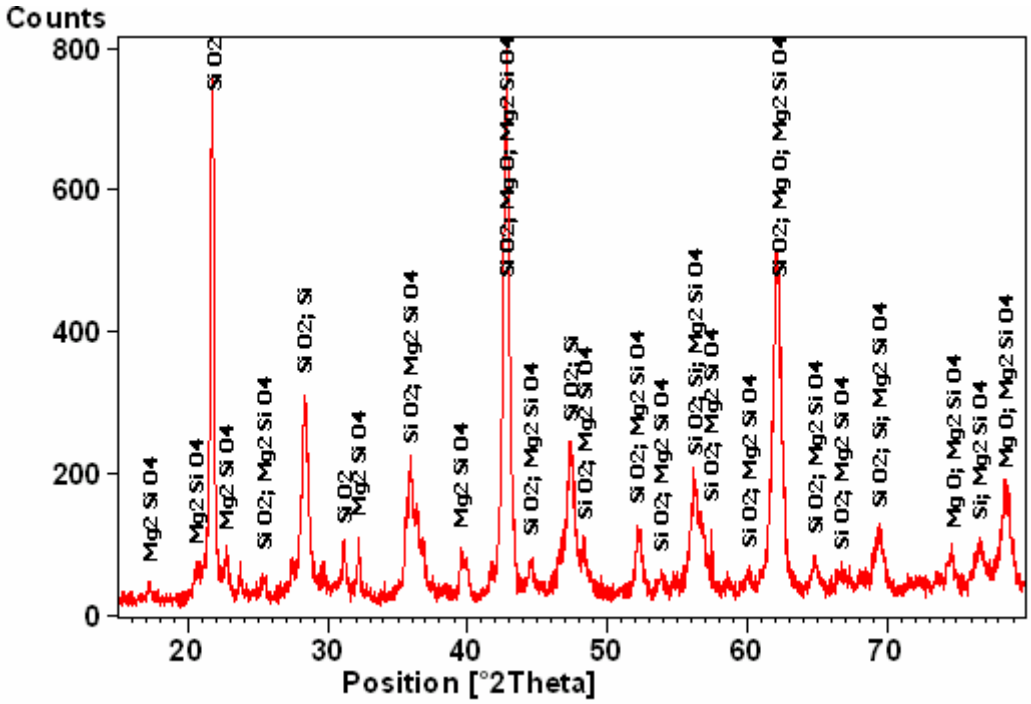


Figure 1.11. XRD pattern of Mg:$SiO_2$ starting molar ratio of 2:1 (no excess Mg for gettering air) after treatment at 800°C for 3 hours. Not only did the reaction fail to complete, but forsterite, $Mg_2SiO_4$, formed.

### 1.3.3 Microstructural Evaluation of Shape Preservation

Diatom frustules converted to MgO at 600 °C and 900 °C are presented in Figures 1.12, 1.13 and 1.14. SEM showed the typical microstructures of diatom frustules converted at 600°C in Figures 1.12 (flame polished *Aulocoseira)* and 1.13 (mined *Melosira)*. The finer grain structure improved the quality of shape preservation over that at 900°C (Figure 1.14) giving a smoother surface appearance. In addition to showing shape preservation, these figures also demonstrate the morphologies of the Si and $Mg_2Si$ by-products. At 600°C the Si byproduct is only distinguishable at the surface at high magnification. $Mg_2Si$ occurs as a coarse, angular grained coating in low temperature runs (Figure 1.12a) but is manifested as by a "solidified" appearance as in Figure 1.14b.

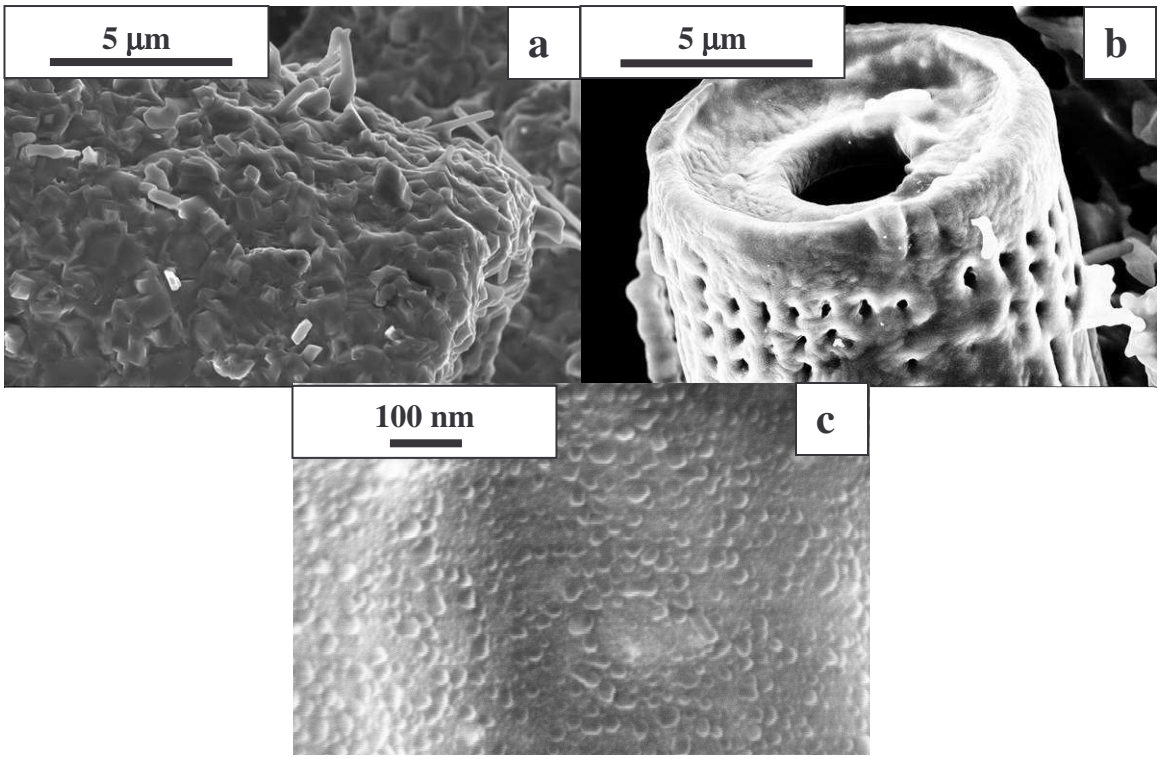


Figure 1.12. SEM of *Aulacoseira* diatoms converted at 600°C in 3 hr, (a) MgO with $Mg_2Si$ from 'blue' region, (b) MgO with Si from 'black' region, (c) high magnification of Si particles on MgO surface.

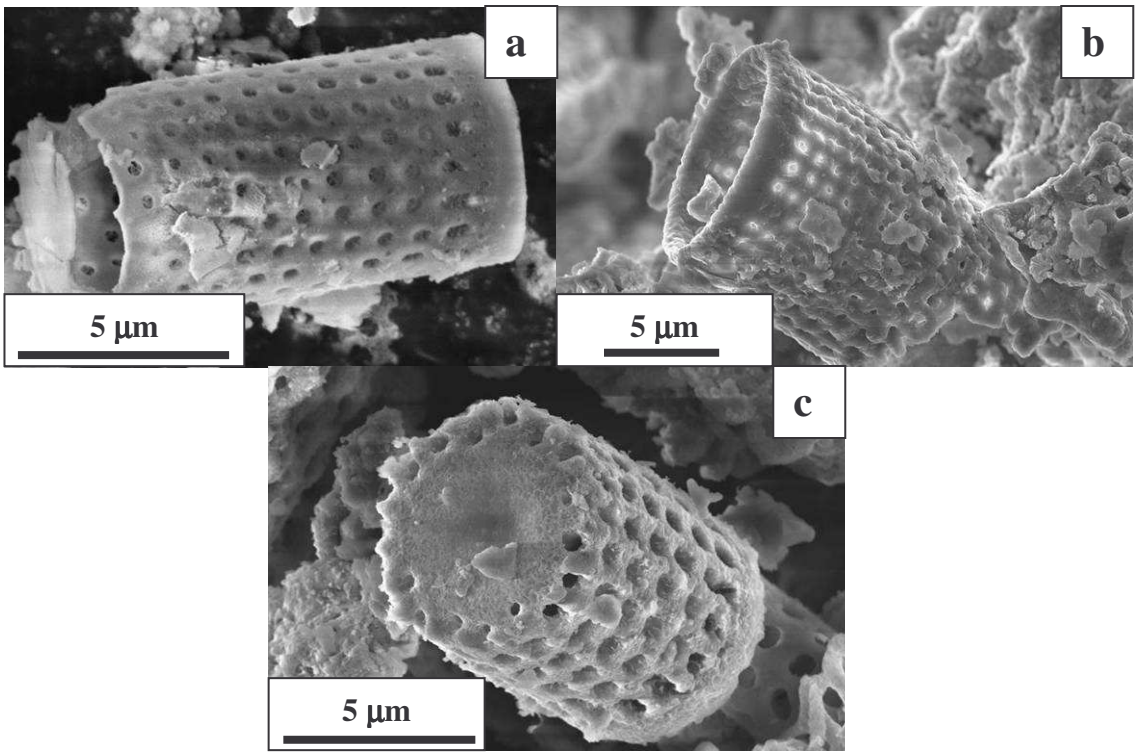


Figure 1.13. *Melosira* diatoms (a) amorphous $SiO_2$, (b) MgO with Si, 600°C in 3 hr with 10:1 mole ratio Mg:$SiO_2$, (c) MgO with Si, 900°C in 1.5 hr with 2.45:1 mole ratio.

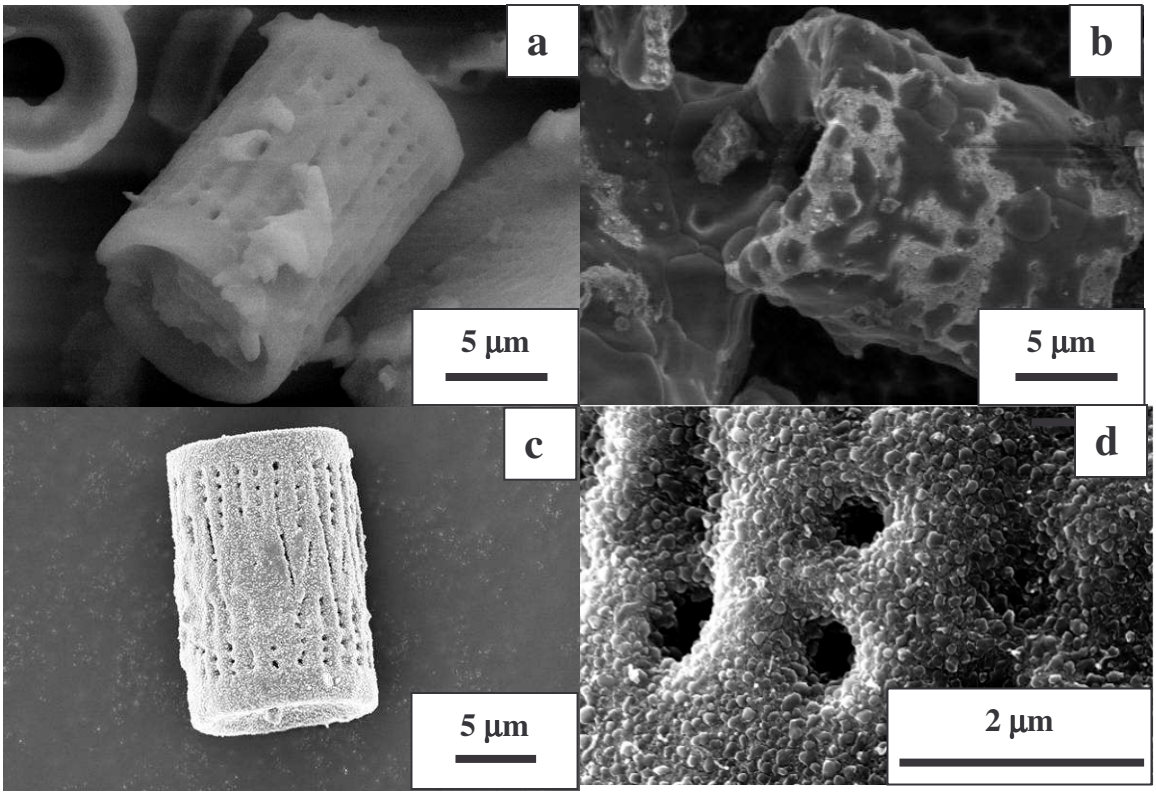


Figure 1.14. SEM of *Aulacoseira* a.) flame polished $SiO_2$ frustule b.) MgO with $Mg_2Si$ from 'blue' zone closest to Mg source, c.) MgO with Si from 'black' zone farther from reaction source, and d.) high magnification of MgO with Si. The reaction was performed at 900°C for 1.5 hr with 3.7:1 mole ratio Mg:$SiO_2$.

The MgO product varied from 12 to 89 nm average grain size from 600°C to 900°C as measured by the Williamson Hall method (Figure 1.15). Coarsening of the Si product was observed from 600 °C (up to 3 hours) to 900 °C (1.5 hours) from 23 nm to 89 nm average grain size respectively, as measured by quantitative stereology of SEM micrographs. The MgO particle size at 650°C, 1.5 hr was less than the particle size at 600°C, 3 hr, likely due to shorter reaction time. At 650°C, the MgO particle size averaged 21 nm when $Mg_2Si$ byproduct was present. For MgO produced at 650°C with Si by-product, the MgO average particle size averaged only 13 nm.

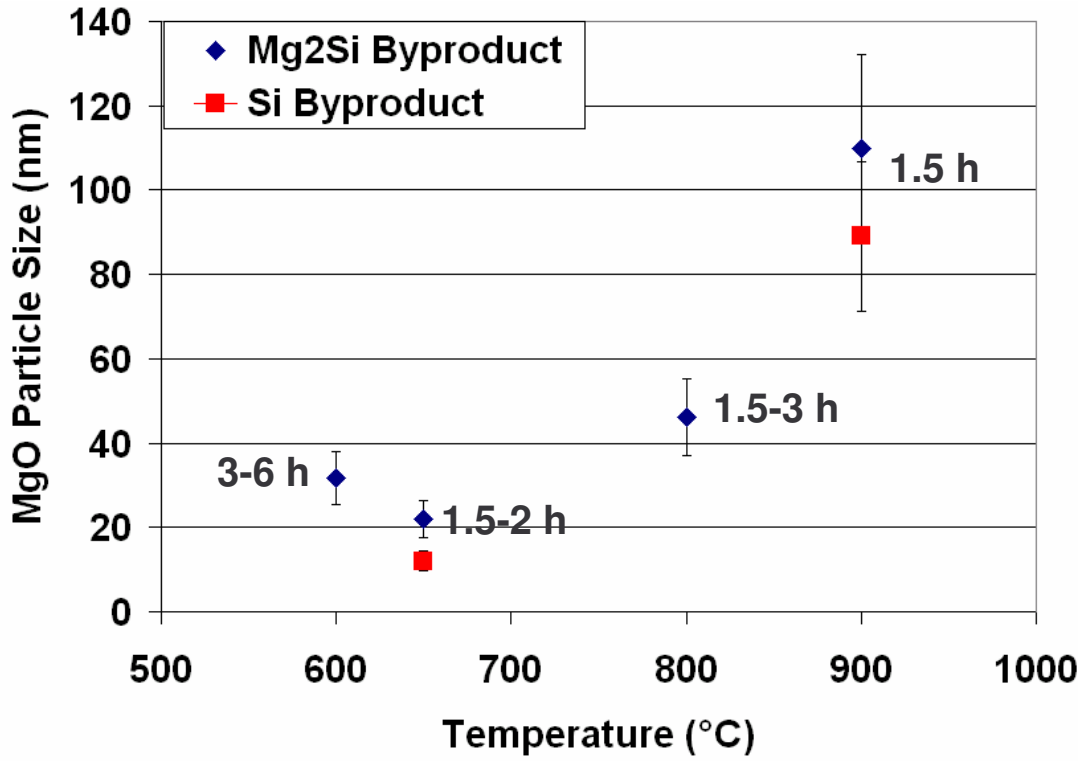


Figure 1.15. Average particle sizes of MgO grains as determined by the Williamson Hall method for samples produced over the range of 600°C to 900°C with dwell times from 1.5 to 6 hours. Results from 650°C and 900°C suggest a finer grain size was achieved when the byproduct was controlled as Si.

In many cases, the MgO with Si byproduct and MgO with $Mg_2Si$ byproduct could be separated from the same powder bed, perhaps from a 1.5 hour heat treatment. Silicon crystallites were visible on the surfaces of MgO diatom frustules, likely pushed to the surface by stresses due to volume increase of 17% from converting one $SiO_2$ into two MgO and one Si. When the frustules were exposed to excess Mg vapor (locally greater than 2:1 Mg:$SiO_2$), the silicon co-product was primarily $Mg_2Si$, and appeared to be coarsened by the assistance of a liquid phase material at reaction temperature, sweated out from the frustule by capillary action and stresses due to volume increase, often coating the exterior of the frustules. The grain size of $Mg_2Si$ was one or two orders of magnitude greater than that of the MgO or Si, even at 600°C where coarsening could not have been liquid phase assisted. A cross section of a frustule wall shows the $Mg_2Si$ coating an MgO frustule wall in Figure 1.16a. The fracture markings visible on the $Mg_2Si$, indicate that the cross section was created after reaction. The Mg-Si phase diagram[59] (Figure 1.17) shows that above 638.6°C, any amount of Mg in addition to stoichiometric $Mg_2Si$ will form a liquid phase, which likely accounts for the coarsening of the $Mg_2Si$ grains.

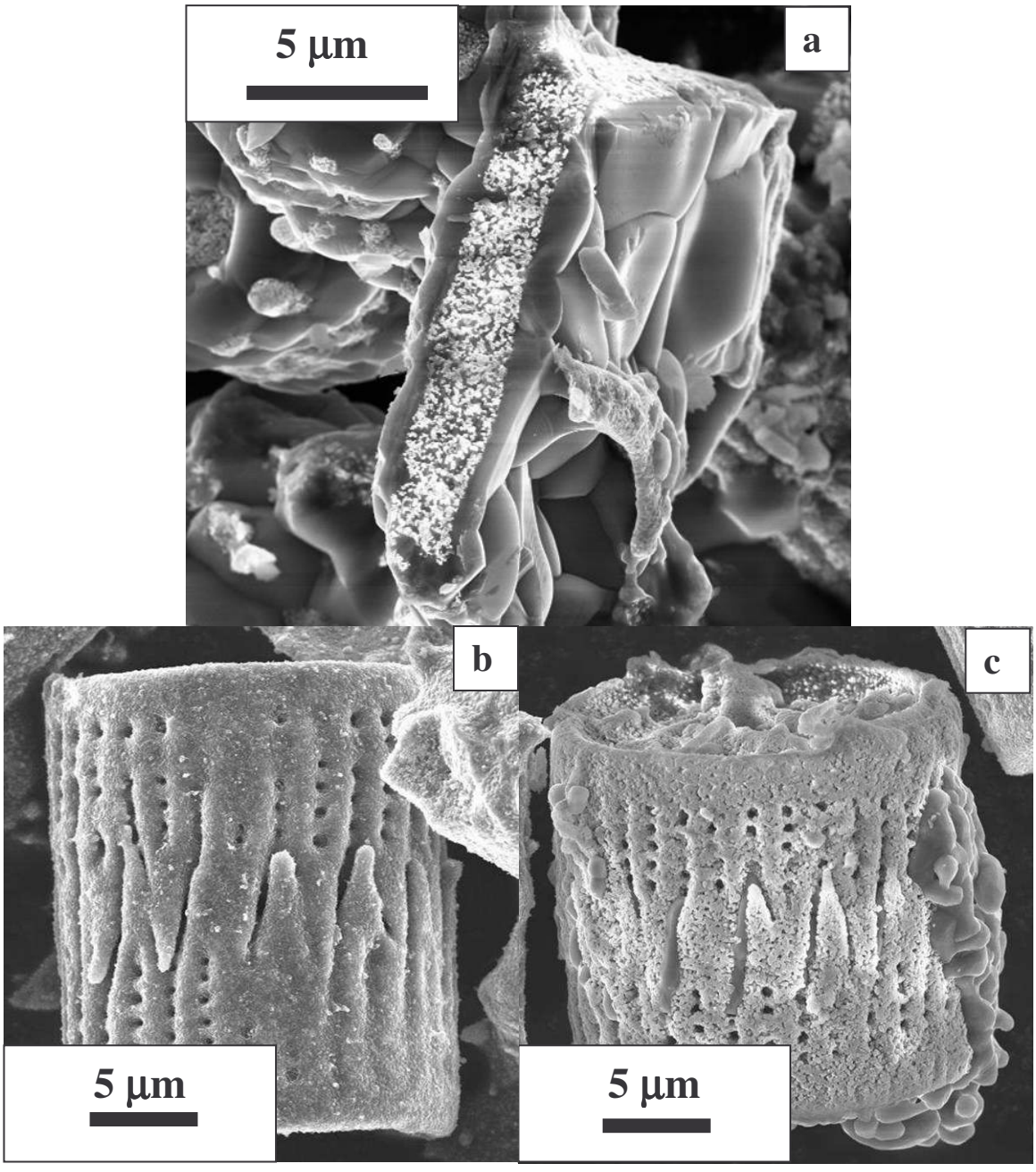


Figure 1.16. (a) Cross section of $Mg_2Si$ co-product coating the underlying MgO structure. (b) MgO diatom with Si, 900°C 1.5 hr (c) MgO diatom (from same run) showing coarsening of MgO at the onset of $Mg_2Si$ formation, $Mg_2Si$ can be seen 'pouring' from the right side of the frustule.

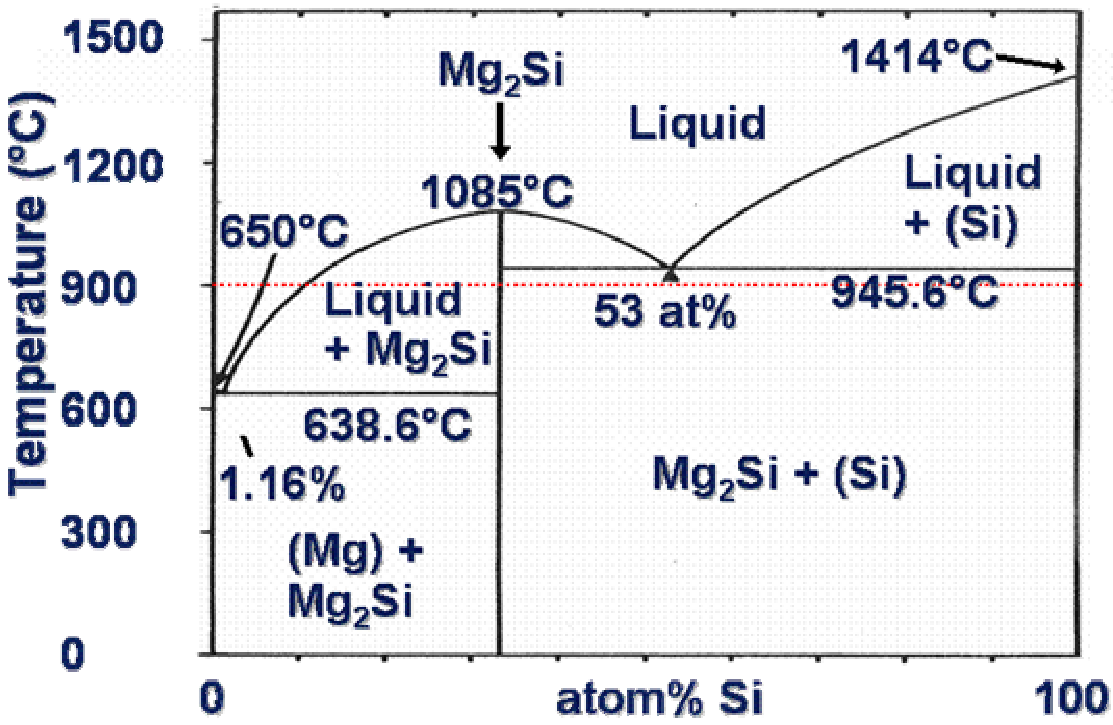


Figure 1.17. The Mg-Si phase diagram (reproduced with permission). When $Mg_2Si$ byproduct is formed, any additional amount of Mg will contribute to the formation of a liquid above 638.6°C. The coarsening of $Mg_2Si$ found even at low temperatures is attributed to this liquid phase formation. The dashed line indicates 900°C, the maximum temperature used for the MgO conversion process.

$Mg_2Si$ possibly contributed to the coarsening of the MgO, perhaps as a transport path for diffusion of Mg. The coarsening effect of $Mg_2Si$ on MgO was observed by SEM in a sample produced at 900°C in 1.5 hr (Figure 1.16, b and c). A diatom frustule was captured in the early stages of $Mg_2Si$ formation alongside other frustules that did not show any silicide. The MgO grains, which were indistinguishable in the MgO and Si diatom, appeared coarser in the sample with $Mg_2Si$.

TEM of frustules converted to MgO at 650°C (from 650°C time series discussed above, 10:1 molar ratio of Mg:$SiO_2$), and shown in Figure 1.18, substantiated the absence of magnesium silicate reaction intermediates ($Mg_2SiO_4$, $MgSiO_3$) as observed in higher temperature work reported with the Mg-$SiO_2$ system[48, 50]. No reaction was observed in the frustules exposed for 1 hour to the Mg vapor which were separated by a distance of approximately 10 cm, with the "Λ" crimp in between. After 1.5 hour, the reaction zone containing MgO and Si crystallites was observed to be spreading through the silica frustule wall. The delay in reaction was attributed to time required for the Mg vapor to first getter the $O_2$ and $N_2$ from the ampoule and then to overcome the crimp barrier. After 2 hours at 650°C, the frustule was fully converted to MgO, and the predominant silicon co-product was $Mg_2Si$. Only MgO and Si products were observed by high resolution TEM in the 1.5 hour sample, with no intermediates at the phase boundary. The MgO and Si particles were observed to range from 5 to 15 nm in size.

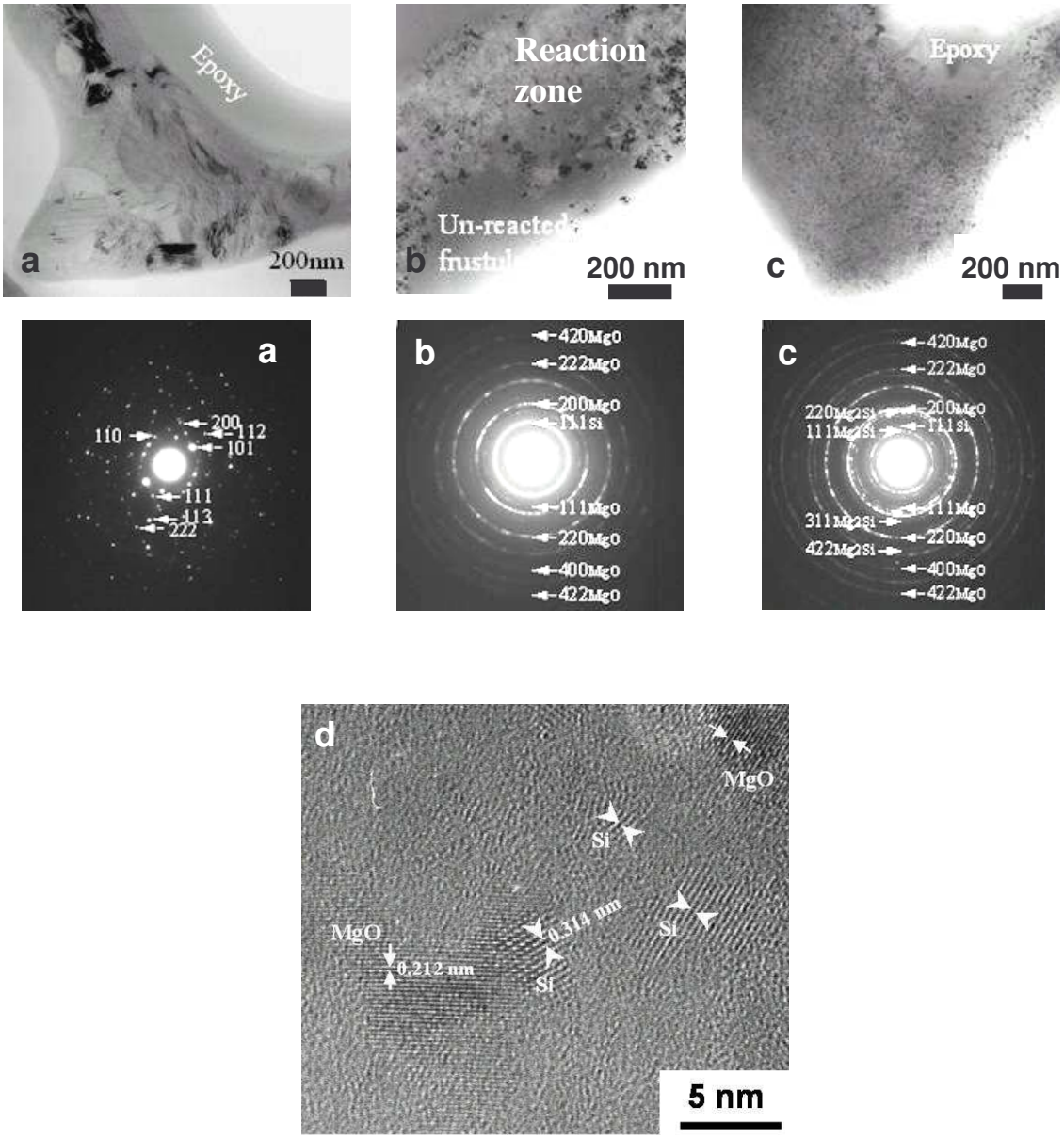


Figure 1.18. Reaction interface between $SiO_2$ and MgO + Si in 10:1 Mg:$SiO_2$ starting molar ratio. a.) TEM of unreacted *Aulacoseira* (flame polished) diatom frustule after 1 hour at 650°C using 10:1 Mg:$SiO_2$. b.) TEM of 650°C reaction interface between MgO/Si and $SiO_2$. (c) fully converted frustule after 2 hours at 650°C bearing MgO, Si and $Mg_2Si$, (d) High resolution TEM of MgO and Si particles in 650°C, 2 hr sample.

## 1.4 Conclusion

In summary, the process of using silica templates for producing 3D-microfabricated magnesium oxide structures has been investigated with regard to processing effects on particles size, surface area and phase composition of the product. The average particle size of MgO in the converted frustules was found to increase from 15 nm to 80 nm as reaction temperature was varied from 550° to 900°C. In the same temperature range, the particles size of the Si product increased from 23 to 89 nm average particle size. The particle size of MgO was found to increase when the silicon byproduct formed $Mg_2Si$. At 650°C, the particle size of MgO increased from 13 nm to 23 nm for Si versus $Mg_2Si$ byproduct respectively. At 900°C, the particle size of MgO increased from 65 to 89 nm for Si versus $Mg_2Si$ byproduct respectively. The morphology of the magnesium silicide product at 600°C was a coarse angular-grained material coating the frustules. At 900°C the $Mg_2Si$ appeared to have coarsened or solidified from a melt. Manipulation of the processing parameters – time, temperature and reactant ratio – showed that the magnesium-vapor reaction with silica was robust for creating shape preserved nanocrystalline MgO structures from the silica templates of silica diatom frustules.

# CHAPTER 2

# SELECTIVE ETCHING OF SILICON FROM MAGNESIUM OXIDE STRUCTURES PRODUCED FROM SILICON DIOXIDE TEMPLATES VIA THE BaSIC PROCESS

## 2.1 Introduction

The conversion of silica micro-structures, such as diatom frustules and silica fibers (with 5 to 50 μm maximum dimensions and features below 100 nm), into magnesium oxide through a gas displacement reaction, with remarkable preservation of shape has recently been demonstrated[10, 19, 44-46, 60]. The reactions were demonstrated for individual diatom and fiber structures on iron substrates. These reactions were performed between 650 and 900° C and evolved elemental silicon as a byproduct. When excess magnesium vapor was present for the reaction, magnesium silicide ($Mg_2Si$) was formed. In the case where the atmosphere was saturated with magnesium vapor, the silicon from individual diatom or microfiber specimens was expelled from the newly formed magnesium oxide structure as an Mg-Si liquid. The liquid preferentially wetted the iron substrate supporting the structures. In this manner, a magnesium oxide product of reduced silicon content was obtained.

As the process was scaled to produce gram quantities of magnesium oxide structures in a powder bed, the volume of silicon by-product liquid that could be produced was dependent on the amount of excess magnesium present. The reaction proceeded to the point of producing elemental silicon or magnesium silicide, but without excess Mg vapor, no liquid could form to carry the silicon out of the frustule. The silicon remained incorporated with the new MgO structures, some of it appearing on the

structure surface as fine crystallites. The silicon crystallites may have been pushed to the surface as a result of stresses associated with the volume expansion as 1 mole of silica was converted to 2 moles of MgO and 1 mole of Si. Where magnesium silicide formed, coarsening of the by-product occurred, by the introduction of a liquid phase transport system as indicated in the Mg-Si phase diagram[59] (Chapter 1, Figure 1.17). The liquid could have facilitated the extrusion of the silicide from the frustules. Compressive forces from the higher elastic modulus MgO resisting the volume increase in the conversion from Si to $Mg_2Si$, may have also facilitated the expulsion of the intermetallic from the interior regions of the frustules. Figure 2.1 shows the morphology of the diatom frustules and byproducts in the starting silica structure and MgO structures with either Si or $Mg_2Si$ by-products.

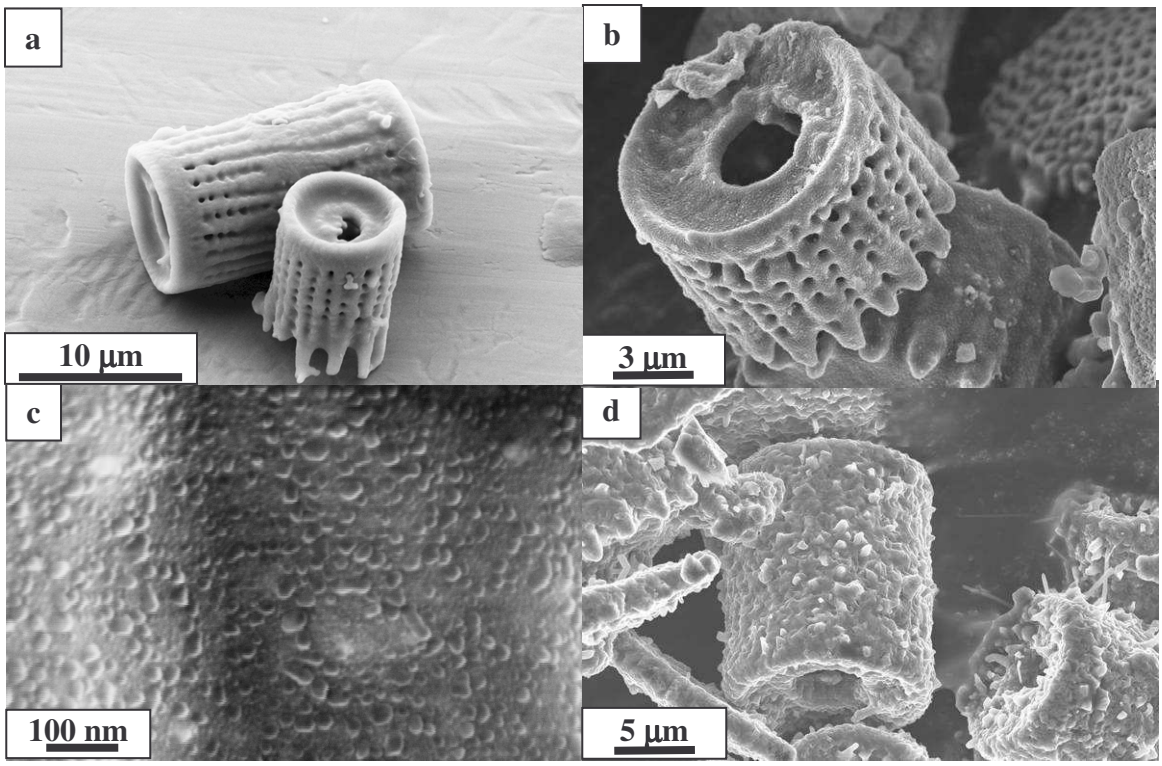


Figure 2.1. SEM images of (a) silica *Aulacoseira* diatom frustule (XRD in Figure 1.1), (b) magnesium oxide and silicon diatom frustule converted at 900°C in 1.5 hr using a 2.45:1 molar ratio of the Mg and $SiO_2$ reactants (c) high magnification of Si grains on surface of magnesium oxide frustule, (d) magnesium silicide coating on diatom frustule from conversion at 600°C in 3 hr using a 10:1 molar ratio of the Mg and $SiO_2$ reactants.

Whether Si or $Mg_2Si$ byproduct were produced in the MgO conversion process, methods were required to remove the silicon or silicide while preserving the integrity of the MgO structure in order to produce bulk quantities of phase pure magnesium oxide frustules. The solutions to this problem may find applicability in the processing of silicon on magnesium oxide substrates, or vice versa, for device manufacturing and in other scenarios where silicon removal is required without damaging MgO structures.

In many potential applications using the magnesium oxide diatom frustules, remnant silicon or magnesium silicide would almost certainly have an adverse affect on

the properties and/or performance of the product. For example, the magnesium oxide diatom frustules may prove to be efficient chemisorbent materials for $SO_x$ and $NO_x$ emissions. In filtration applications, magnesium oxide diatoms could be employed for their positive surface charge and ability to adsorb heavy metals such as chromium dissolved in water streams. As a catalyst support, magnesium oxide frustules impregnated with a surface layer of molybdenum oxide catalyzes the reduction of $H_2S$ emissions to elemental sulfur at room temperature[25]. In each of these applications, a silicon coating on the particle surface would reduce the specific surface area and thus the specific activity of the magnesium oxide for the applications.

Biologically derived structures can be produced using a variety of chemistries by employing sol gel coatings or further BaSIC reactions to the magnesium oxide templates. Barium titanate films can be formed from sols deposited on MgO substrates[21]. Piezoelectric thin films of barium titanate are commonly grown on magnesium oxide substrates due to low epitaxial strain between MgO and $BaTiO_3$ single crystals. Additive reactions with the magnesium oxide frustules can produce binary ceramic structures of materials such as $MgWO_4$ (Chapter 3). In these scenarios, unwanted silicon may cause strain and spalling of films, reaction with the new chemistry, creating undesirable secondary phases that detract from the properties of the intended product.

In addition to substrates of magnesium oxide, the BaSIC process may potentially be used to fabricate microdevices from $SiO_2$ templates for specific applications using materials such as SrO, CaO and $Li_2O$ [10]. For any such materials where the BaSIC reaction involves reduction of the $SiO_2$ by a metallic vapor, a solid silicon product will accompany the new oxide. Analogous processes to those discussed in this chapter

regarding the silicon products of the MgO process will be required to produce phase pure structures of these materials.

Numerous methods exist in the literature for removing silicon, many of which were developed for use in the semiconductor industry and often based on the selective etching of silicon over silicon dioxide[61]. These methods include chemical etching by atomic halogens, plasma assisted etching with chlorine, carbon tetrachloride or sulfur hexafluoride. Several of these techniques have been developed for etching extremely fine patterns in silicon. The interest in this case was to remove silicon from complex structures while sparing the magnesium oxide substrate. For solutions to this problem, I chose to investigate and compare three chemical methods. The first two were aqueous methods whereby silicon is etched with sodium hydroxide, or secondly whereby magnesium silicide is etched by hydrochloric acid (Table 2.1). The third method was borrowed from semiconductor processing and employed chlorine or anhydrous hydrogen chloride gas to remove elemental Si and the Si-component of $Mg_2Si$ as silicon tetrachloride vapor (Table 2.2). To determine if $Cl_2$ and HCl were candidates for removing silicon without any reaction with the MgO structure, the standard Gibbs free energies of the reactions of the gases with MgO were compared in Table 2.3.

Table 2.1. Aqueous dissolution formulae for silicon and magnesium silicide.

| |
|---|
| $Si + 2NaOH + H_2O \rightarrow Na_2SiO_3 + 2H_2$ |
| $Mg_2Si + 4HCl\ (aq) \rightarrow SiH_4 + 2MgCl_2\ (aq)$ |
| $SiH_4 + 2H_2O \rightarrow SiO_2 + 4H_2$ |

Table 2.2. Formation energies for chlorine and hydrogen chloride decomposition of silicon byproducts[58, 62].

| Reaction | $\Delta G_{27°C}$ (kJ/mol-K) | $\Delta G_{527°C}$ (kJ/mol-K) |
|---|---|---|
| $Si + 2Cl_2 \rightarrow SiCl_4$ | -622.5 | -556.6 |
| $Si + 4HCl \rightarrow SiCl_4 + 2H_2$ | -241.3 | -158.8 |
| $Mg_2Si + 4Cl_2 \rightarrow 2MgCl_2 + SiCl_4$ | -1729.3 | -1509.9 |
| $Mg_2Si + 8HCl \rightarrow 2MgCl_2 + SiCl_4 + 4H_2$ | -966.8 | -714.3 |

Table 2.3. MgO compatibility, in terms of free energy, with $Cl_2$ and HCl gases[58, 62].

| Reaction | $\Delta G_{27°C}$ (kJ/mol-K) | $\Delta G_{270°C}$ (kJ/mol-K) | $\Delta G_{527°C}$ (kJ/mol-K) |
|---|---|---|---|
| $2MgO + 2Cl_2 \rightarrow 2MgCl_2 + O_2$ | 11.0 | 23.2 | 36.1 |
| $MgO + 2HCl \rightarrow MgCl_2 + H_2O$ | -35.2 | ± 0 | 31.457 |

## 2.2 Experimental Materials and Procedures

Finely structured magnesium oxide diatoms were produced by reacting silica diatomaceous earth (Recreational Water Products, Stockdale, GA) with magnesium vapor inside a 1020 carbon steel ampoule (TW Metals, Forest Park, GA) that was TIG welded shut at both ends. Heat treatments were applied for 1.5 hour at 1.) 650°C in a 10 cm ampoule, with 0.1 gram diatoms in an iron boat on top of a 0.6 gram Mg granule bed, or 2.) 900°C in a 20 cm ampoule with diatoms in a 0.6 gram powder bed at the opposite end of the ampoule from 0.6 gram of Mg granules, separated by a crimp in the ampoule to prevent the flow of Mg liquid to the diatom end of the ampoule. From each reaction mixtures of MgO with mostly Si byproduct or MgO with mostly $Mg_2Si$ byproduct were obtained for use in the byproduct removal studies. The reaction products were analyzed by X-ray diffraction (XRD) (Philips PW 1800), scanning electron microscopy (SEM)

(Hitachi S-800) and XPS (SSX-100 Esca Spectrometer, Surface Science Instruments) both prior to and after by-product removal using an 800 μm spot size.

### 2.2.1 Silicon Removal: Sodium Hydroxide Etch

MgO diatom frustules with Si as the major by-product were etched using a stoichiometric amount of NaOH (Alfa Aesar, 97-100%) required to fully oxidize the Si to $Na_2SiO_3$. The NaOH was assayed in the lab and found to be 92% pure by weight (See Appendix C). The content of Si in diatom frustules upon the complete reduction of silica is calculated to be 25. 4 wt % when Si is the sole byproduct. The etching was performed in a 60ºC ultrasonic bath for up to 3 hours. The sodium silicate was removed by boiling the etched frustules in 50 ml deionized water for 20 minutes and filtering the frustules.

### 2.2.2 Magnesium Silicide Removal: Hydrochloric Acid Etch

The amount of acid to add required to digest the $Mg_2Si$ in the frustules was calculated from the reaction where Mg vapor reacts with silica to form MgO and $Mg_2Si$. When only $Mg_2Si$ byproduct is formed (no Si), the product will be composed of 74 % $Mg_2Si$ by weight. MgO frustules with $Mg_2Si$ as the primary by-product were magnetically stirred in acetone in a round-bottom flask. After purging the flask with flowing argon, 1.0 N HCl was added in 0.5 ml increments. The solution was stirred until bubbling of $SiH_4$ or $H_2$ from the reaction ceased. After cessation of bubbling, another 0.5 ml of 1.0 N HCl was added. The addition and stirring process was repeated until all the acid was added to the system. The system was continually flushed with argon to remove

the product gases. The $MgCl_2$ product of the decomposition was later dissolved and filtered away with deionized water.

### 2.2.3 Chlorine Gas Etch

MgO frustules bearing mixtures of silicon and magnesium silicide were placed in a 99.8% alumina crucible, 50mm long, 12mm wide, 9mm tall, (Vesuvius McDanel, Beaver Falls, PA) inside a 1" quartz tube sealed with Monel Alloy 400 (C. G. Metals, Duluth, GA) end caps and fluorosilicone o-rings (Marco Plastics, Andover, MA) in a clamshell tube furnace (Figure 2.2). Ultra high purity $Cl_2$ gas (99.9 % Matheson Tri Gas, Montgomeryville, PA) was plumbed through PFA and Teflon tubing and fixtures (Swagelok, Alpharetta, GA) and passed over 2 mm deep beds of frustules at temperatures from 350° to 550ºC. The furnace was purged with ultra-high purity argon (Airgas South, Atlanta, GA) and to remove $SiCl_4$ and excess $Cl_2$ vapors after reaction. The chlorine and argon gases were controlled with Matheson Trigas flowmeters and backflow arrestors were used to prevent flow of argon into the chlorine gas tank and vice versa. The halogen vapor products were neutralized by a gas scrubber built in-house, containing sodium thiosulfate (Alfa Aesar) and activated carbon (Alfa Aesar, 200 mesh) in a 30" long, 1" diameter quartz tube sealed with Monel (nickel) end caps.

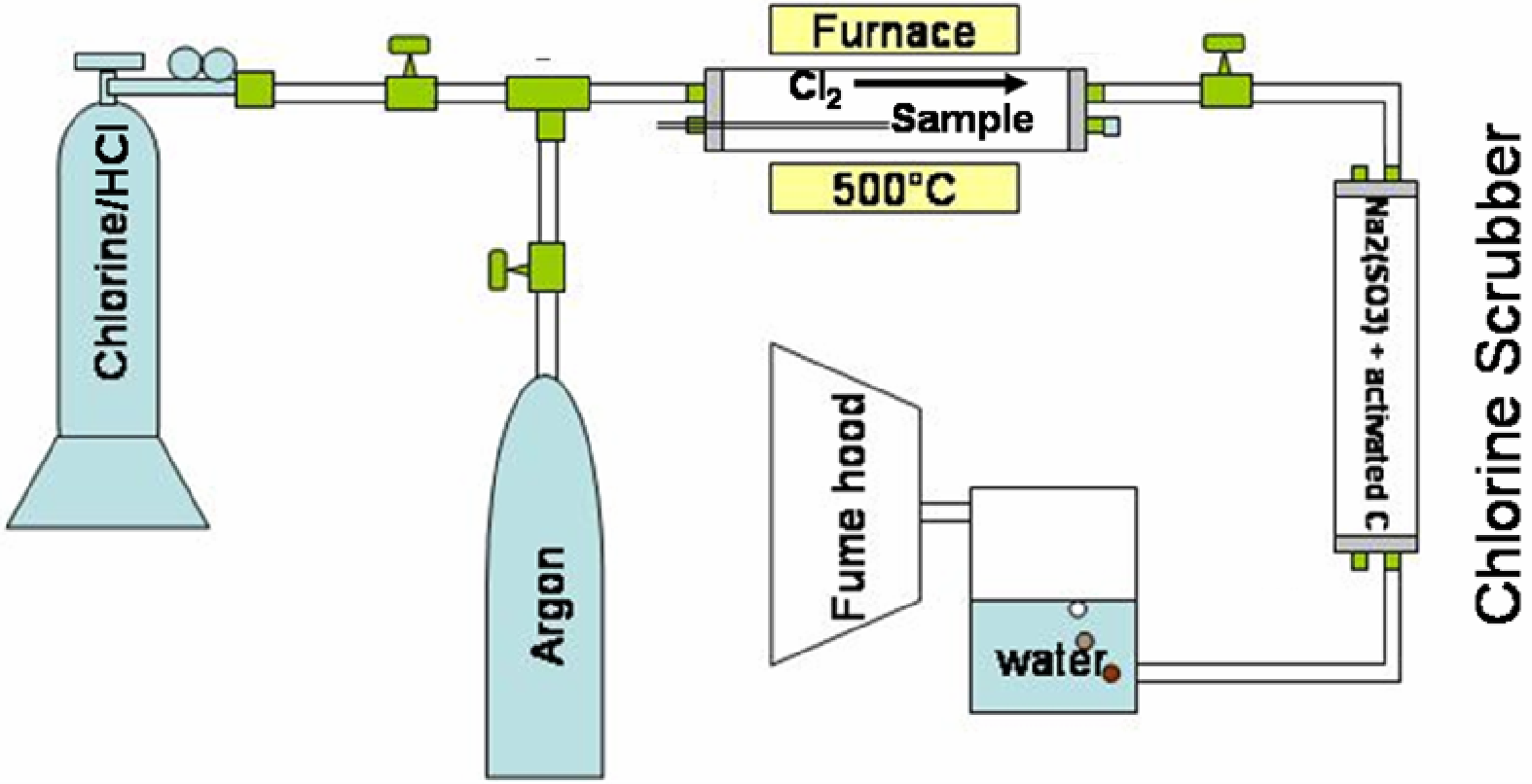


Figure 2.2. Schematic of chlorine gas furnace assembly built for $Cl_2$ etching of silicon and magnesium silicide byproducts of the MgO BaSIC reaction.

## 2.3 Results and Discussion

### 2.3.1 Silicon Removal: Sodium Hydroxide Etch

The etching time of silicon with sodium hydroxide at 60°C was restricted to 3 hours to limit hydration of the MgO. SEM showed frustules free of the Si nodules that were present on the surfaces of un-etched samples (Figure 2.3). EDS analysis showed reduced silicon content and no remaining sodium in the frustules after reaction compared with the starting MgO/Si frustules (Figure 2.4). The XRD pattern of the MgO frustules complemented the EDS data showing reduced silicon content in the sodium hydroxide treated materials (Figure 2.5). Using the Rietveld quantitative analysis function in Panalytical High Score Plus software, the silicon content was determined to be reduced from 16% to 1% by treatment in sodium hydroxide for 3 hours at 60°C. In cases where $Mg_2Si$ was present in the starting MgO material, the peak at 40º 2θ in the post-etched sample, corresponding to the $Mg_2Si$, was unaffected by the alkali etch, demonstrating the ineffectiveness of the etchant for removing $Mg_2Si$. The XRD pattern for the sodium silicate filtrate showed only crystalline sodium carbonate; although EDS of the filtrate revealed the presence of silicon (Figure 2.6). This was accounted for by the amorphous nature of the sodium silicate. It is unclear at what stage the carbonate evolved as the starting NaOH material assayed as 95.9% NaOH with only 0.4% $Na_2CO_3$ (balance $H_2O$) using the ACS method for NaOH assay. The residual silicon in the MgO frustules may have been the result of an inadequate supply of NaOH due to carbonation of the NaOH from "old" deionized water which had absorbed significant $CO_2$ from the lab air. The filtration process appeared to be effective at removing sodium, as none was detected in the EDS of the treated frustules. The SEM of the NaOH treated frustules showed

relatively good preservation of shape through the etching step. However some of the finer features (pores, ridge lines) appear "smoothed over" or less well defined than the pre-etch frustules. In some instances destructive etching of the frustule is apparent such as in the upper center region of Figure 2b.

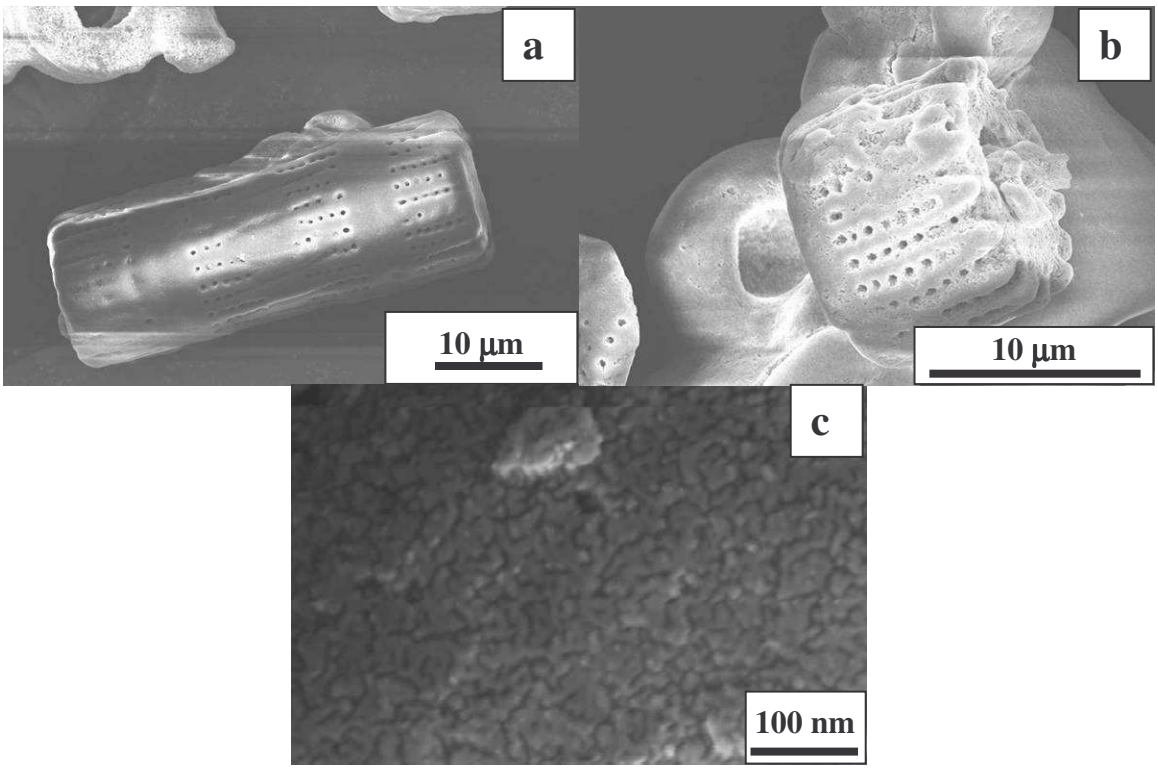


Figure 2.3. SEM images of (a, b) MgO frustules produced at 900°C in 1.5 hr with 2.45:1 molar ratio of Mg and $SiO_2$ reactants, after removal of silicon with sodium hydroxide (3 hours, 60° C), (c) High resolution image of MgO microstructure.

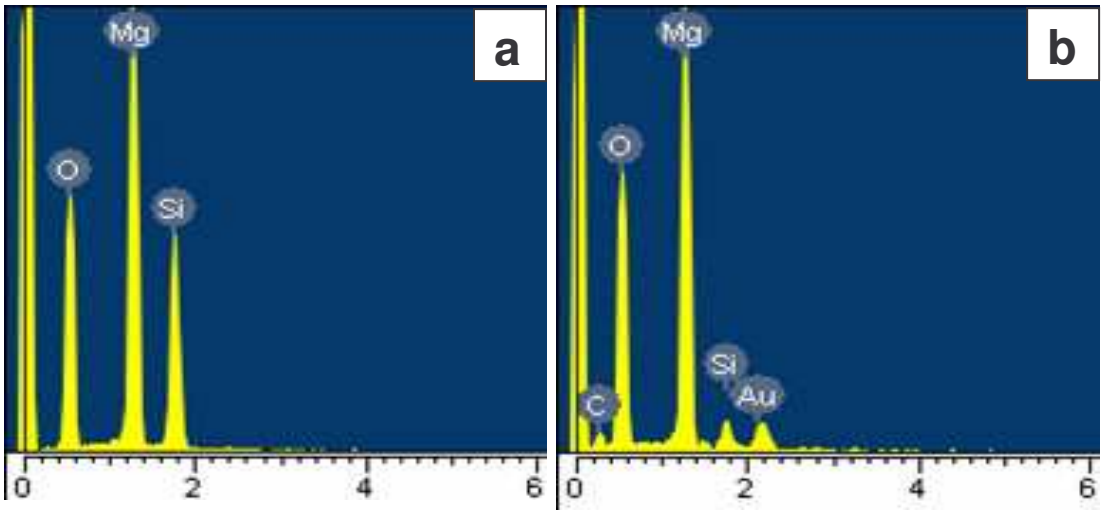


Figure 2.4. EDS of MgO/Si frustules (a) after conversion at 900°C for 1.5 hour with 2.45:1 ratio of the Mg and $SiO_2$ reactants, and (b) after dissolution of Si in sodium hydroxide solution at 60°C for 3 hours.

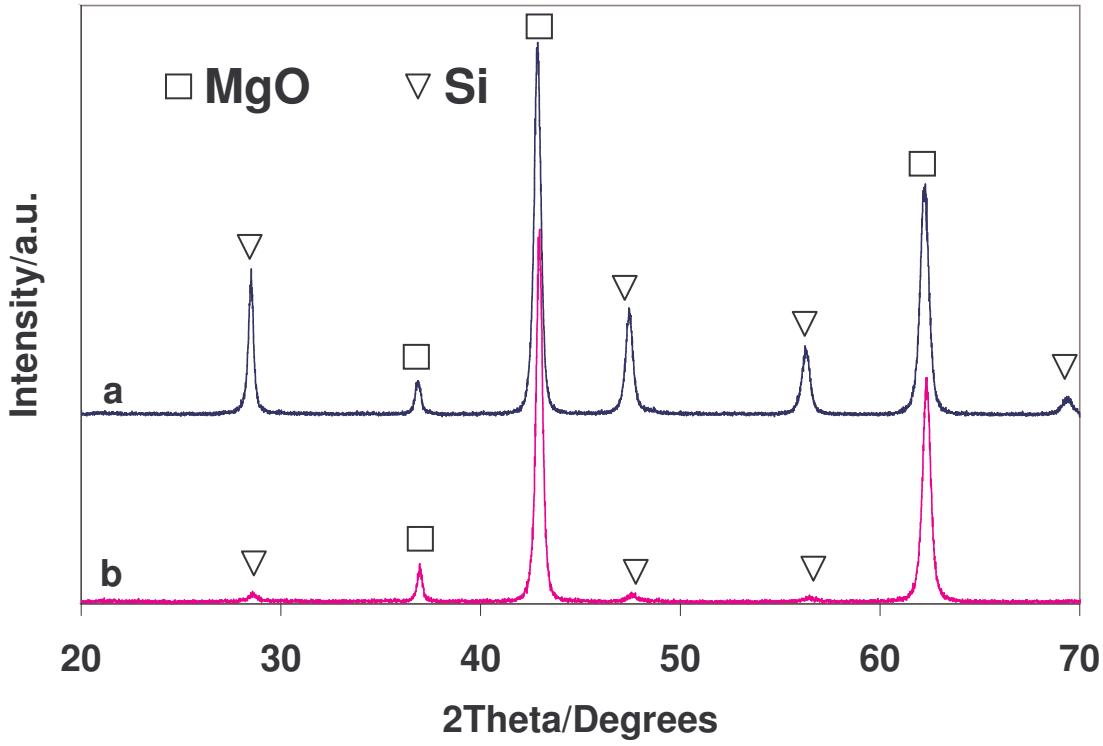


Figure 2.5. XRD of (a) magnesium oxide/silicon frustules produced at 900°C in 1.5 hr with a 2.45:1 molar ratio of the Mg and $SiO_2$ reactants, producing about 16 % Si, and (b) magnesium oxide frustules after etching with sodium hydroxide solution at 60°C for 3 hours, bearing approximately 1 % Si, quantified by Rietveld analysis.

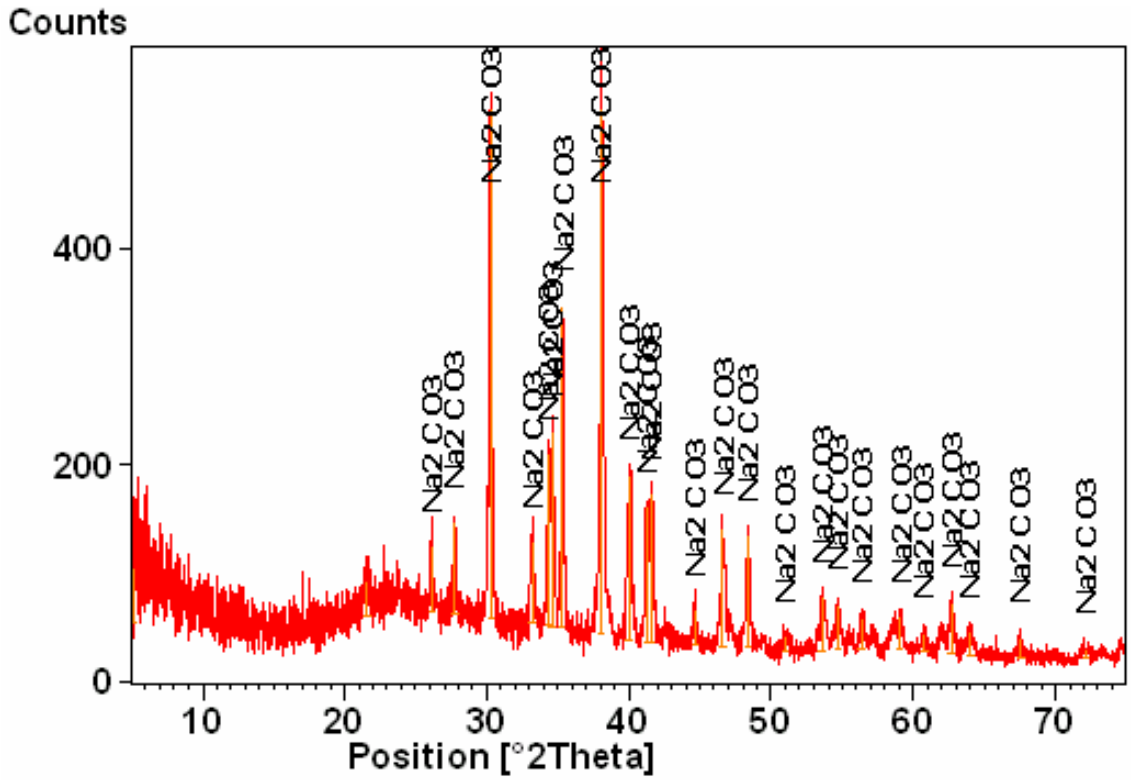


Figure 2.6. Filtrate from NaOH etching process (a) XRD showing the crystalline phase $Na_2CO_3$ and an amorphous rise in the background due to sodium silicate, (b) EDS showing the silicon removed from the MgO frustules by the sodium hydroxide.

### 2.3.2 Magnesium Silicide Removal: Hydrochloric Acid Etch

The $Mg_2Si$ dissolution using hydrochloric acid failed to adequately remove the $Mg_2Si$ phase and was found to have destructive consequences for the shape of the MgO structures. For partially etched samples, using one half the hydrochloric acid calculated for decomposing all the $Mg_2Si$ present in the sample, SEM revealed interesting patterns in the $Mg_2Si$ where polycrystalline nanofiber and nano-cellular structures were produced with individual particle sizes as small as 10 nm (Figure 2.6). In this case the $Mg_2Si$ decreased relative to the amount of MgO as seen in the XRD (Figure 2.7). When the entire amount of HCl was added for the purpose of removing the silicide, a significant amount of silicide remained and a new phase, $Mg_2(OH)_3Cl{\cdot}4H_2O$, appeared. The new phase appeared to form from the MgO, as the MgO peak decreased relative to the remaining $Mg_2Si$. Apparently after the coating of $Mg_2Si$ on the particles is removed by etching, the hydrochloric acid preferentially dissolves MgO rather than decomposing the remaining $Mg_2Si$. Overall, aqueous methods for removing $Mg_2Si$ from MgO were found to be inadequate in both removal ability and shape preservation.

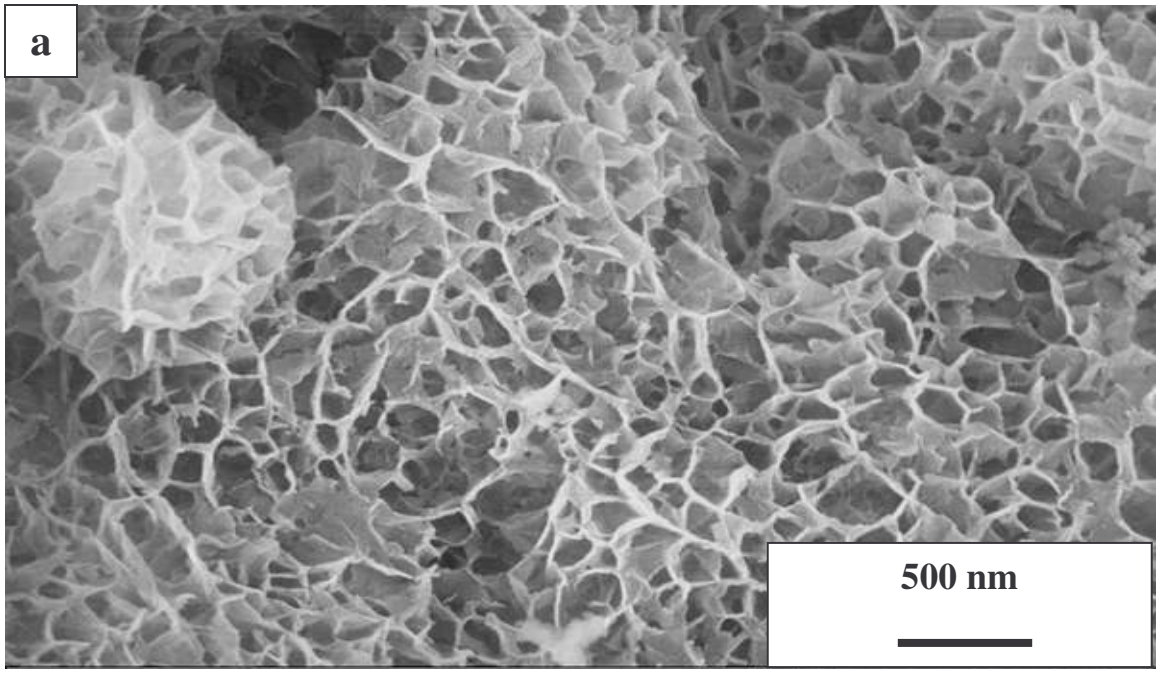
a
500 nm

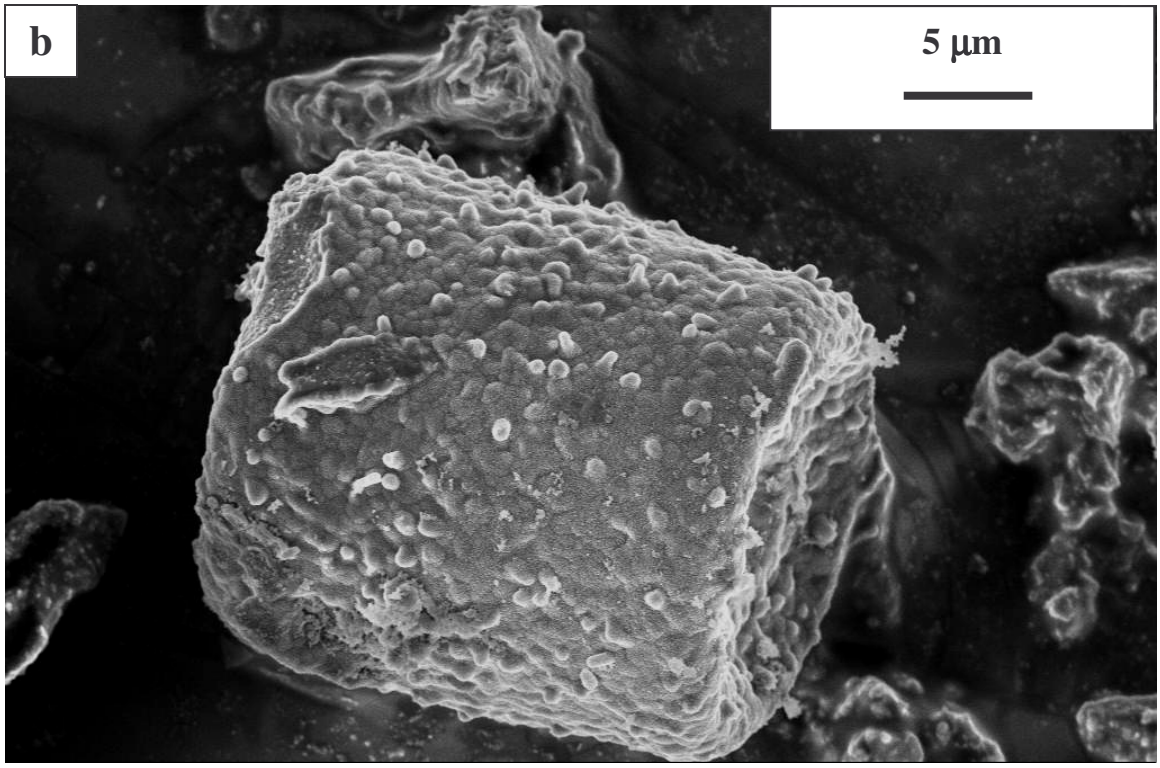
b
5 µm

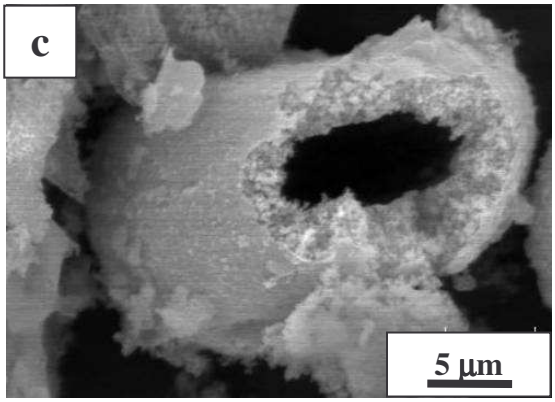


Figure 2.7. SEM of $Mg_2Si$ bearing MgO diatoms treated by HCl etching, (a) (previous page) partially etched $Mg_2Si$ (30 minutes, only half HCl needed for full dissolution) showing nanocellular structures, (b) MgO frustule after partial etching showing frustule microstructure exposed from removal of the silicide coating. (c) MgO frustule from after further etching (XRD Figure 2.7c) showing damage caused by HCl etching the MgO.

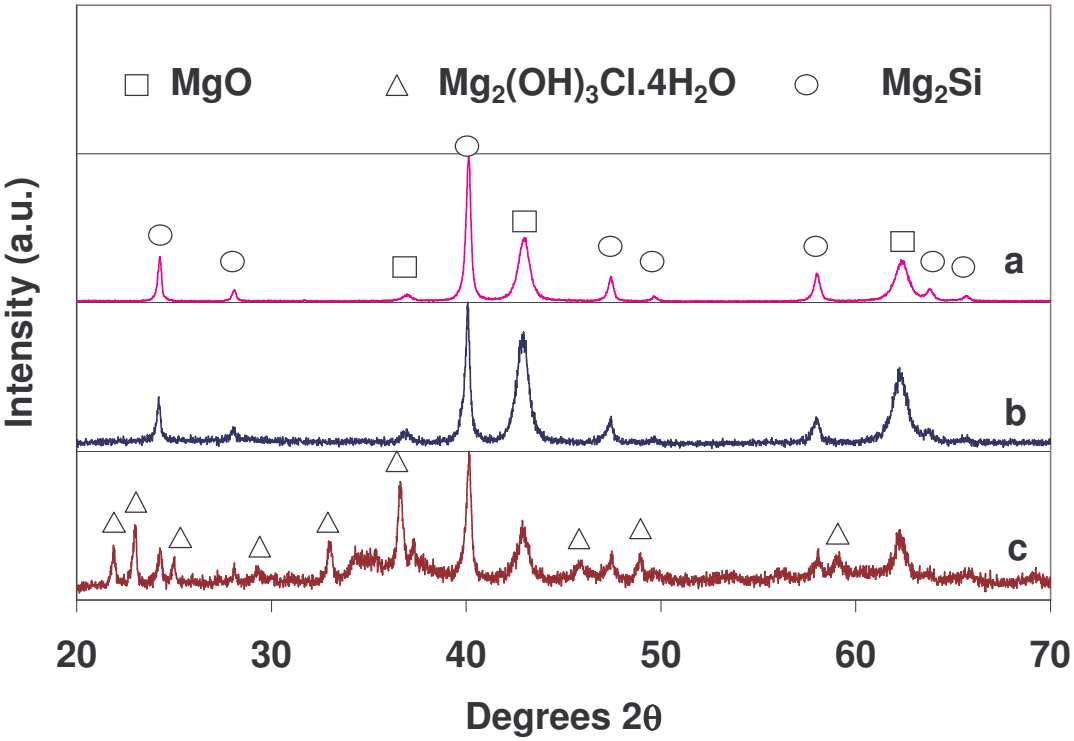


Figure 2.8. (a) MgO with $Mg_2Si$ product after 1.5 hr at 650°C and 10:1 molar ratio of Mg and $SiO_2$ reactants, (b) After treatment with one-half the HCl need to decompose all the $Mg_2Si$ at room temperature for 30 minutes. The $Mg_2Si$ content reduced relative to the MgO content, decreased from 43 to 29 wt % according to Reitveld analysis. (c) Addition of the remaining HCl required for $Mg_2Si$ decomposition leads to formation of $Mg_2(OH)_3Cl.4H_2O$, and loss of MgO relative to residual $Mg_2Si$ after 30 minutes.

### 2.3.3 Chlorine Gas Etch

After exposing MgO frustules with Si and/or $Mg_2Si$ byproducts to chlorine gas above 350°C, the powder was found to change from either black or blue color, respectively, to a light tan color. The chlorine treated frustules gradually increased in mass and clumped together after exposure to air. This suggested the presence of magnesium chloride ($MgCl_2$) in the frustules. Therefore the samples were soaked in deionized water and filtered to completely remove any $MgCl_2$. The $MgCl_2$ was attributed to $Mg_2Si$ which would exist to some extent in any nearly sample of converted MgO. X-ray diffraction analysis of the MgO frustules showed that both silicon byproducts were successfully removed by the chlorine gas without loss of the MgO phase. Figure 2.9 shows the XRD patterns for (a) a primarily $Mg_2Si$ containing MgO sample, and (b) a primarily Si containing MgO sample after 0.5 hour chlorine treatments at 550°C followed by dissolution of $MgCl_2$ with deionized water.

Regardless of which silicon byproduct was present in the starting MgO frustules, the chlorine gas removed the materials from the surfaces of the diatoms while preserving the MgO morphology as seen in Figures 2.10 and 2.11. Higher magnification revealed the individual MgO grains on the order of 100 nm in accordance with the grain sizes determined by the Williamson-Hall method from XRD patterns in Chapter 1.

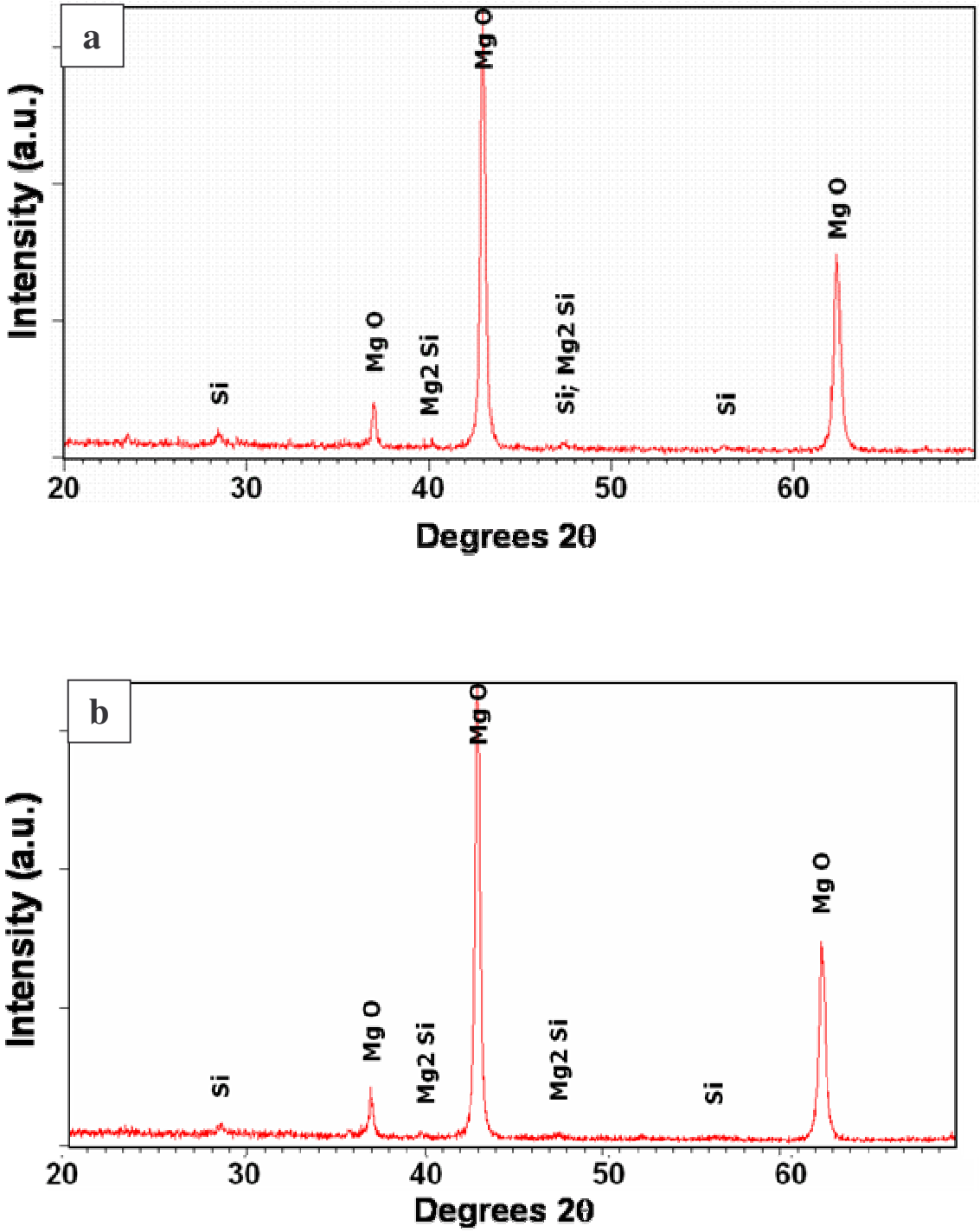


Figure 2.9. XRD patterns of (a) MgO with $Mg_2Si$ byproduct and (b) MgO with Si byproduct after being treated at 550° for 0.5 hour with chlorine gas at 1 atmosphere pressure. Note that after treatment only trace amounts of $Mg_2Si$ and Si are detected. At the same time, the XRD pattern provides evidence that the MgO was not attacked by the $Cl_2$ gas.

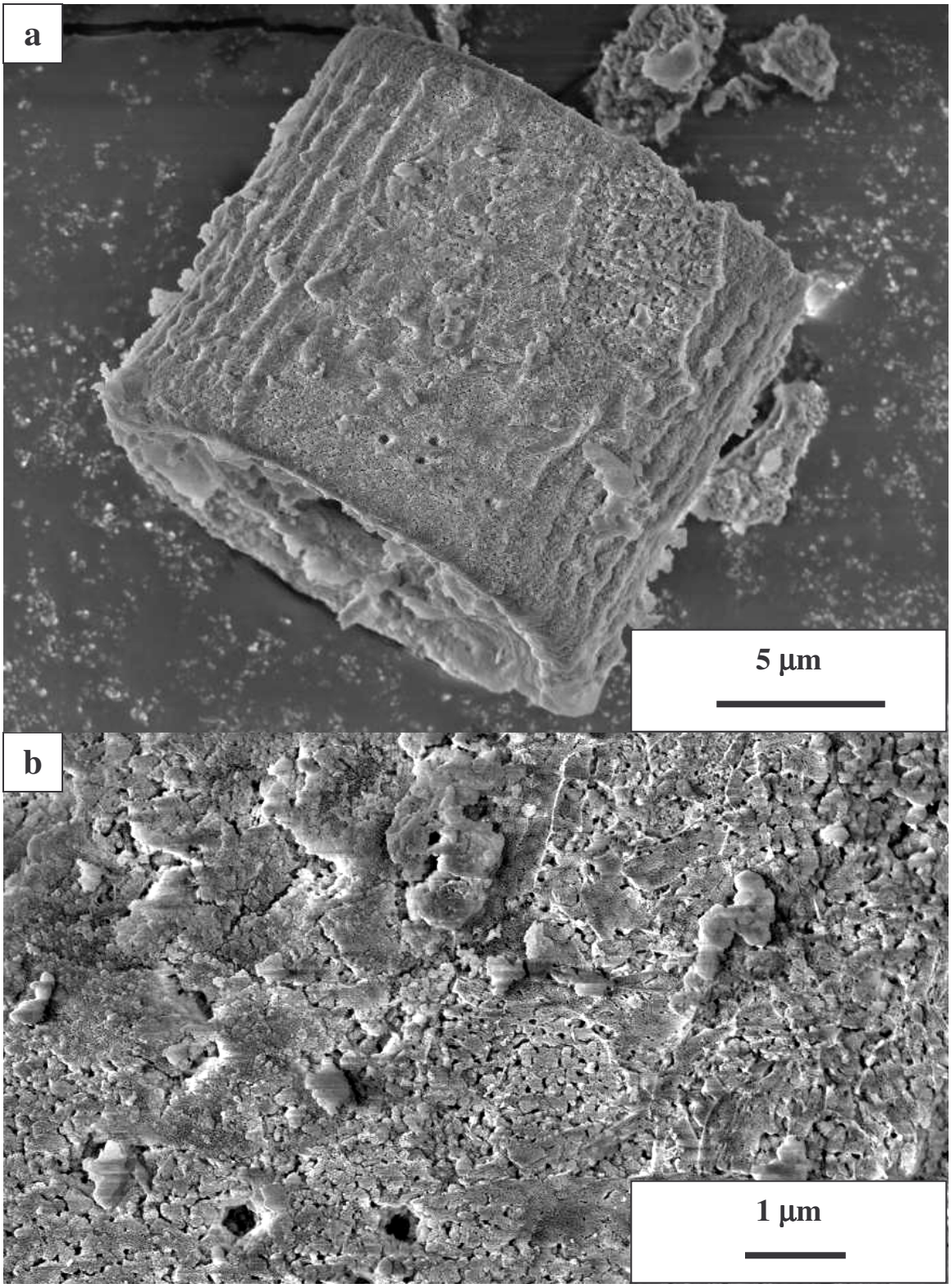


Figure 2.10. SEM of an MgO with $Mg_2Si$ *Aulacoseira* diatom frustule produced at 900°C in 1.5 hour after etching the silicon with chlorine gas at 550°C for 0.5 hour. (a) shows shape retention of the MgO structure after chlorine treatment and (b) shows the nano-sized grains of the MgO microstructure.

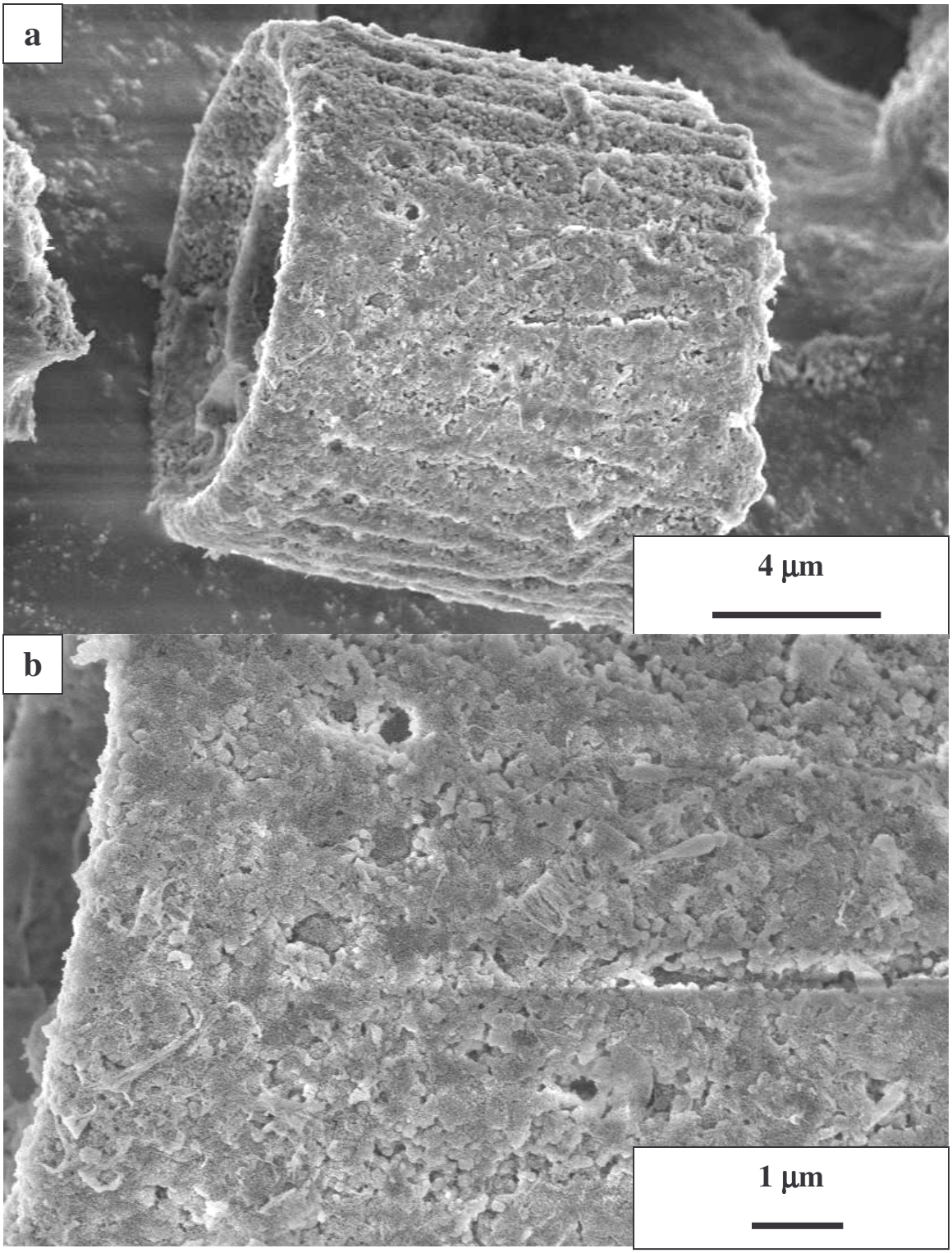


Figure 2.11. SEM of an MgO with Si *Aulacoseira* diatom frustule produced at 900°C in 1.5 hour after etching the silicon with chlorine gas at 550°C for 0.5 hour. (a) shows shape retention of the MgO structure after chlorine treatment and (b) shows the nano-sized grains of the MgO microstructure.

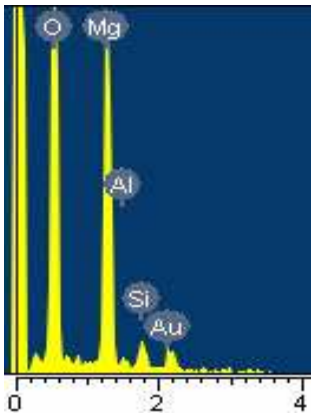

Figure 2.12. EDS of MgO with $Mg_2Si$ diatom frustule after chlorine treatment at 550°C for 0.5 hour.

### 2.3.4 Thermodynamic Analysis of Vapor Etching

Chlorine gas was predicted to result in silicon vaporization as silicon tetrachloride ($SiCl_4$) without attacking MgO. The reaction of pure $Cl_2$ gas at 1 atm pressure with Si has strongly negative standard Gibbs free energy from room temperature to 527°C (-623 to -557 kJ/mol-K), though many sources report temperatures greater than 300°C are required to penetrate the native oxide coating of the silicon particles and activate the reaction. Several sources report chlorine as an extremely effective tool for removing silicon above 400°C[63-65]. The standard Gibbs free energy of the MgO and $Cl_2$ reaction is positive Gibbs free energy over the same temperature range from 11.0 to 36.1 kJ/mol-K, using Barin's data for MgO adjusted according to Gourishankar's corrections[58, 62]. If Barin's MgO data is used, the standard Gibbs free energy for the reaction of MgO with $Cl_2$ is only positive above 500°C. Because of the sensitivity of this reaction to thermodynamic error in Barin, Gourishankar's correction was tested by firing SiO with Mg at 827°C for 3 hours and quenching. The formation energy for SiO used in the calculation was obtained from Schnurre[54]. At 827°C, if the Barin data were correct for MgO, no reaction would take place, however if Gourishankar's data were correct, the Mg

would reduce the SiO at that temperature. The resulting material from the experiment showed reaction to form MgO, Si and $Mg_2Si$, validating the Gourishankar correction. The implication for the chlorine etching process is that the etching process can be performed at any temperature without bringing harm to the MgO.

Thermodynamics also support the decomposition of $Mg_2Si$ with chlorine gas to form $SiCl_4$ gas and $MgCl_2$, a water soluble salt. The standard Gibbs free energy of the reaction from R.T. to 527°C increases from -1729 to -1510 kJ/mol-K. The implication of this attribute of the silicon etching process is that for producing phase pure MgO frustules, either silicon byproduct, Si or $Mg_2Si$, is acceptable. Thus large quantities of MgO frustules could be processed with regard only to complete reaction of the starting silica diatoms, rather than focusing on the composition of the silicon products of the reaction.

Hydrogen chloride gas should react with $Mg_2Si$ and Si at and above R.T. At R.T. pure HCl gas should react with MgO to form $MgCl_2$ and $H_2O$ with a standard Gibbs free energy of -35.2 kJ/mol-K. However, above 270°C, any reaction of MgO with pure HCl gas should not occur because the free energy becomes positive. In fact, at 327°C the standard Gibbs free energy of pure HCl gas at 1 atm pressure reacting with MgO is 8.62 kJ/mol-K. Therefore HCl is another candidate for the decomposition of Si and $Mg_2Si$ without attacking the MgO frustules. In the presence of HCl gas, $Mg_2Si$ should decompose to $SiCl_4$ vapor and water soluble $MgCl_2$. Thus, like $Cl_2$ gas, HCl could be used as a silicon byproduct-independent etchant for the production of phase pure MgO diatom frustules.

The halogen reactions provide several distinct advantages over the aqueous method of byproduct removal. 1.) The silicon is removed as a gas rather than a

moderately soluble sodium silicate. 2.) Thermodynamically speaking, no deleterious effects to the MgO structure should occur (nor did they occur) with the halogen etch. 3.) The most significant advantage is that there is no need to tailor the silicon by-product if Si and $Mg_2Si$ are both attacked by the halogen gases. In addition, the $SiCl_4$ and $H_2$ generated from these reactions in a large scale operation could be collected as a means of capital recovery. For example, the hydrogen evolved from the use of HCl could be used to power fuel cells which power the process.

## 2.5 Conclusion

In summary, simple methods for extracting silicon from complex magnesium oxide structures were investigated. Sodium hydroxide was found to etch silicon but contributed to some degradation of the MgO structures and did not have an effect on $Mg_2Si$. Hydrochloric acid was found to be an unacceptable etchant for magnesium silicide in the presence of MgO, as the MgO is attacked in the acidic environment. The most successful etchant found was chlorine gas, which successfully removed both silicon and $Mg_2Si$ without causing damage to the silicon frustule. The chlorine gas etching method revealed the fine grained and apparently high surface area microstructure of the MgO frustules that had been obscured by the presence of the silicon byproducts. Successful silicon removal methods will be increasingly important for the development and commercialization of high surface area oxides produced by the BaSIC method as new devices and applications are realized.

# CHAPTER 3
# CONTROLLED SHAPE MAGNESIUM TUNGSTATE PARTICLES FROM BIOLOGICALLY DERIVED SILICA TEMPLATES

## 3.1 Introduction

Phosphor materials are valuable for numerous applications in lighting, display technologies, microoptics, and photonics. In the production of commercial and novel phosphors, attention is often paid to the control of particle morphology. Uniformity of particle shape and size generally ensures high density and flatness of phosphor films and consistent luminescence throughout the material[4, 66-68]. Specific particle shapes may find use in certain optoelectronic devices where non-spherically shaped fluorescent particles could be advantageous (e.g. microtags, diffraction gratings).

A method for mass producing particles of various materials in specific complicated three dimensional shapes has been developed via chemical conversion of biological templates, (*i.e.*, the inorganic silica shells of diatom algae)[10, 21, 43-45, 60]. The 100,000 species of diatoms available as templates, each representing a unique particle structure, present a catalogue of possible highly specific particle structures available for materials applications. Many of the diatoms produce hollow pill-like structures or cylindrical rods yielding low bulk densities of diatomaceous earth powders[11-13, 16, 55, 69].

The shape controlled phosphor produced in this work is magnesium tungstate ($MgWO_4$). Magnesium tungstate has been commercially developed since the 1930s for use in phosphor screens for detecting x-ray and ultraviolet light, and for cathode ray tubes and television, persisting today as one of the primary phosphors in fluorescent lighting[70, 71]. The magnesium tungstate phosphor has generally been prepared by calcining blended

batches of high purity magnesium oxide and tungsten oxide precursors. Ideal processing parameters for maximizing phosphor brilliance are described in the literature by early researchers[72]. The literature shows that the brilliance of $MgWO_4$ phosphors is improved significantly by including two moles of MgO to every mole of $WO_3$[73]. It was originally reported that this composition yielded only $MgWO_4$ phase suggesting the incorporation of the additional MgO into the wolframite structure. This is unlikely as the MgO-$WO_3$ phase diagram shows no solid solution for MgO in $MgWO_4$. The early work was influenced by the large relative intensity of $MgWO_4$ compared to MgO in the XRD pattern and failed to see the MgO band in their Debye-Scherrer patterns[73, 74]. In this work, the MgO (200) peak was identified using a $\theta/2\theta$ XRD goniometer. Regardless of this misconception in the literature, the significant point is that a 2 to 1 composition of MgO to $WO_3$ may provide added brilliance. More recent research on the production of $MgWO_4$ powders by Bludsuss, *et. al.*, at the H.C. Stark Company showed that ammonium para-tungstate (APT) could be used as a precursor for many tungstate ceramics. Their work suggested the possibility of producing the tungstates at lower temperatures than possible with a tungsten oxide or tungstic acid source[75].

Apart from photoluminescence, recent literature on magnesium tungstate reported photo induced water splitting ability of tungsten oxide doped with magnesium oxide at room temperature[76]. The inherently high surface area of diatom frustules could enhance such catalytic activity.

The process for producing magnesium tungstate phosphor particles possessing a complex three dimensional structure has been coined “Bioclastic and Shape-preserving Inorganic Conversion” or BaSIC[10, 21, 43, 44, 60]. The BaSIC concept is that the complexity

of genetically reproduced structures could be harnessed for more technological applications if greater materials selectivity were present. New materials could be fabricated by producing a replica of the structure via displacement of the cations of the original chemistry with elements of the desired chemistry. Such a conversion process has been demonstrated with silica diatom frustules. For example, magnesium vapor displaces the silicon atoms in the silica structure to yield a magnesium oxide replica[10, 43, 44]. Titanium fluoride vapor has also been found to displace silicon in silica, yielding complex, shape-preserved titanium dioxide structures[60].

The magnesium oxide produced by the BaSIC method can be designed to have particle size ranging from 10 to 100 nm (Chapter 1). In recently published work, these MgO diatom replicas were used as substrates for photoluminescent and ferroelectric barium titanate ($BaTiO_3$) coatings[21]. MgO is a commonly used, ideal substrate for the growth of barium titanate films. By sol-gel methods, barium titanate coatings were applied uniformly at low temperatures. In contrast to a method where functionality may be added by coating, the MgO frustule can function as a precursor for Mg-containing binary ceramic compounds.

The development of a *BaSIC* process to produce $MgWO_4$ may lead to methods for producing highly shape-controlled powders in similar (Group II-VIB) binary compounds like magnesium chromate ($MgCrO_4$), magnesium chromite ($MgCr_2O_4$) and magnesium molybdate ($MgMoO_4$). One recent paper demonstrated the feasibility of using MgO doped with a monolayer of $MoO_3$, in an analogous process to Bludsuss' method for fabricating tungstate powders, to produce a catalyst for room temperature reduction of

hydrogen sulfide to sulfur[25]. In this work, a process has been developed for producing a photoluminescent binary oxide, $MgWO_4$, from the MgO replica of a diatom frustule.

## 3.2 Experimental Materials and Procedures

Silica diatoms were obtained as flame-polished diatomaceous earth (Recreational Water Products, Stockdale, GA), primarily of the genus *Aulacoseira*. The diatom frustules contained Ca, Na and Al impurities according to manufacturer data sheets and had a specific surface area of 1.9 $m^2/g$ (determined with Quantachrome BET surface analyzer). Magnesium flakes (99.5% metals basis), tungstic acid $H_2WO_4$ (99.9%) powder, ammonium *para*-tungstate (APT) ($(NH_4)_{10}W_{12}O_{41}\cdot xH_2O$) powder and sodium hydroxide pellets were obtained from Alfa Aesar. Thermogravimetric analysis and differential thermal analysis of the tungsten precursors and sodium hydroxide is provided in Appendix B. Iron tubing (1020 steel) measuring 2.5 cm ID by 20 cm length comprised the reaction ampoules for magnesium oxide production (TW Metals, Forest Park, GA). Iron was chosen for its relative inertness to magnesium (0.0875 at.% solubility of Fe in Mg at 900°C, a eutectic at 650.5°C with 0.0026 at.% Fe)[77]. Alumina crucibles, 98%, (80 mm long, 15 mm wide, 9 mm tall) (MTI Corp, Oakland CA) were used for $MgWO_4$ heat treatments.

For control experiments, 325 mesh MgO powder was obtained from Alfa Aesar and 325 mesh silicon powder from Johnson Matthey. $MgWO_4$ powder was obtained from Alfa Aesar for comparison of fluorescence properties.

Silica diatom frustules (0.6 grams) were packaged with magnesium granules (0.6 grams) and heat-treated at 900°C for 1.5 hours, in sealed iron ampoules[44]. The resulting

magnesium oxide diatoms and silicon by-product (approx. 1 gram) were treated in an ultrasonic bath at 60°C for 3 hours to reduce the silicon content of the material by etching, using 0.15 Molar sodium hydroxide in deionized water. Sodium hydroxide treated magnesium oxide diatoms were reacted with two types of tungsten oxide precursors – tungstic acid or APT.

(i). Magnesium oxide was blended in a 2:1 molar ratio with tungstic acid ($H_2WO_4$) in acetone, dried, heated at 600°C/hr to 1100°C and calcined for up to one hour in air[73]. Samples with 2:1 and 10:1 molar ratios of MgO to $WO_3$ were produced at 800° and 900°C for 2 hr. From another calcining method found in the literature, the a 2:1 blend of MgO and $H_2WO_4$ powders was calcined 0.5 hr at 875°C, quenched (pulled hot from the furnace and cooled), refired to 1250°C at 600°C/hr, cooled to 1000°C at 500°C/hr and quenched again[72].

(ii) Magnesium oxide diatoms were mixed with APT in a 2-to-1 molar ratio in deionized water and dried for 8 hours at 100°C. The powders were calcined at 500°, 800° and 1000° C for 2 hr each[75] in air, heated at 450°C/hr.

Control samples were produced whereby commercially obtained MgO, $WO_3$ and Si powders were mixed in 2:2:0 and 2:2:1 molar ratios to simulate the reaction between pure MgO diatoms and $WO_3$, and the influence of the silicon by-product from the MgO production on the final $MgWO_4$ diatoms. The MgO and Si were mixed in deionized water and subjected to a sodium hydroxide etch as described above. Tungstic acid was then added in 1:1 and 2:1 mole ratios of MgO to $WO_3$ and the batches was calcined at 1100°C for 1 hr in air.

Xray diffraction was performed on a Phillips PW-1800 powder diffractometer and analyzed using Phillips APD and X'Pert HighScore Plus software. Lattice parameter measurements were made using silicon as a standard. Typical scans were performed from 10 to 80° 2θ, with 0.15° step size. Shape preservation was characterized with the LEO 1530 scanning electron microscope in secondary electron mode and electron dispersive spectroscopy (EDS) for compositional information on the converted diatom structures. Quantitative analysis was performed using the Rietveld function built into the Panalytical High Score Plus software package.

Photoluminescence measurements were performed at room temperature using a 337 nm pulsed nitrogen laser. A Laser Physics LN1000 nitrogen laser, an Acton Research Spectra Pro 500i emission monochromator, and a Hammamatsu photo sensor module comprised the system. The laser was triggered externally with a Spiricon Chopper Sync II, allowing use of an EG&G 5208 2-phase lock-in amplifier. The samples measured were excited at 45° incidence, and the resulting emission was collected at normal incidence using a collimating lens coupled to an Acton Research fiber probe. Fluorescence was detected using 0.8 V photomultiplier tube with 1 mm slit width. Photography of $MgWO_4$ fluorescence was performed using a 254 nm UV light source from UVP, Inc. (Upland, CA).

## 3.3 Results and Discussion

### 3.3.1 XRD Phase Analysis

Heat treatment of $SiO_2$ diatoms with Mg vapor at 900°C for 1.5 hours yielded MgO diatoms with 28 wt % elemental Si by-product and less than 1% $Mg_2Si$. The Si content was predicted by calculation and confirmed by Rietveld analysis to be 16% (Figure 3.1b). Ultrasonication in deionized water with sodium hydroxide reduced the silicon phase content to 1% (Figure 3.1c). The sample calcined at 875°C for only 0.5 hr (Figure 3.1d) yielded a phase composition by the Rietveld method of 31 mole % $MgWO_4$, 56 mole % MgO, and 13 mole % $WO_3$, bearing a green color characteristic of $WO_3$. Quantitative analysis of the 100 % intensity peaks of MgO and $MgWO_4$ in Figure 1e showed a 1:1 molar ratio of the $MgWO_4$ and MgO phases in samples treated between 800° and 1100° C. When heated to 1250°C, some of the $MgWO_4$ was transformed to the high temperature "beta" phase of $MgWO_4$, shown in Figure 1f. The color of the samples changed from green to gray as tungsten oxide was converted into $MgWO_4$, and then to pink above 1000°C as an unidentified phase crystallized. The samples prepared at 1100° and 1250°C possessed a pink color and showed an unidentified phase in their diffraction patterns (no exact JCPDS match) however MgO and $MgWO_4$ maintained a 1:1 molar ratio.

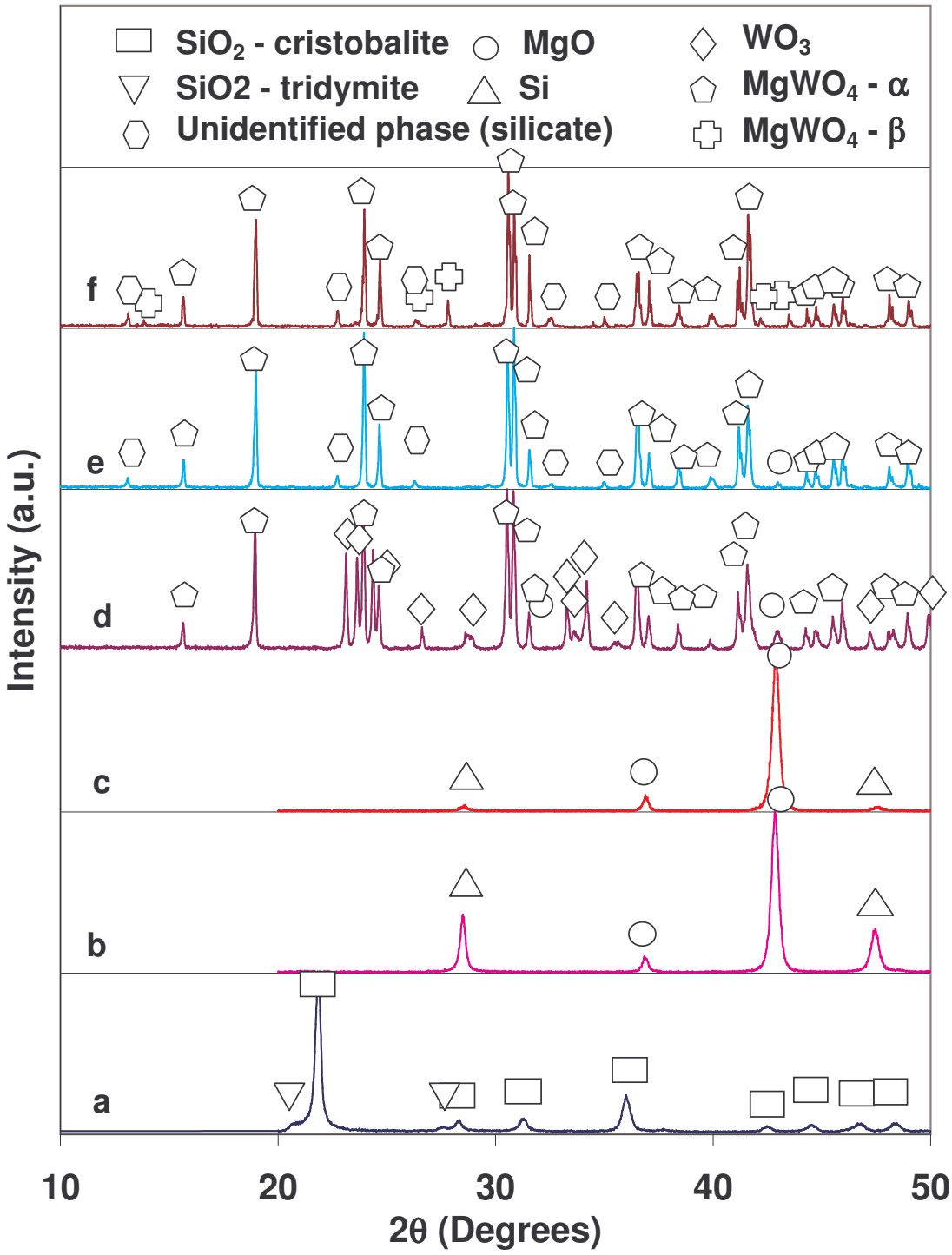


Figure 3.1. XRD of (a) $SiO_2$ diatoms (b) MgO + Si diatoms after reaction, 900°C for 1.5 hr, with 2.45:1 Mg:$SiO_2$ starting molar ratio (c) MgO diatoms after Si etching, 60°C, 3 hr, (d) Diatoms showing $MgWO_4$ + MgO + $WO_3$, 875°C, 0.5 hr (e) Diatoms showing $MgWO_4$ + MgO 1100, 1 hr, (f) Diatoms showing $MgWO_4$ + MgO 1250°C, 0.5 hr. All samples used 2:1 MgO:$WO_3$ molar ratio.

Wet mixing of MgO and APT resulted in a relatively amorphous powder tungstate powder, retaining significant crystalline MgO. After 2 hr at 500°C the sample, a green powder, crystallized as MgO and $WO_3$ with no $MgWO_4$ detected. Bludsuss referred to the "first peaks" of $MgWO_4$ forming after 2 hr at 500°C[75], and it is apparent that the calcination at 500°C is quite insignificant. After 2 hr at 800°C, MgO and $MgWO_4$ appeared in a 1:1 molar ratio. A third crystalline phase appeared in the sample heated to 1000°C that was not identified in the JCPDS file. The APT sample that was heated to 1000°C for 2 hr, became pale pink colored, and the ratio of $MgWO_4$ content to MgO remained 50-50, and an unidentified phase (suspected to be a silicate) had crystallized, similar to the tungstic acid samples.

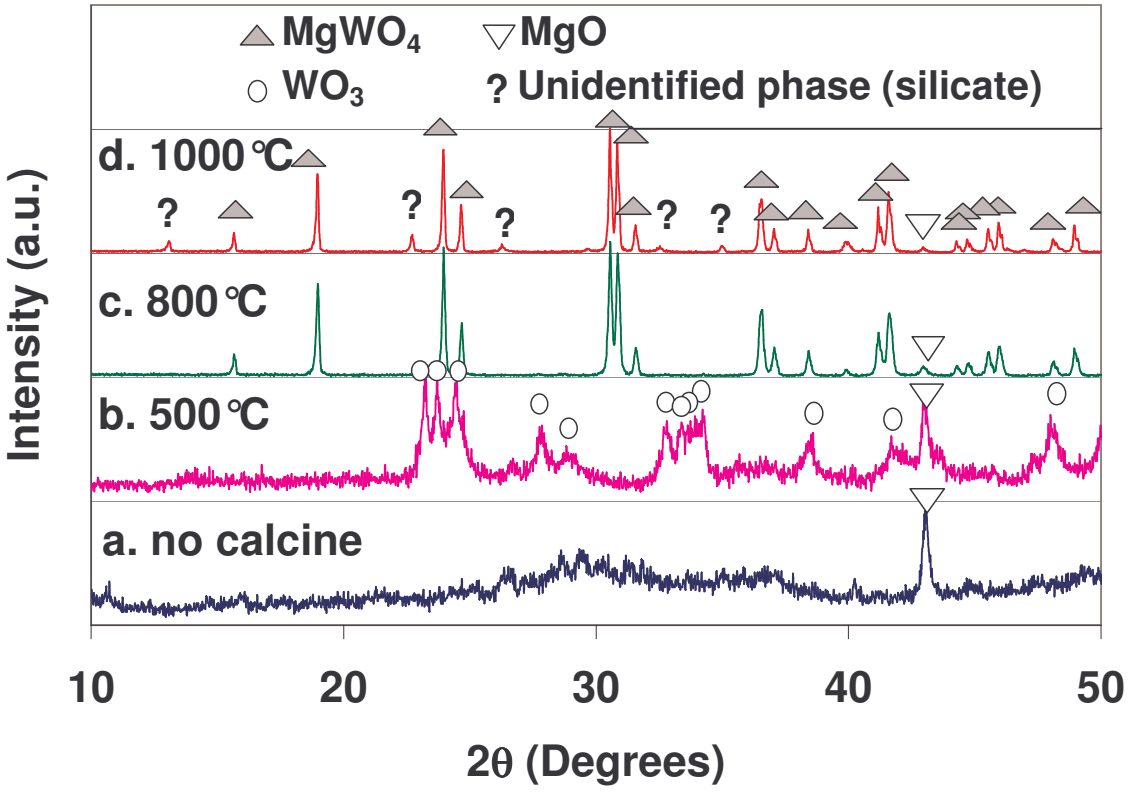


Figure 3.2. Xray Diffraction (a) MgO blended with APT in water at 50°C for 1 hr at room temperature, (b) MgO and APT, 500°C, 2 hr, (c) MgO and APT 800°C, 2hr, (d) MgO and APT 1000°C, 2 hr. All with 2:1 molar ratio of MgO:$WO_3$.

No distinct differences were seen between the tungstic acid and APT precursors in terms of initiating formation of $MgWO_4$ at lower temperatures. Both precursors simply appeared to decompose into tungsten oxide ($WO_3$) and then proceed to react with the MgO.

The conclusion by early researchers (using the Debye-Scherrerr method of XRD) that the excess MgO was incorporated into the $MgWO_4$ structure was proven false by analysis of the XRD patterns. In the diffraction patterns presented here, one can see that the intensity of the (200) peak of MgO pales in comparison to the intensity of the (110) of $MgWO_4$, even at a 1:1 molar ratio of the phases. However, given the relative intensity ratios (RIR) of MgO and $MgWO_4$ which are found in the JCPDS files, 1.0 for MgO and 3.7 for $MgWO_4$, the ratio of MgO to $MgWO_4$ in the sample could be determined. The difference in relative intensity of the two phases was due mainly to the greater mass absorption by the tungsten bearing phases. Lower concentrations of MgO would be increasingly difficult to identify due to the adsorption effects, making a qualitative look at phase content in the XRD patterns initially deceptive, as shown by early $MgWO_4$ work where researchers drew the incorrect conclusion that no MgO phase remained in samples with as much as 2:1 ratio of MgO to $MgWO_4$[73].

The crystalline phase of unknown composition that appeared in samples treated at 1000°C and above was profile fitted and was indexed to determine a hexagonal or rhombohedral unit cell. The cell was similar to a series of silicates with heavier cations of the type 48-1629[78]. A silicate phase could have originated from the residual silicon left by the sodium hydroxide etching process.

### 3.3.2 Fluorescence Analysis

The increased brilliance associated with the batching composition of 2 moles MgO per 1 mole $WO_3$ was observed in a control sample where MgO and $H_2WO_4$ powders were calcined in alumina crucibles at 1100°C for 1 hour in both 1:1 and 2:1 molar ratios. Figure 3.3 shows the powders in ambient lighting and again when illuminated with a 254 nm UV mercury lamp. The 2:1 molar ratio powder (on the right) was observed to fluoresce much more brightly than the 1:1, single phase $MgWO_4$, as described by the literature[73].

Fluorescence measurements in Figure 3.4 show the maximum fluorescence of $MgWO_4$ produced from diatom frustules ranges from 650 to 700 nm (orange-red). The color of the powder was unrelated to the red fluorescence, as the gray 800° and pink 1000°C APT samples fluoresced at the same wavelength. The pink color of the powder seemed to be correlated to the crystallization of the unidentified (possibly silicate) phase, and the presence of the silicate did not appear to impact fluorescence. A slight shift to higher wavelength was observed in the 1000°C sample, and it was observed to be much more brilliant than the 800°C sample.

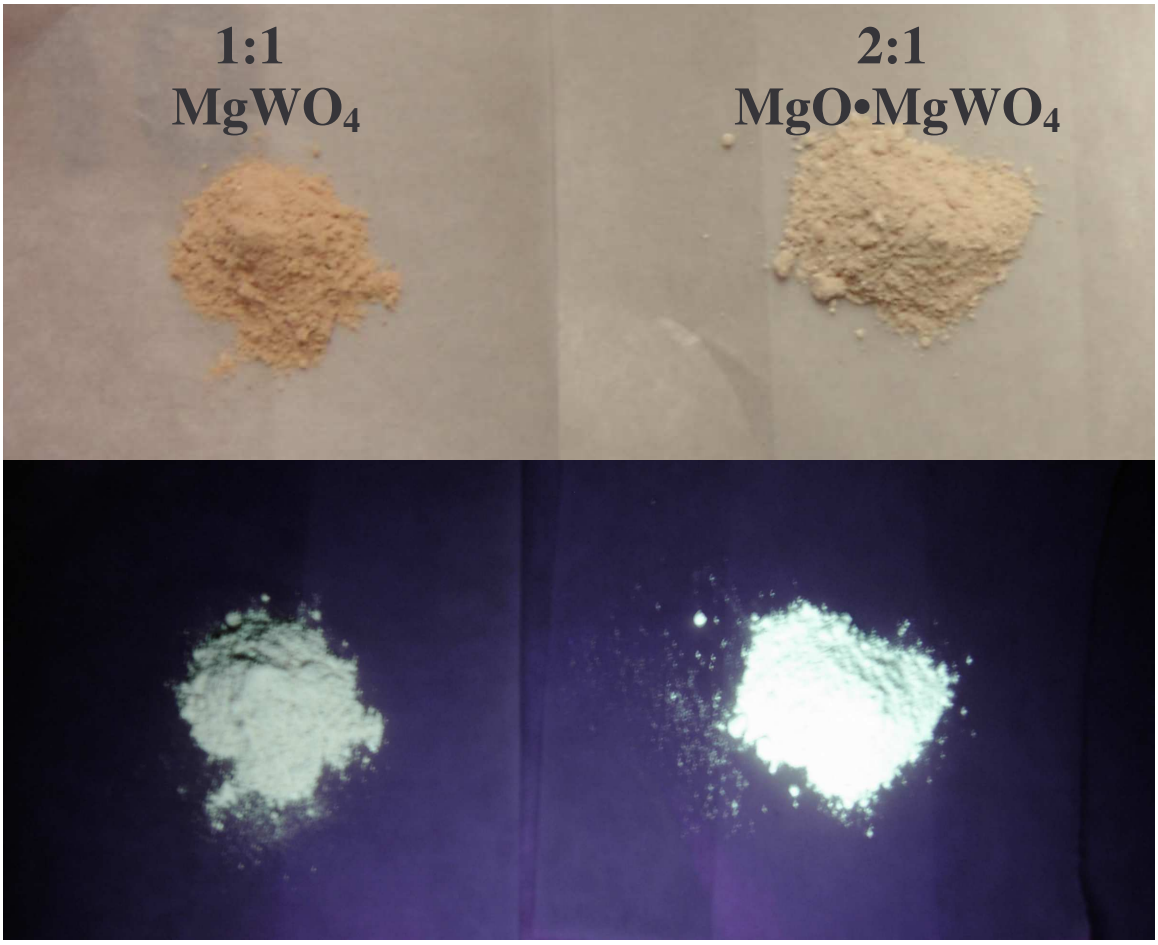


Figure 3.3. $MgWO_4$ prepared from MgO (Alfa Aesar) and tungstic acid ($H_2WO_4$ Alfa Aesar) using 1:1 and 2:1 molar ratios of MgO to $WO_3$. The top level images show the powders side-by-side in natural light. The lower images show the fluorescence of the same powders when excited with 254 nm ultraviolet light. The powder prepared using 2:1 ratio of MgO to $WO_3$ shows notably more brilliant fluorescence.

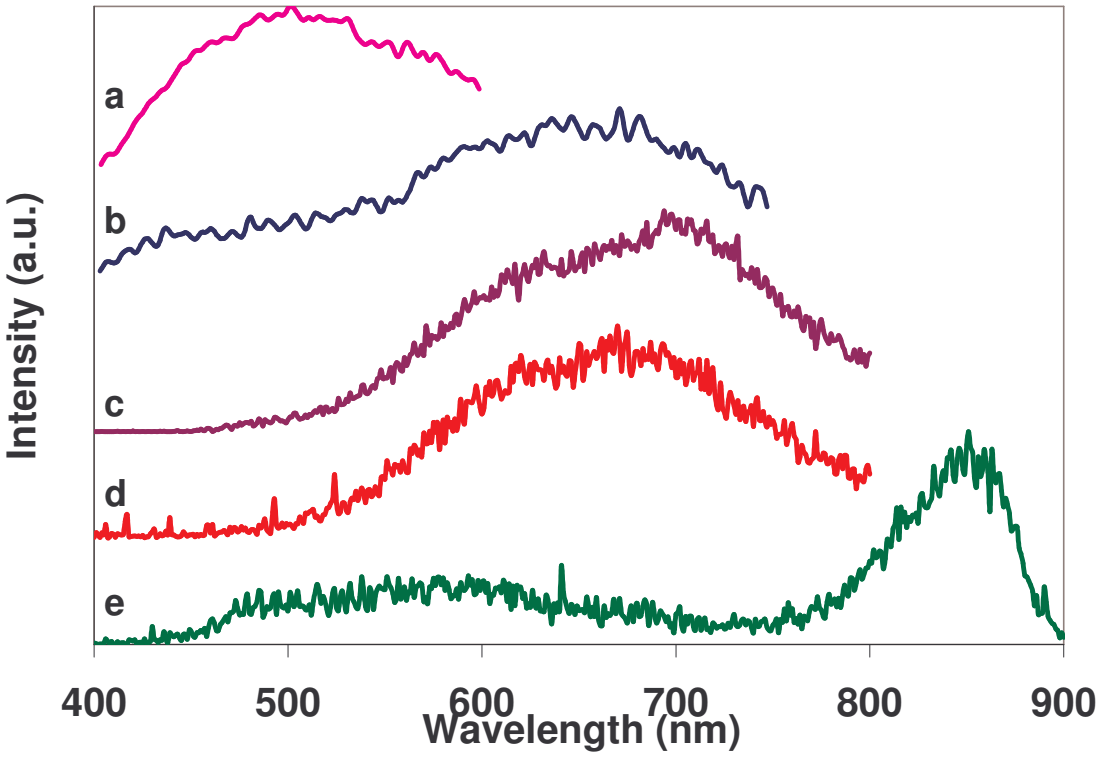


Figure 3.4. Fluorescence spectra of $MgWO_4$ from (a) Alfa Aesar, (b) diatom MgO and tungstic acid, 1100° C, 1 hr, (c) diatom MgO and APT, 800° C, 2 hr, (d) diatom MgO and APT, 1000° C, 2 hr, (e) control sample of Alfa Aesar MgO, tungstic acid and Si (etched with NaOH and filtered) 1100°C, 1 hr.

The fluorescence of diatom-based $MgWO_4$ samples was compared with that of $MgWO_4$ from Alfa Aesar. The commercial sample did not fluoresce as brightly as the diatom material, but gave its intensity peak near 500 nm, as expected for pure $MgWO_4$. The control sample composed of magnesium oxide, tungsten oxide and NaOH-etched silicon metal produced a material possessing distinguishable white and reddish colored phases, similar to the diatom material, gave a green fluorescence similar to pure $MgWO_4$ (Figure 3.what what). A large emission was detected in the near infrared range for the control sample. The result of the control experiment suggested that while the residual silicon affected the color of the $MgWO_4$ via the crystallized silicate, the shift in the fluorescence peak in $MgWO_4$ was not attributable to the silicon. The fluorescence shift appeared to be associated with impurities from the starting diatoms incorporated into the $MgWO_4$ lattice, which may include Al, Na, or Ca. It was not made clear whether the red-orange fluorescence of the diatom $MgWO_4$ was a result of a shift of the green fluorescence to longer wavelength; of the infrared fluorescence to a shorter wavelength; or perhaps both.

### 3.3.3 SEM Analysis and Shape Preservation

The 2-to-1 molar ratio which yielded improved fluorescent efficiency also potentially presented an advantage for retaining frustule shape during the calcination process. This argument was made by considering the volume changes associated with the conversion reaction steps. In the conversion of the $SiO_2$ molecule to two of the densely packed MgO molecules (37.34 cc/2-mole MgO), a volume decrease of 13.2% is anticipated for each $SiO_2$. On the addition of $WO_3$ species to produce $MgWO_4$ (65.56

cc/mole), a volume increase of 351% is predicted. In a 2:1 MgO:$WO_3$ composition, the predicted volume increase would be only 176%. That the amount of $WO_3$ required to achieve significant fluorescence is half that required to produce phase pure $MgWO_4$ suggests that the possibility for shape preservation could also be improved by minimizing intrusion on the starting MgO structure. Figure 3.5 shows the first steps toward producing $MgWO_4$ frustules – the progression from silica to MgO.

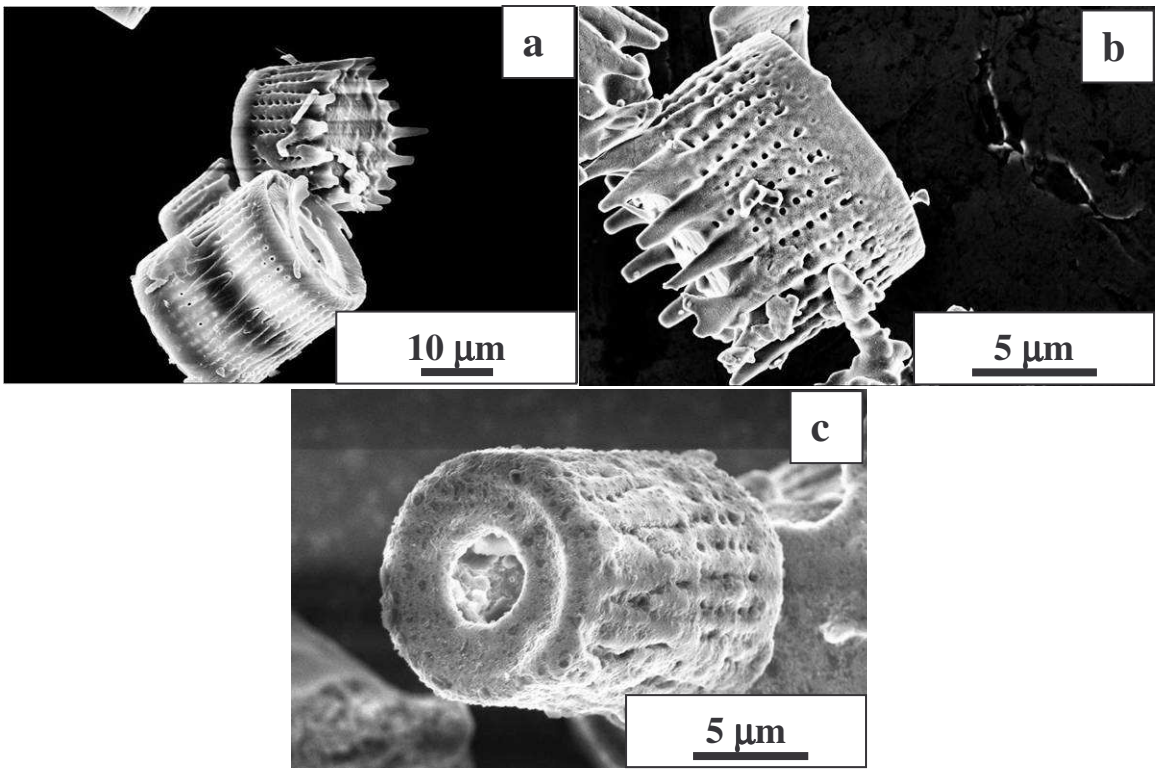


Figure 3.5. SEM of diatoms (a) as natural $SiO_2$, flame polished by manufacturer, (b) converted to MgO with Si byproduct converted at 900°C in 1.5 hour with 2.45:1 mole ratio of Mg:$SiO_2$, (c) and MgO with the Si removed using aqueous NaOH etching process, 60°C, 3 hr in ultrasonic bath. EDS of (b) and (c) shown in Chapter 2, Figure 2.4.

SEM results of shape preservation show a progression of morphologies of $MgWO_4$ as temperature increases (Figure 3.6). In general, the frustule morphology was preserved on the microscale, as the cylindrical aspect of the frustules was maintained, and in some cases the primary pore remained, but the finer "nano-scaled" features disappeared. The $MgWO_4$ grains grew large, averaging 1 micron or larger. Powders calcined at higher temperatures (1100°C in Figure 3.6b) exhibited the most dramatic grain growth and the least shape retention. The 10 mole % $WO_3$ sample, which was calcined at 900°C for 2 hours showed a finer grain structure of $MgWO_4$, which coated the MgO frustule. The lower tungsten content also produced the best shape preservation. Several of these frustules retained their appearance and even some of the fine pores remained discernable. Frustules that were produced by reaction of APT with MgO also showed similar shape retention as that seen in tungstic acid sample (Figure 3.7). In the 800°C APT sample, grain sizes were smaller than at 1000°C, but much of the overall shape of the frustule was lost. The wet mixing step in the APT/MgO processing may have been a contributing factor for shape degradation in the frustules. Figure 3.6d shows an MgO frustule (silicon previously removed by NaOH etching) which was calcined at 1100°C for 2 hours to show that the coarsening of $MgWO_4$ was not due to MgO coarsening alone.

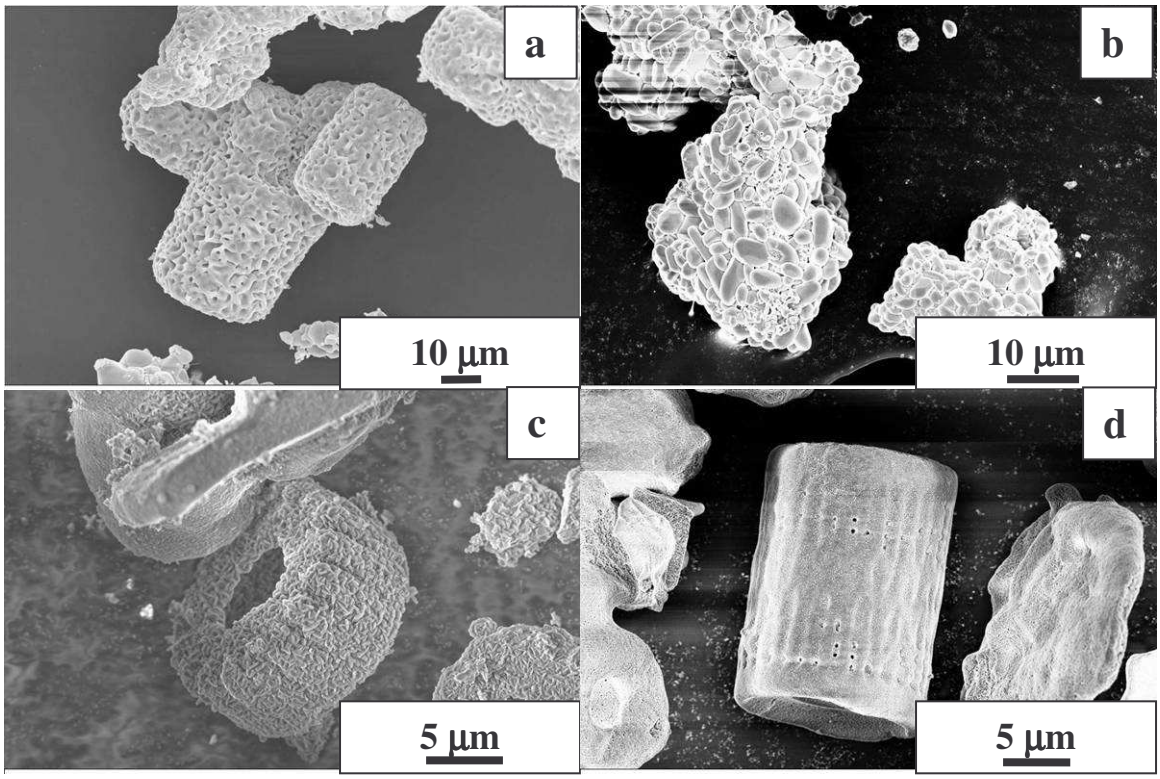


Figure 3.6 $MgWO_4$ made by dry mixing diatom MgO with tungstic acid and calcining at (a) 900°C, 2 hr (50% $MgWO_4$), (b) 1100°C, 2hr (50% $MgWO_4$), (c) 800°C, 2 hr (10% $MgWO_4$), (d) MgO control with no tungsten, 1100°C, 2 hr.

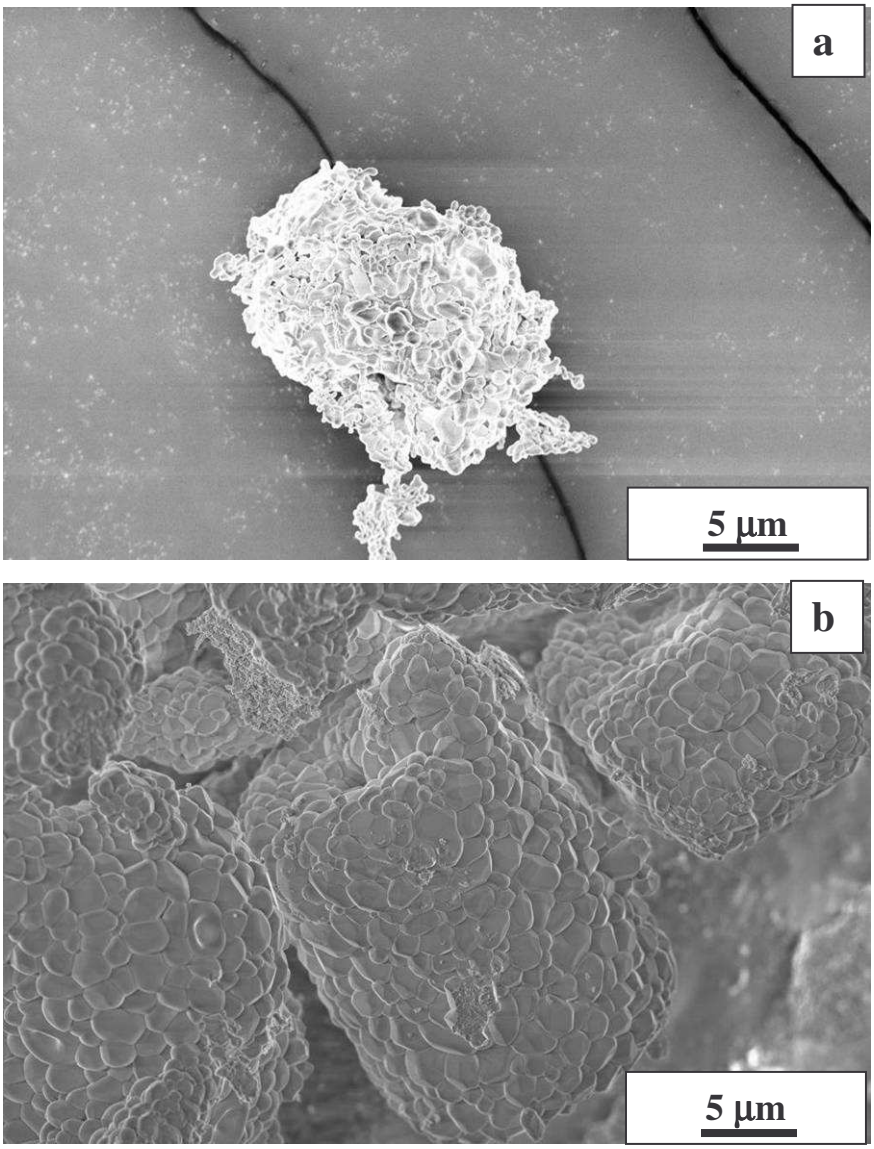


Figure 3.7 SEM of MgWO4 diatoms produced with 2:1 molar ratio of MgO to $WO_3$ (APT) via wet mixing at room temperature followed by calcination at (a) 800°C, 2 hr, (b) 1000°C, 2 hr.

## 3.4 Conclusion

In summary, shape preserving reactions have been performed to convert $SiO_2$ diatom frustules to $MgWO_4$ in the range of 800° to 1250° C. XRD patterns of the products were indexed as wolframite $MgWO_4$ and MgO at 800°C; wolframite $MgWO_4$, MgO and a silicate phase at 1000° to 1100°C; wolframite $MgWO_4$, MgO, the silicate and the high temperature β-$MgWO_4$ at 1250°C. The $MgWO_4$ phase produced from natural $SiO_2$ diatoms fluoresced brilliantly from 600 to 700 nm when excited with 337 nm light. The fine features of the diatom frustules were not preserved in the conversion of MgO to $MgWO_4$, however cylindrical $MgWO_4$ particles of uniform shape and size were produced. The significance of this work beyond fluorescence was the demonstration of binary ceramic systems that can be produced from biological templates by displacement and additive reaction synthesis. Although this work has focused on the conversion of bio-derived silica which bears certain impurities inherent to the environments in which they are produced (and potentially influence the properties of the product material), these techniques could be applied to other silica structures produced by biological or synthetic means to easily yield large numbers of controlled micro-shapes with functional compositions in a massively parallel processing scheme.

# CHAPTER 4

# SHAPE PRESERVING PREPARATION OF $CaCrO_4$, $CaMoO_4$, $CaWO_4$, FROM SAND DOLLAR AND COCCOLITHOPHORID CALCITE

## 4.1 Introduction

Previous work reported by Sandhage, *et. al.,* describes the shape preserving conversion of silica structures into new materials (MgO, $TiO_2$). These reactions took place via chemical displacement reactions where metal vapors or metal halide vapors reacted with the silica structures to yield new compositions while maintaining the shape of the original silica structure[10, 43, 60]. This paradigm of 3D microfabrication entailed using biologically-formed (bioclastic) inorganic structures as templates for producing identical structures with selected material compositions. In this new work, bioclastic calcium carbonate structures were converted into materials with different functionalities using solution based inorganic chemistry. Calcium carbonate structures are produced by a wide array of organisms from common mollusks, such as coral, starfish, and sand dollars, to single-celled algae known as coccolithophorids. Structures from the micro- to meso-scale are thus available.

Bioclastic calcium carbonate can take one of two crystal forms, calcite or aragonite, depending on the organism, water pressure, temperature and pH conditions under which the structures are formed. The structures evaluated in this study were of the calcite phase.

Sand dollars, mollusks related to sea urchins, form highly porous calcite shells called “tests”. Certain recognizable features of the test microstructure, and the spines that grow from the tests, were identified to demonstrate shape preservation over a wide range

of length scales, microns to centimeters (Figure 4.1). Coccolithophores provided shapes on the sub-micron scale. Extensive research on the biological processes of coccolithophores and other aquatic carbonate forming organisms is of primary interest in atmospheric, oceanic and geological sciences. Despite only a few hundred species (compared with over 100,000 diatom species), coccolithophores are widespread in the Earth's aquatic and marine systems. They serve as the primary global agent for the removal of carbon from the carbon-cycle and are the major contributors to limestone and gypsum deposits worldwide[79-82].

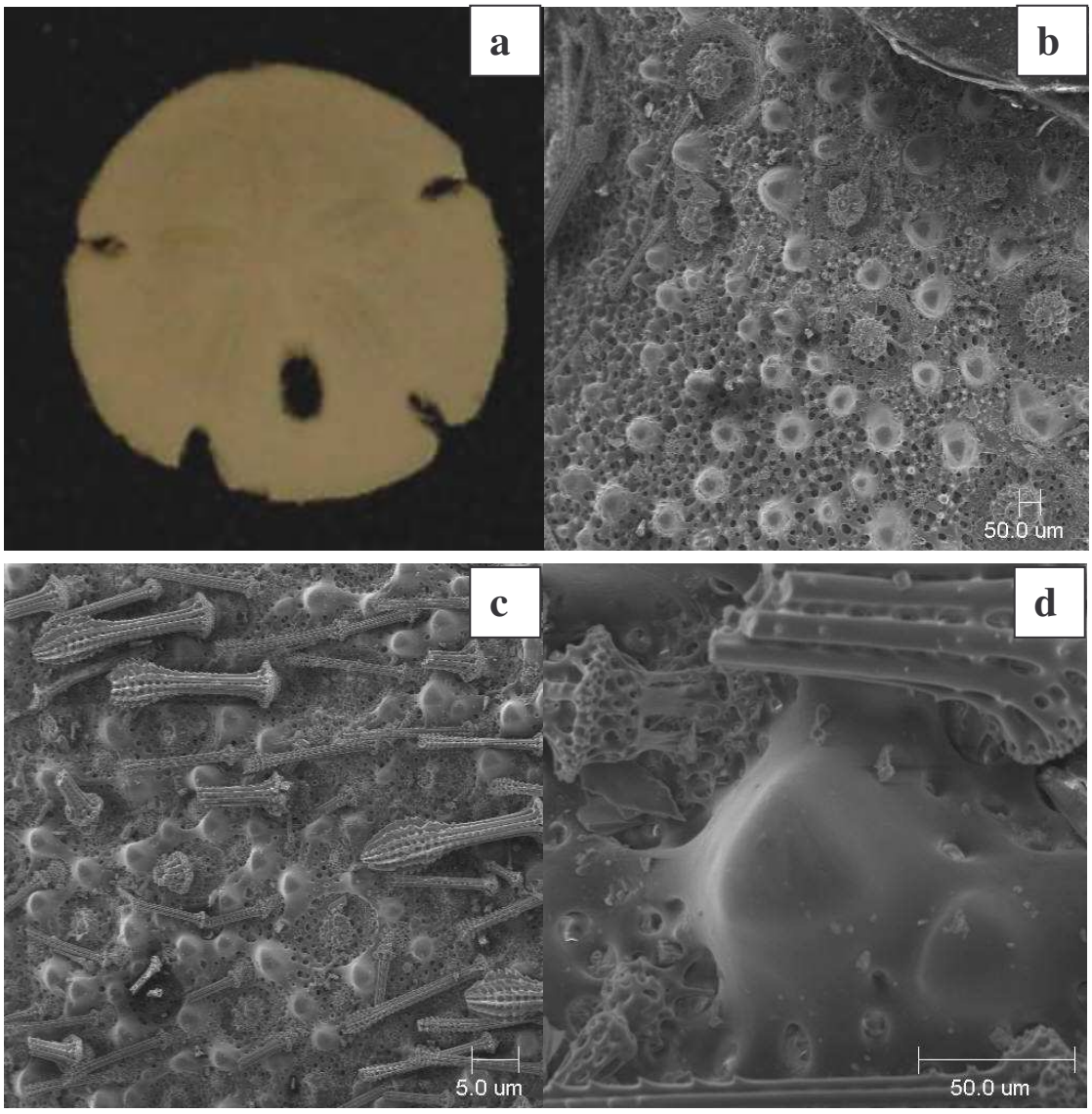


Figure 4.1. SEM of unreacted sand dollar (a) whole sanddollar, top view, (b) SEM of underside features, (c) SEM of topside features and locomotive appendages, (d) SEM of lens-like structure on top surface.

Rather than possessing a single (or dual) capsule-like structure as seen with the diatoms, the coccolithophore cell is covered with smaller scale-like structures called "liths". Certain types of coccolithophores called the "holococcoliths" arrange the liths in periodic arrays that are remarkably similar to synthetically produced photonic crystals. The species of coccolithophore used for this study is *Emiliania huxleyi*, perhaps the most commonly researched species, which produced ovular liths with regular features seen in Figure 4.2.

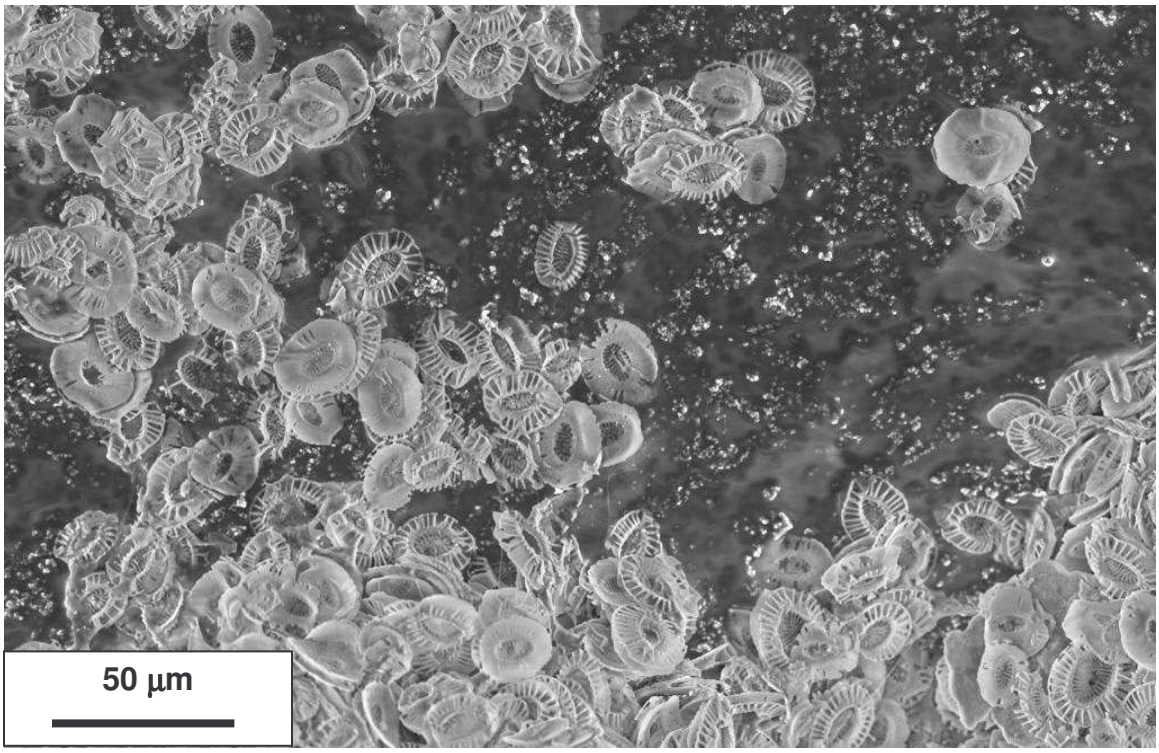


Figure 4.2. Calcium carbonate coccoliths from *Emiliana huxleyi.*

In particular, the conversions of calcium carbonate to calcium tungstate ($CaWO_4$), calcium molybdate ($CaMoO_4$), and calcium chromate ($CaCrO_4$) were investigated. These materials were chosen for the reported ease of producing II-VIB compounds at low temperatures. Bludssus, et al., report in their patent that pure compounds of the general

composition Me(II)$WO_4$ can be produced, in some cases at relatively low temperatures, by reacting the hydroxides or oxides of Group II elements with ammonium para-tungstate or ammonium meta-tungstate. They provide example of calcium hydroxide reacting with ammonium para-tungstate after mixing for 30 minutes from 45-55°C followed by drying at 100°C. X-ray diffraction found the material was fully reacted, yielding phase-pure calcium tungstate[75]. We sought to emulate this procedure with bioclastic calcium carbonate in order to produce shape specific structures of the formula Ca[Me]$O_4$.

The current work expands on Bludssus' work by using this reaction to achieve shape preserved structures from calcium carbonate. In addition, we explored the feasibility of the corresponding reactions of calcium carbonate with ammonium para-molybdate and ammonium di-chromate, which was not reported in prior work. This work also demonstrates an attempt at the conversion of a macro-scale biomineral structure (the sand dollar) into a new material.

Calcium tungstate and calcium molybdate are common fluorescent materials that have been used in lighting and display applications for many years[83]. Calcium tungstate is also an interesting material for ceramic matrix composites and shape controlled processing of calcium tungstate could lead to higher toughness composites materials. Calcium chromate is used as a yellow pigment, a depolarizer for batteries and as a corrosion inhibitor. Whether these applications are consistent with shape-preserved applications, calcium chromate is presented for demonstration of the versatility of shape preserving conversion chemistry. Significant effort was avoided on the chromate do to lack of applications coupled with the severe health risk as a carcinogen and irritant that

can cause such maladies as erosion of the nasal septum upon inhalation. Instead we focus primarily on conversion of structures to $CaMoO_4$ and $CaWO_4$.

## 4.2 Experimental Materials and Procedure

Sand dollar tests of the genus *Mellita* were obtained from The Shell Factory (Fort Myers, FL). X-ray diffraction (Figure 4.3a) shows single phase of calcite ($CaCO_3$) or magnesian calcite $(Ca,Mg)CO_3$. EDS detected magnesium in the tests (Figure 4.3b) indicating the composition is likely that of magnesian calcite. Coccoliths of the species *Emiliania huxleyi* were obtained from cultures at Scripps Oceanographic Institute at University of California, San Diego. Ammonium para-tungstate (APT) $(NH_4)_{10}W_{12}O_{41}\cdot 5H_2O$, ammonium para-molybdate (AMT) $(NH_4)_6Mo_7O_{24}\cdot 4H_2O$ and ammonium di-chromate (ADC) $(NH_4)_2Cr_2O_7$ were obtained from Alfa Aesar as powders. The AMT powders were made into 0.25 and 0.5 Molar solutions (relative to $MoO_3$) in deionized water. The APT was less soluble in deionized water, but could be kept in solution of 0.1 Molar concentrations with respect to $WO_3$ at 80°C. The ADC was prepared as a 1.0 Molar solution in deionized water.

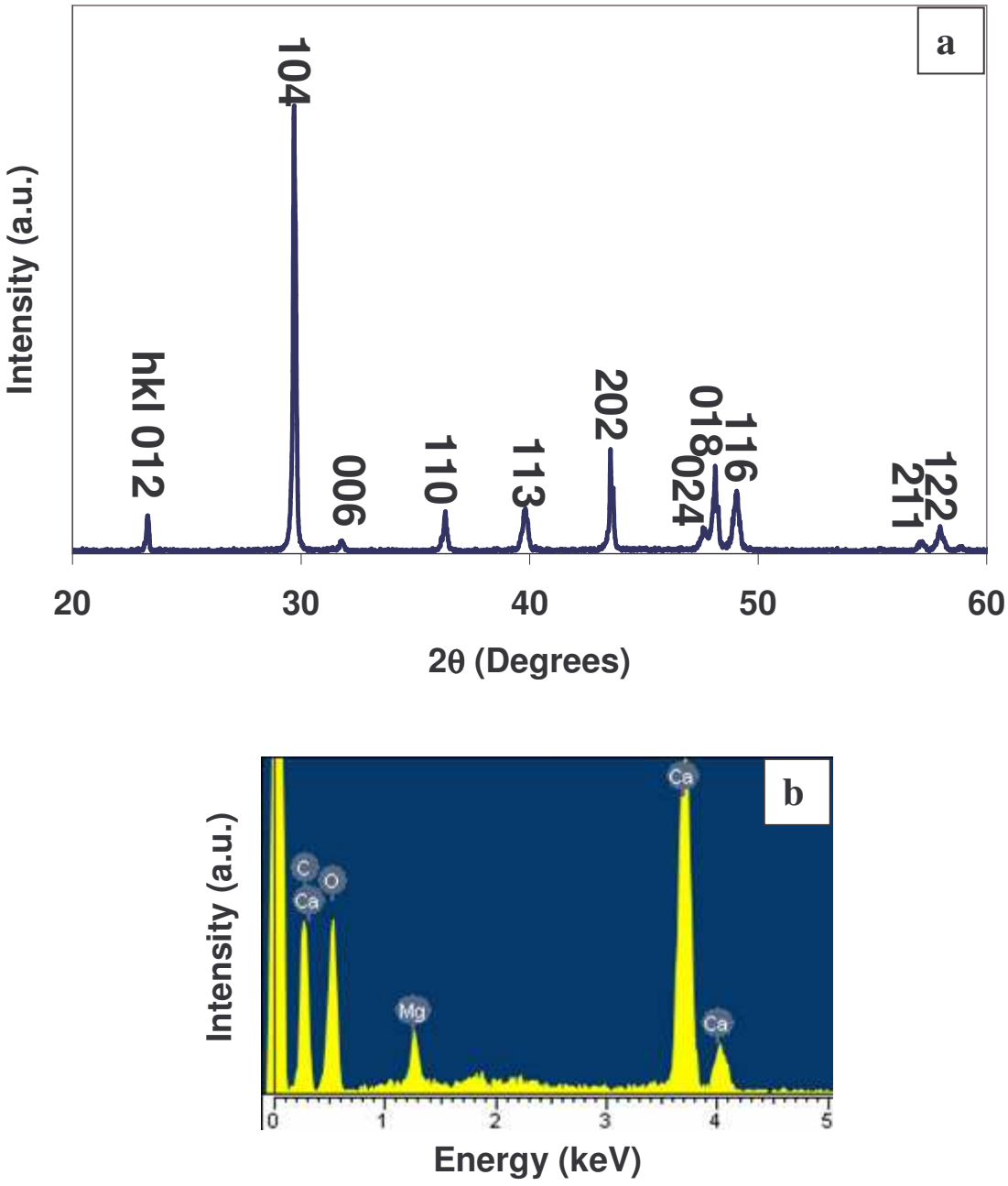


Figure 4.3 (a) XRD of sanddollar showing (Ca,Mg)$CO_3$/calcite (PDF 43-697) and (b) EDS showing Ca and Mg content of the sanddollar structure.

Sand dollars or coccoliths were immersed in solutions of known concentration of ammonium para-tungstate (0.1 Molar), ammonium para-molybdate (0.25 and 0.5 Molar), or ammonium dichromate (1.0 Molar). The immersion was done at temperatures from 20 to 100°C. The quantity of solution used corresponded to the amount of reactant needed to totally convert the carbonate structure. Drying was performed in ambient air between room temperature and 100°C for 8 hours. Calcium chromate samples were given additional treatment from 500 to 750°C in flowing, ultra high purity carbon dioxide to delay calcination. Calcination was purposely avoided to promote reaction of calcium carbonate with ADC which could perhaps avoid crumbling of the test due to the volume contraction and re-expansion from $CaCO_3$ to CaO to $CaCrO_4$.

X-ray diffraction was performed using zero-background holders and PW-1800 x-ray diffractometer (Panalytical). Step sizes of 0.02° 2θ were used. SEM and EDS were performed on a Hitachi S-800 and LEO 1530 (FEG) microscopes.

## 4.3 Results and Discussion

XRD and EDS of sand dollar shells (called 'tests') revealed the structure to be that of calcite but with a significant inclusion of magnesium in the calcite (Figure 4.3). Sand dollar tests (shells) and spines were converted to calcium tungstate and calcium molybdate at temperatures below 100°C (Figure 4.4a and 4.4b). Ammonium dichromate did not react with the calcium carbonate in solution at 100°C. Interaction was only achieved after calcination at 700°C (Figure 4.4c). Even after a second soak/calcine cycle, the chromate sand dollar still bore $CaCO_3$ and CaO phases (Figure 4.5).

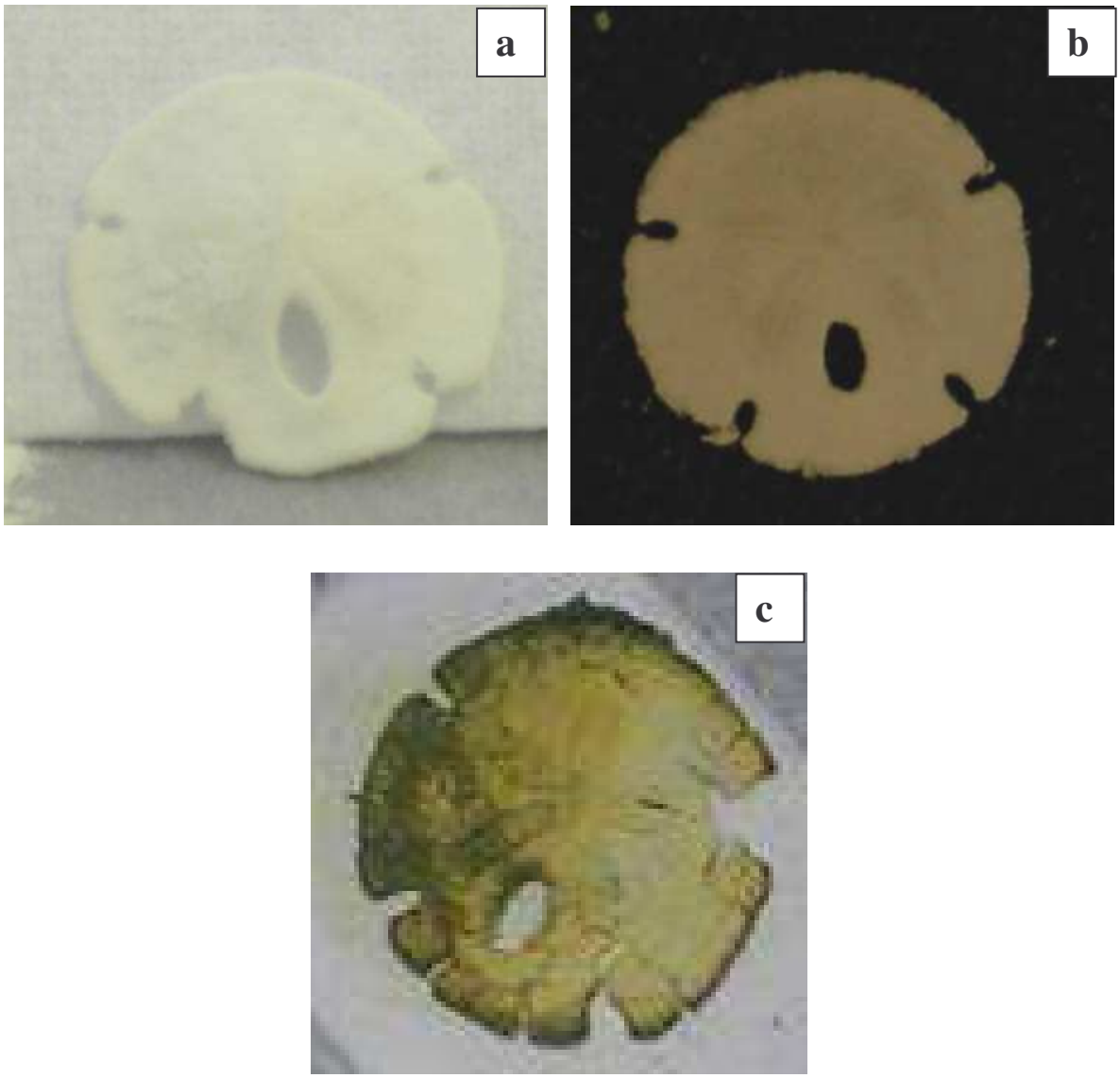


Figure 4.4. Optical images of sand dollar tests converted to (a) $CaWO_4$, (b) $CaMoO_4$, and (c) $CaCrO_4$.

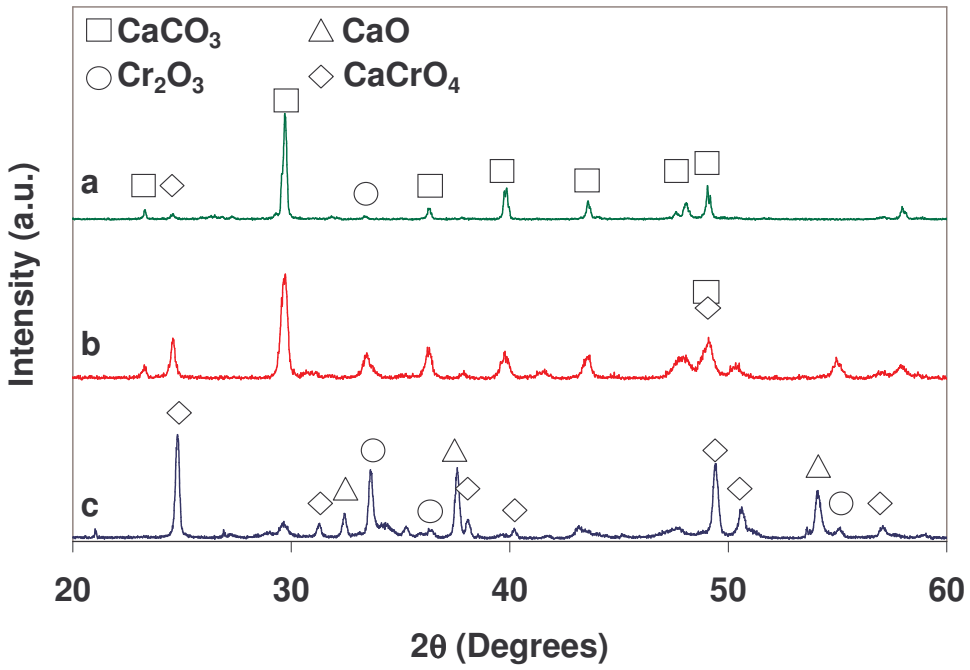


Figure 4.5 XRD pattern of calcium chromate sanddollar after (a) 1 cycle of ADC soak and 500°C, 2 hour calcine in $CO_2$, (b) 1 cycle of ADC soak and 700°C, 2 hour calcine, (c) 2 cycles of ADC soak and 700°C, 2 hour calcine The $Cr_2O_3$ peak increased from b to c as a result of excess chromium from the second soak.

Ammonium molybdate displayed good solubility in deionized water from room temperature to 100°C with as high a 0.5 molar concentration. XRD study showed that while the surface of the sand dollar bore only $CaMoO_4$, the bulk of the shell was unconverted (Figure 4.6). Completion of conversion of the sand dollars was considered when $CO_2$ bubbling from the surface of the shells ceased, after 5 hours at 50°C or 2 hours at 80°C, although in fact the entire structure was not converted. Further reaction may have been impeded by the coating of $CaMoO_4$. SEM showed that the structure of the sand dollar was preserved, but that nodules of $CaMoO_4$ formed on the surface of the sand dollars. With extended reaction time, the nodules covered the surface of the sand dollar, obscuring the features of the underlying structure (Figure 4.7).

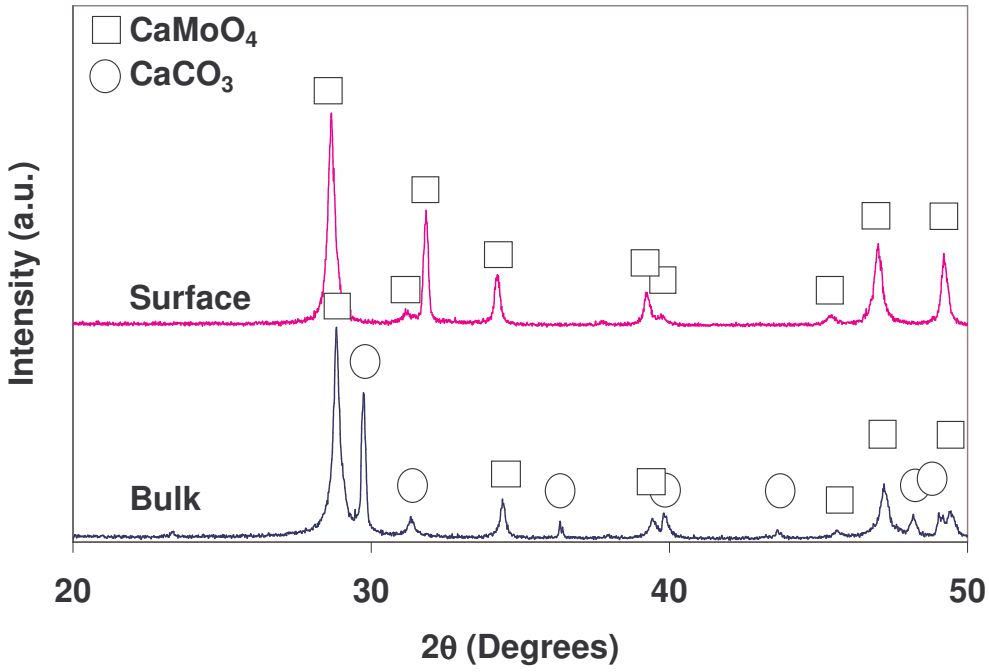


Figure 4.6. XRD of $CaMoO_4$ sanddollar surface and bulk after conversion at 80°C for 3.5 hours with 0.5 M APM.

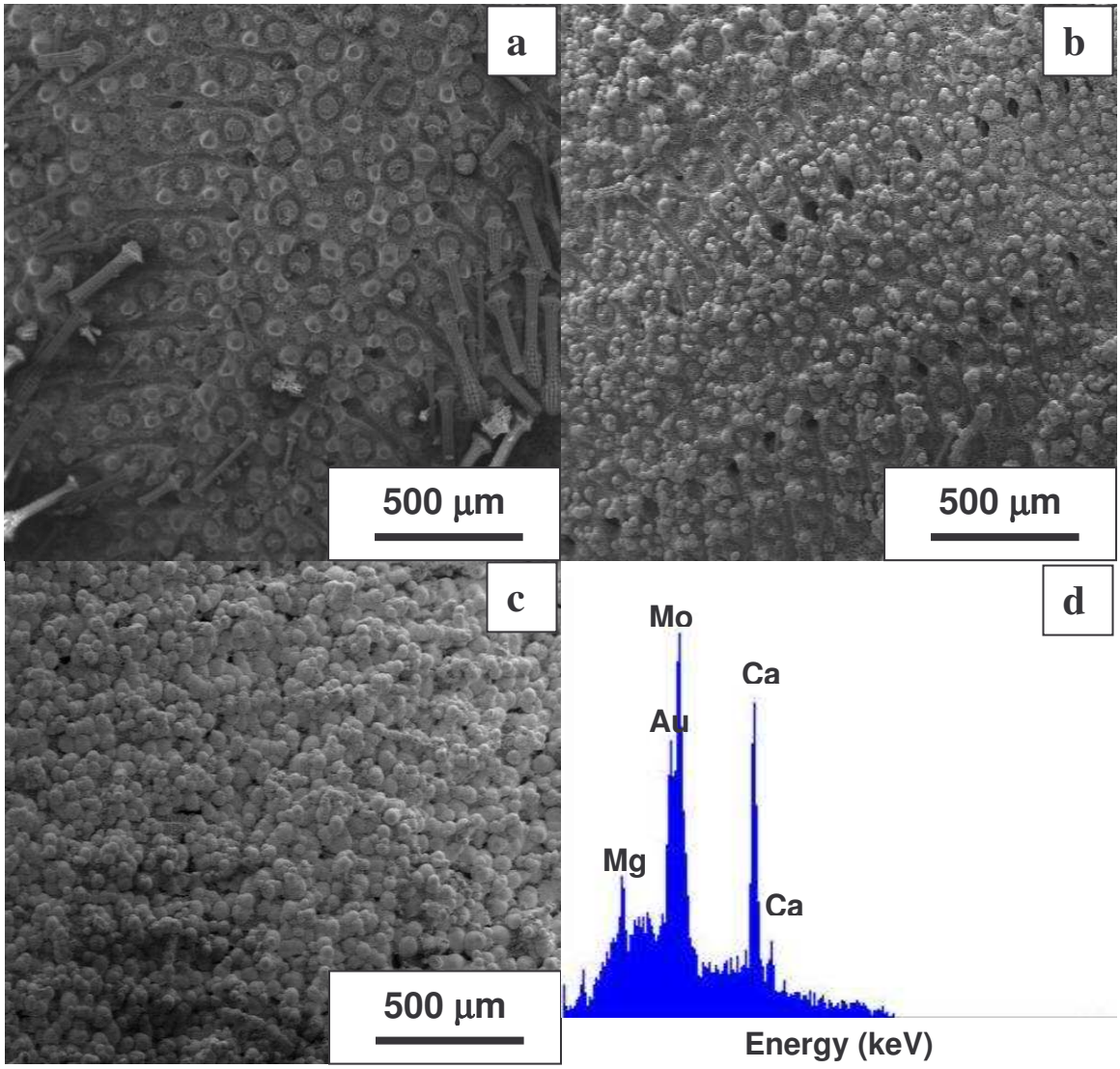


Figure 4.7. SEM of sanddollar surface before and after conversion to $CaMoO_4$ (a) before reaction (b) after 3.5 hr in 0.25 M APM solution at 80°C, (c) 5 hr in 0.5 M APM solution at 80°C, (d) EDS of 3.5 hour sample surface.

Ammonium tungstate displayed moderate solubility in deionized water above 80°C (less than 0.1 molar concentration). Solutions of ammonium tungstate were diluted with deionized water to help maintain solubility. These reactions were performed between 80 and 100°C. Similar to the $CaMoO_4$ case, the $CaWO_4$ sand dollars exhibited a coating-like structure where the surface showed phase pure tungstate, while the bulk of sand dollar showed primarily carbonate (Figure 4.8). Backscatter electron imaging of a converted sand dollar cross section showed the depth of the tungstate layer to be between 20 to 50 μm.

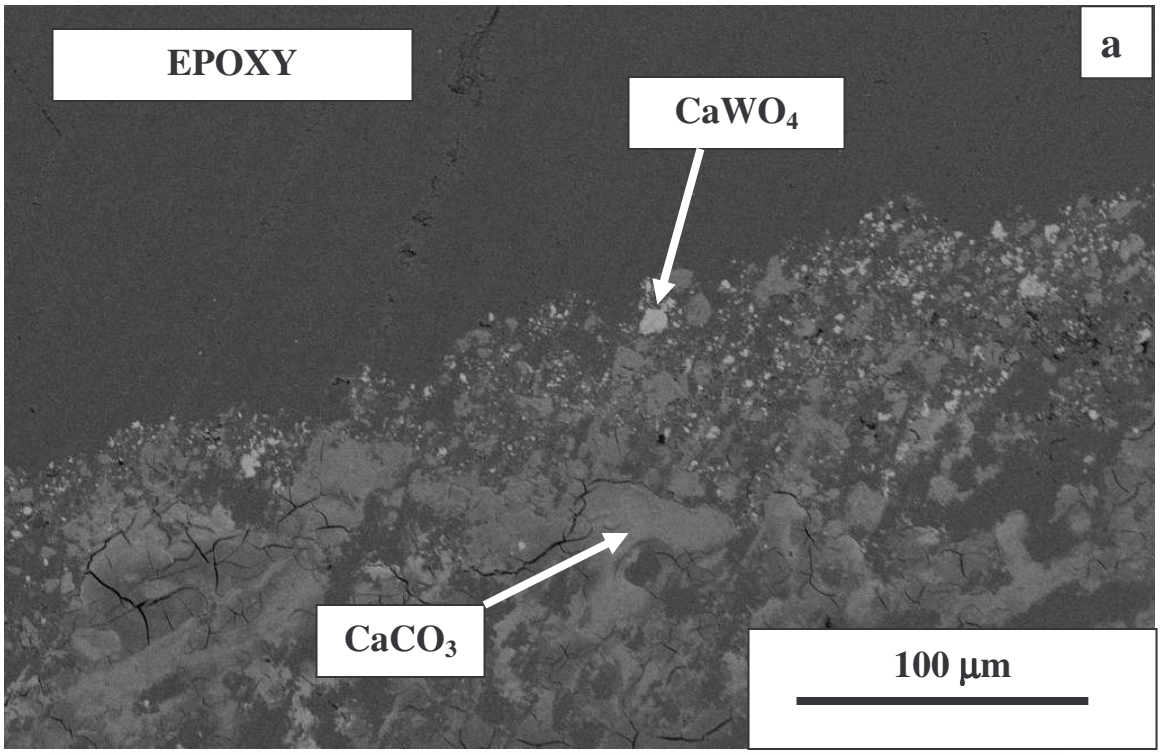


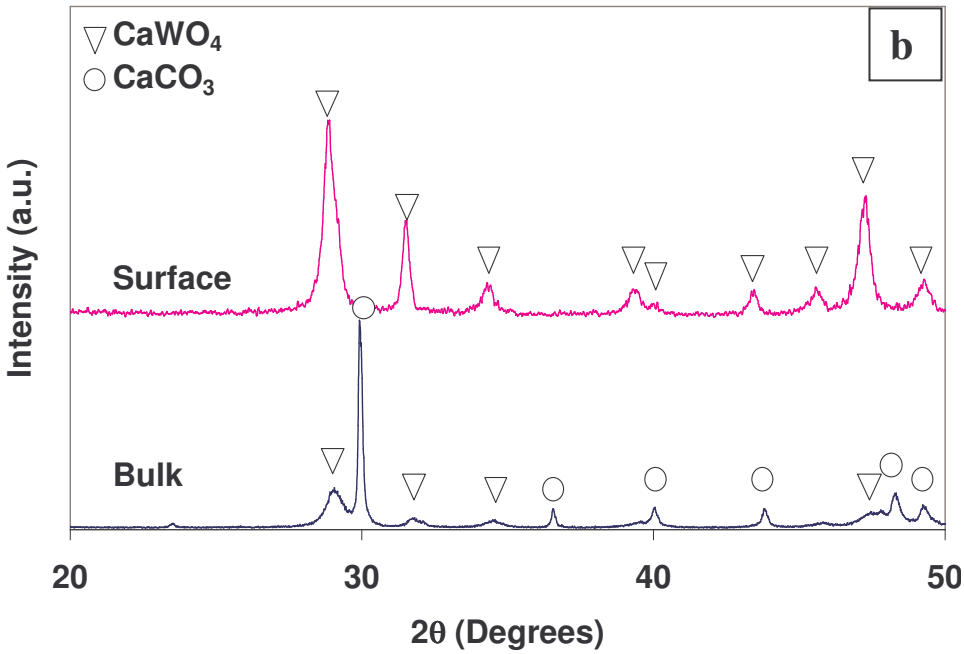


Figure 4.8 (a) Backscatter electron image of a $CaWO_4$ sand-dollar cross-section. The tungstate appears as the bright phase, which shows a depth of 20 to 40 µm. (b) XRD of $CaWO_4$ sanddollar surface and bulk after conversion at 80°C for 5 hours, showing coating-like conversion.

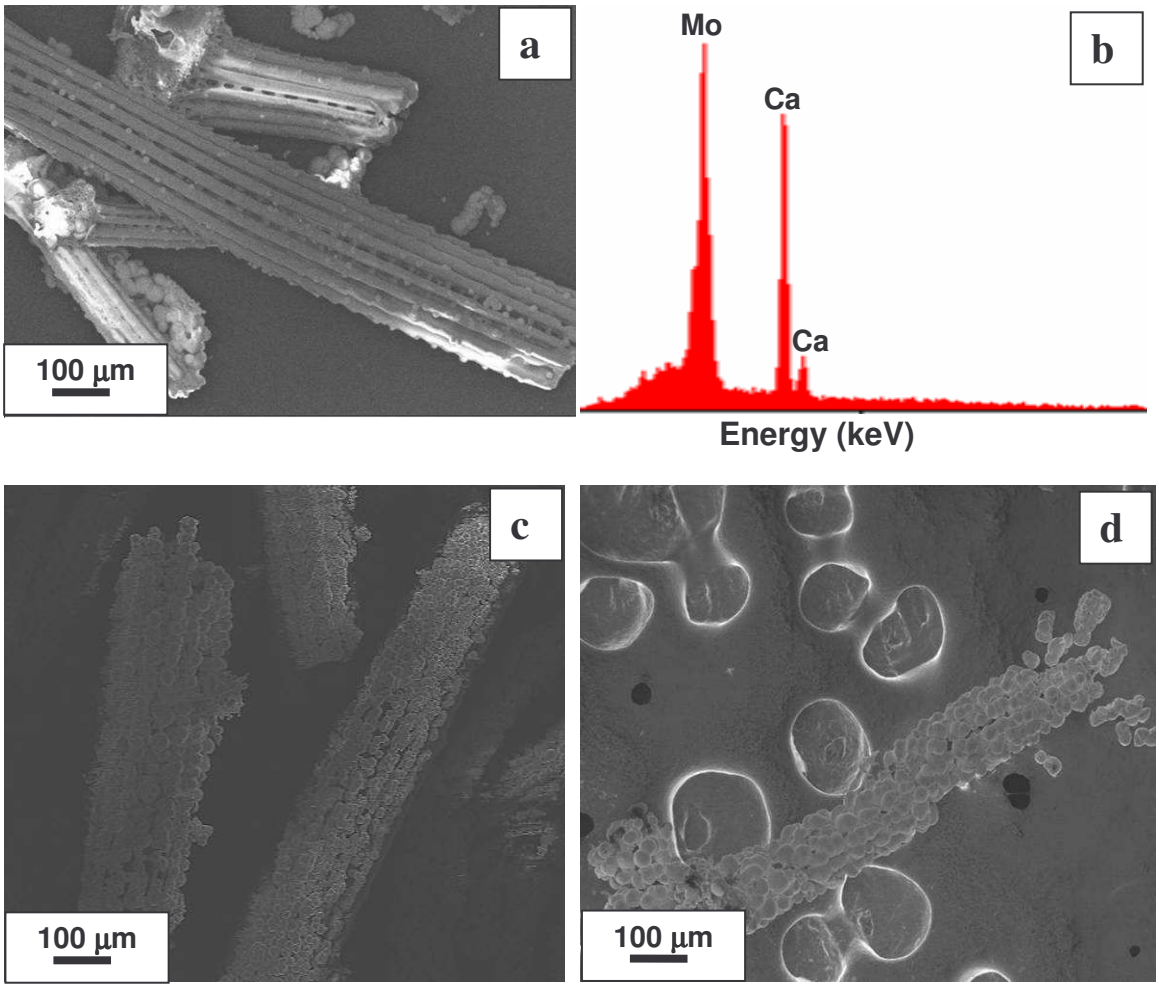


Figure 4.9 (a) SEM of unconverted sanddollar spines (not cross sections), (b) EDS of spine converted to $CaMoO_4$ in 10 min. at 80°C in 0.25 M APM, taken from the center of the spine, (c) SEM of $CaMoO_4$ spines after 10 min., (d) SEM of spines after 30 minutes.

The sand dollar possesses smaller club or rod shaped structures known as spines or 'tube feet' used for locomotion and food entrapment. These structures were used to determine the effect of reaction time on microstructures. Figure 4.9 shows a sequence of reaction times for converting the spines, with 20μm wide ridges, into $CaMoO_4$. After only 10 minutes in 0.25 molar APM at 80°C, the structure had converted to the molybdate and the shape of the ridges could be identified as ridges composed of 20μm spherical nodules. After 30 minutes, the nodules coarsened further leaving only a vague resemblance to the original structure.

Coccoliths were subjected to 0.5 ml of 0.25 molar APM at 50°C for 10 minutes. In this reaction, a mass of coccoliths (approximately 60 μg) which originated as approximately 1 μm disks, converted to an unrecognizable clump of sub-micron spherical particles of $CaMoO_4$. EDS confirms the composition of the nodules with gold present from the coating for SEM and aluminum appearing from the SEM sample stub (Figure 4.10). Figure 4.11 shows a coccolith prior to conversion, and the resulting structure obtained after conversion to $CaWO_4$ using 0.05 molar APT solution at 50°C. The general structure was better preserved for the tungstate than in the case of the molybdate.

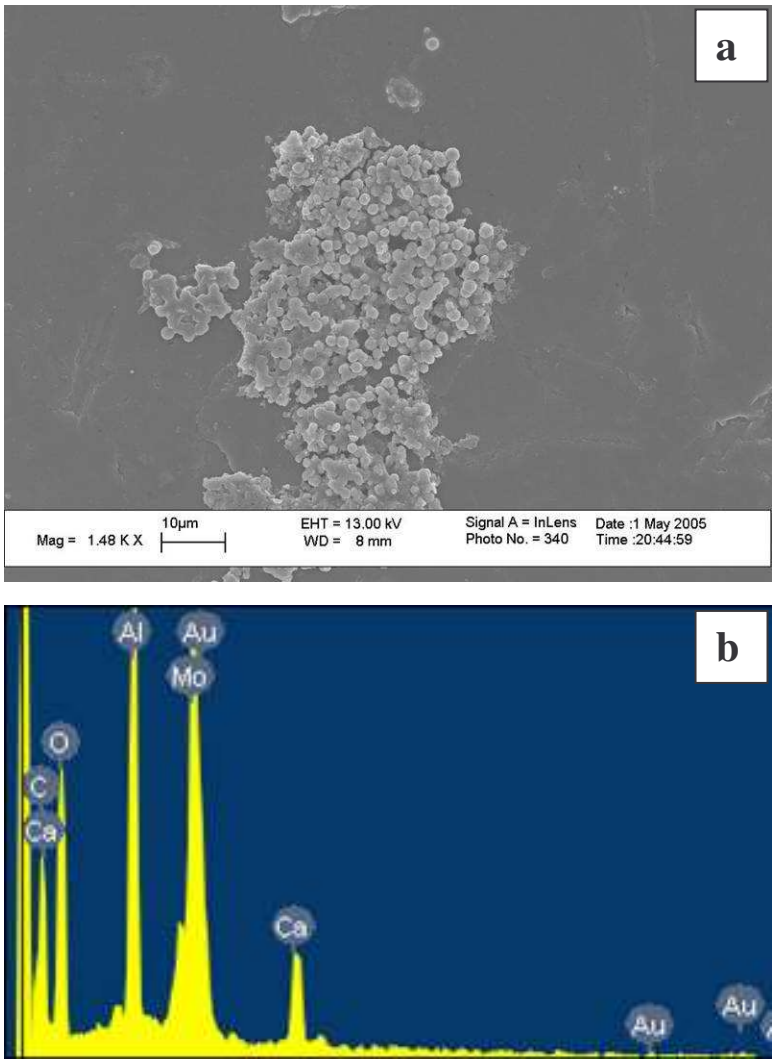


Figure 4.10 (a) SEM of $CaMoO_4$ converted coccolithophore after 10 minutes reaction at 50°C in 0.25 M APM. (b) EDS of converted coccoliths.

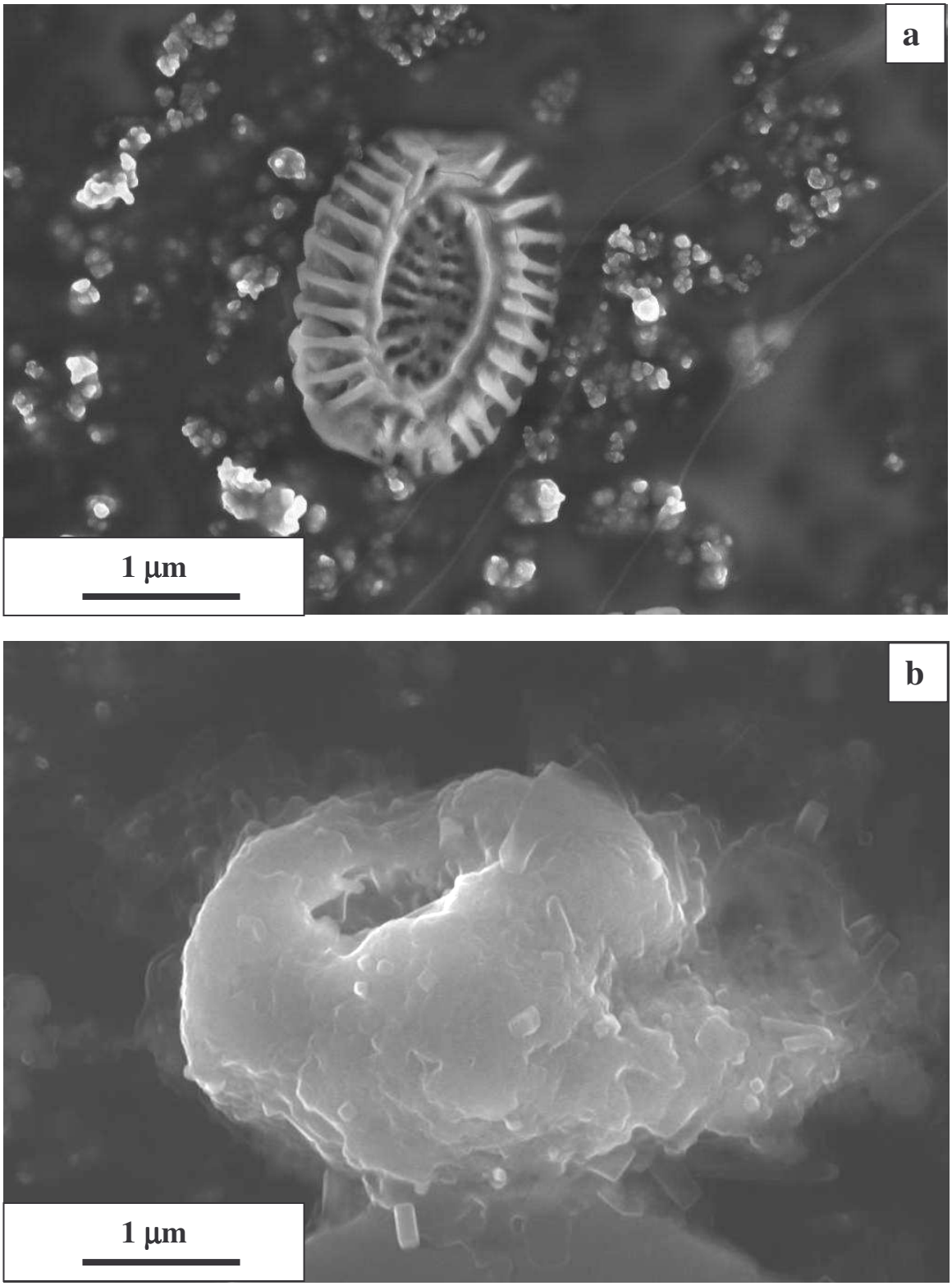


Figure 4.11. SEM of *Emiliania huxleyi* lith (a) unconverted, (b) after reaction with 0.05 M APT to form $CaWO_4$ at 80°C for 10 minutes.

## 4.4 Conclusion

Bioclastic calcium carbonate structures provide new opportunities for exploring shape-preserving inorganic reactions for a variety of applications. It was shown that calcium molybdate and calcium tungstate can be formed from direct reaction with calcium carbonate at temperatures as low as 50°C, without special drying or calcining. Calcium chromate was only produced after calcining to at least 700°C. These methods were less successful at producing shape-preserved microfeatures than certain reactions involving silica structures; however additional manipulation of reaction time, temperature and solution concentration may eventually yield a favorable process for producing precisely shaped nanostructures in $CaWO_4$ and $CaMoO_4$.

# CHAPTER 5

## QUALITATIVE INVESTIGATION OF SIO FORMATION AND THE CONVERSION OF SILICA DIATOMS FRUSTULES TO $LI_2O$.

In the original work by Sandhage, *et. al.,* regarding the new bioclastic route to self-assembled 3D micro structures, the reaction of silica diatom 'templates' with magnesium vapor to produce MgO structures was presented with impressive shape retention. The paper presented a challenge to go beyond MgO and explore other displacement reactions that could be used to create a wide array of materials in shapes never before produced synthetically (from a palette of some 100,000 diatoms to choose!). The new suggested chemistries included aluminum oxide, titanium dioxide, calcium oxide, iron oxide, lithium oxide, niobium oxide, strontium oxide, tantalum oxide, titanium oxide, and zirconium dioxide[10].

In the last two years, several of these chemistries have been researched. For example, titanium dioxide and calcium oxide have been demonstrated and published by other researchers in the group[43, 60]. Other recent investigations have focused on issues with creating phase-pure oxide structures, (*i.e.*, understanding the role of the silicon from the starting template in the reaction and how it may be removed from the system [Chapter 2]).

In certain conversions proposed by Sandhage where the new cation is introduced as a halide gas (such as for titanium dioxide, zirconium dioxide or iron oxide) the silicon product would be a gaseous silicon halide ($SiF_4$, $SiCl_4$, etc.)[10]. The optimum reaction conditions appear to be achieved when the rate of new halide approaching the reaction surface and the rate of silicon halide leaving the surface are balanced in such a way that

shape is preserved and coarsening is minimized[60]. Phase purity of products in these reactions would be facilitated by the removal of silicon as a gaseous species, perhaps in its entirety.

Other conversions, in which the new cation is introduced as a metal vapor (such as magnesium oxide, calcium oxide and lithium oxide), produce solid silicon byproducts. In the magnesium oxide reaction for example, these products were observed in the forms of Si and $Mg_2Si$. Quite possibly the silicon byproduct may be permissible or even functional for certain applications, however, the ability to produce a phase pure structure via this type of reaction is severely limited by the presence of residual silicon. To counter this problem, several methods were explored for removing both silicon and magnesium silicide from magnesium oxide frustules, including etching by sodium hydroxide, chlorine gas, and anhydrous hydrogen chloride gas (Chapter 2).

In study of the magnesia reaction, no magnesium silicates were found to occur as intermediate species in the reaction. This was verified by both XRD of numerous samples and TEM of reaction fronts in individual diatoms. Another possible intermediate-byproduct was silicon monoxide (SiO). It was uncertain as to whether SiO (silicon monoxide) formed as a product due to amorphous nature of SiO which makes its detection difficult. The methods capable of resolving SiO's presence include EXAFS, EELS, ESI, XPS and XANES. FTIR would be helpful if the Si-O bond produced a detectable double bond. However Schnurre's conclusions imply that such analysis may be unfruitful:

"[Amorphous] SiO is not a classical homogenous single phase. Neither is it a classical heterogeneous two-phase mixture [of Si and $SiO_2$] because of the large fraction of atoms belonging to the interphase domain, or in other words the absence of sharp phase boundaries with negligible volume

fraction…. Solid silicon monoxide may be classified as an only globally stoichiometric compound with composition fluctuations in this highly amorphous phase."[54, 84-86]

A question that remained was whether SiO played a role in the magnesium reaction. Thermodynamically, it was uncertain as to the role that SiO would play due to the general lack of data on the solid material. Using SiO data recently published by Schnurre and the MgO data provided in Barin, SiO formation would be thermodynamically favorable in the Mg-$SiO_2$ system above 744°C[54, 58]. However, Barin's data was revised by Gourishankar *et. al.*, and the correction brings the low temperature limit for equilibrium SiO retention to 904 °C[62] (Figure 5.1) using the standard Gibbs free energies. An attempt was made to test Gourishankar's correction by blending Mg granules (Alfa, 99.5% granules) and SiO powder (Alfa Aesar, optical grade) with a 1 to 1 molar ratio in a sealed iron ampoule (similar to the diatom reaction) and firing at 827°C for 2 hours and another sample at 1000°C for 2 hours and quenching the reaction ampoules in water to preserve any high temperature phases. At 827°C, the materials reacted to form MgO, Si and $Mg_2Si$, which supported the Gourishankar correction to the Barin data. At 1000°C the SiO powder bed partially reacted to form Si and $Mg_2Si$ was observed by the black and blue colors in the powder bed. This result may indicate that the high pressure environment within the reaction ampoules may deviate significantly from the standard state predictions. Another possible conclusion, given the incomplete reaction of the SiO powder bed (despite the use of excess Mg), might be that reaction occurred as the tube was heated past 904°C, but further reaction was impeded at higher temperatures. The standard $\Delta G_f$ for SiO was calculated from the equation

published by Schnurre in a thorough review of the thermodynamic data on the Si-O system[54].

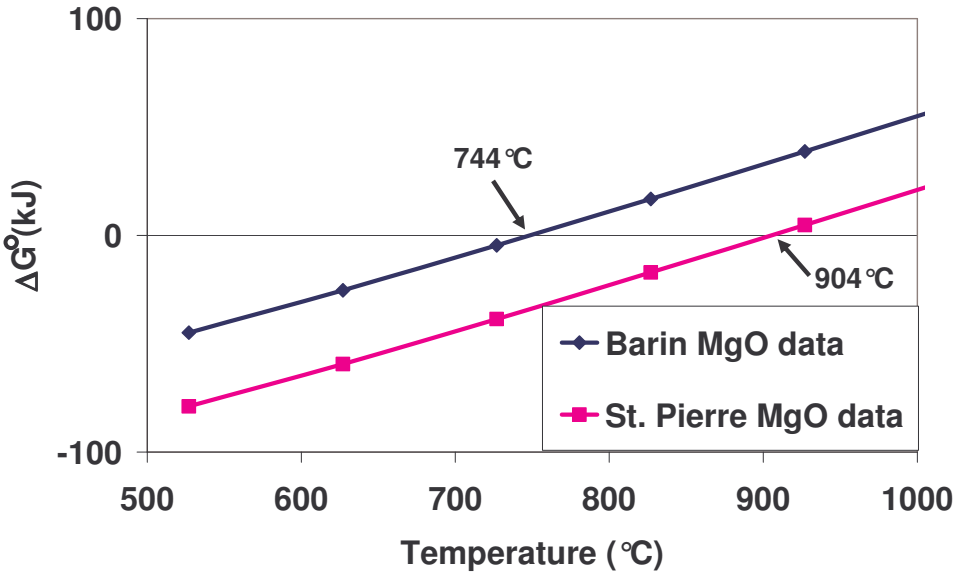


Figure 5.1. Standard Gibbs free energy for the reaction of Mg + SiO → MgO + Si reaction versus temperature.

There were several indicators for the presence of SiO in the reaction products, but no readily available method to determine it analytically. XPS detected shifted Si 2p peaks, but the shift may have been due to the Mg-Si bond ($Mg_2Si$ was found in the samples by XRD) or simply due to the native $SiO_2$ layer on the silicon particles. Qualitative physical characteristics of SiO include brown color[54, 56, 57, 87] and a relatively high vapor pressure, which gives the material a "skunk" like odor, as reported by several MSDSs. Given this information, it was noted that occasionally the diatoms showed a brown color in some region in addition to the black of the Si rich regions and the blue of the $Mg_2Si$ regions. The brown region typically appeared on the opposite end of the powder bed as the blue region, meaning the colors proceeded from brown to black to blue

(Figure 1.5). This appeared to correspond to a logical progression of the local Mg to $SiO_2$ ratio, where 1 Mg per $SiO_2$ yielded SiO (brown), 2 Mg yield Si (black), and 4 Mg yield $Mg_2Si$ (blue).

Also, after removal of the silicon from the MgO (Chapter 2) in the black, "Si", region by sodium hydroxide etching, the MgO diatoms retain a brown color, rather than the expected white of MgO. This brown color had several possible explanations aside from SiO, particularly contaminants from the original diatom material (Al, Na, Ca), or even residual Si that remained after etching.

A foul smell was noted to emanate from the ampoules when cut open, similar to that described by the MSDS sheets. Oftentimes, the inside of the iron ampoules were coated with a brown powder deposit that may have been SiO. In fact, Potter described this condensed phase as a "soft, brown, very fine and voluminous deposit on all exposed surfaces within the furnace."[56] The presence of SiO is significant as an intermediate stage in the MgO conversion process (which was previously believed to be a one-step reaction process), and also for the associated health risks of inhalation of SiO fume (i.e., silicosis).

The conclusion that SiO gas is formed in the MgO reaction was inadvertently validated by a preliminary study on the conversion of $SiO_2$ to $Li_2O$.

a. $SiO_2 + 4Li \rightarrow 2Li_2O + Si$

This reaction was proposed in Sandhage's original paper on shape preserving displacement reactions[10]. The experiment was designed similar to the magnesium reaction, where Li granules were placed at one end of an iron ampoule and silica diatoms were placed in an iron boat at the opposite end. Air was excluded by welding the

ampoules shut in an argon glove box. Lithium is positioned higher on the Ellingham diagram[88] that magnesium so sealing in argon may not be necessary, however by doing so, any compounds produced in the experiment must only come from the Li and $SiO_2$ from the reactant species. This reaction was attempted at 900ºC and 700ºC for 2 hours at each temperature. At 900ºC, the diatom powder bed became a fused mass of $Li_2SiO_3$, $Li_4SiO_4$, and Si. However, at 700ºC, 4 distinct reaction zones were observed (analogous to the reaction zones observed in MgO). In the first zone, the diatoms became light gray, but no lithium compounds were detected by XRD (Figure A.2). In the second color zone, lithium meta-silicate, $Li_2SiO_3$, was observed along with $Li_4SiO_4$ and $Li_{13}Si_4$. In the third zone, which appeared dark green, $Li_2SiO_3$ was accompanied by $Li_4SiO_4$, $Li_2O$ and $Li_{13}Si_4$. In the fourth region, mainly $Li_2O$ was observed by XRD with very little lithium silicate remaining. Interestingly no significant silicon containing phase was detected in the fully converted region, *i.e.*, the silicon, if present must be amorphous, possibly as SiO. Another possible net reaction to explain the absence of a crystalline silicon phase in the fully converted region could be:

b. $2\ Li + SiO_2 \rightarrow Li_2O + SiO$

A review of the lithium reaction by way of the observed phases results in the following series of equations:

c. $2\ Li + 2\ SiO_2 \rightarrow Li_2SiO_3 + SiO$

d. $4\ Li + 3\ SiO_2 \rightarrow 2\ Li_2SiO_2 + Si$

e. $Li_2SiO_3 + 2\ Li + SiO \rightarrow Li_4SiO_4 + Si$

f. $Li_2SiO_3 + 2\ Li + SiO_2 \rightarrow Li_4SiO_4 + SiO$

g. $Li_4SiO_4 + 4\ Li \rightarrow 4\ Li_2O + Si$

Unlike the magnesium reaction, the complex lithium reaction proceeded through two distinct crystalline intermediates and an intermetallic before lithium oxide was obtained. As no silicon was found in the XRD analysis, it appears that in the process to create $Li_2O$, SiO may have been generated. It was noted that the same foul smell associated with the iron ampoules from the magnesium oxide reaction was observed when the lithium reaction ampoules were opened. The only possible chemical products in common with the two reactions were Si and SiO. As Si was reported to be odorless and was not detected in XRD of the lithium reaction products, the qualitative observations and results suggested that SiO formed as a reaction intermediate in both the lithium oxide and magnesium oxide reactions.

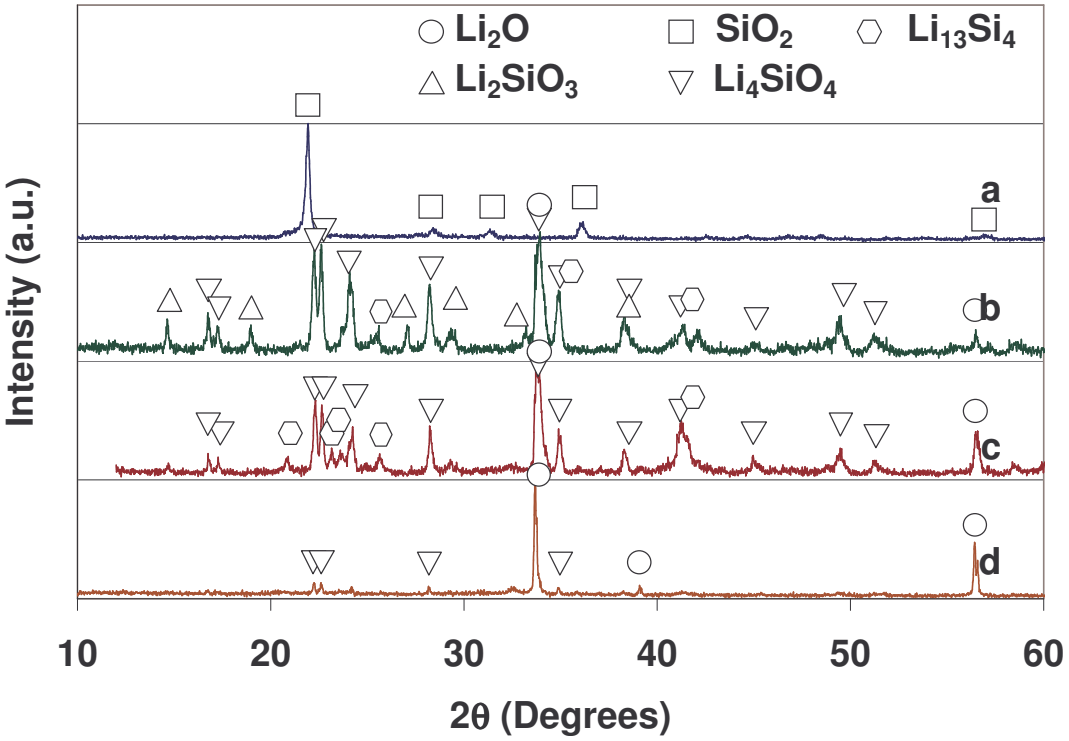


Figure 5.2. XRD of silica conversion to lithium oxide at 700°C in 2 hours. Samples were taken from 4 reactions zones in the same sample showing the progression of the reaction. (a) Unconverted $SiO_2$, (b) $Li_2SiO_3$, $Li_4SiO_4$, and $Li_{13}Si_4$ appear, no silica remains, (c) silicates are becoming $Li_2O$, no silicon-bearing phase seen, (d) nearly all $Li_2O$ with little crystalline silicon-bearing phase present.

For the magnesium oxide reaction, it was found in the thermodynamic literature that the $\Delta G$ of reaction for $Mg + SiO \rightarrow MgO + Si$ becomes positive above 904ºC. By running the Mg reaction at 900ºC, the likelihood of breaching 904ºC and locking in SiO is very good. As the ampoules are often removed directly from the 900ºC furnace, there is little time for the remaining SiO to be consumed by Mg vapor in the ampoule. Another criticism of the magnesium reaction process is that controlling the furnace temperature with a thermocouple inside the tube (rather than the furnace thermocouple) is liable to result in overheating of one end of the furnace if the thermocouple is not placed exactly in the center of the furnace's length. While we have shown that the largest diatom batches can be processed in the shortest relative time at 900ºC, there may be a distinct advantage to decreasing the reaction temperature by just 15 or 25º.

The second significant finding of this work is that the vapor transported lithium reaction suggested in the original Sandhage paper is feasible. Shape preservation was not observed in a manner agreeable with the magnesium oxide reaction, but as these were only preliminary experiments, these may find usefulness as a starting point for generating shape preserved $Li_2O$ structures (Figure 5.3). Advantages of $Li_2O$ over MgO, CaO or SrO, include resistance to hydroxylation and carbonation (higher position on the Ellingham diagram) and ultra-low density.

This work serves as evidence that not only can the diversity of shape preserving reactions with silica continue to be broadened, but also that we can learn more about the reactions we are studying by looking beyond to new reactions. The learning curve in the development of new fabrication techniques is steep, and for bioclastic 3D microfabrication (the BaSIC process), this thesis serves as a ladder to climb.

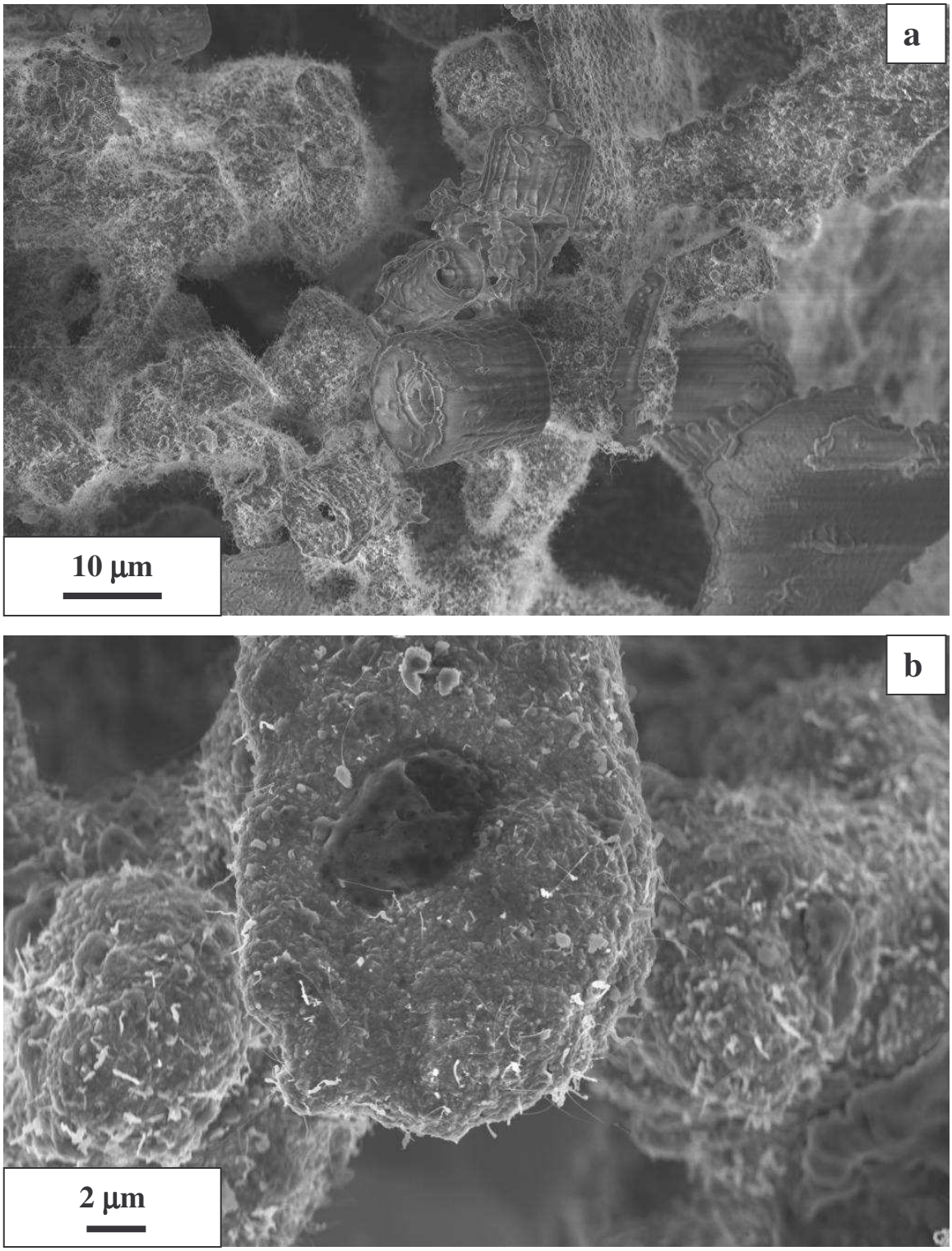


Figure 5.3. SEM of lithium conversion materials. (a) Image shows unconverted $SiO_2$ diatoms in matrix of 'converted' material from zone 'b'. (b) A 'fully converted' structure of $Li_2O$ from zone 'd'. Possibly a shape-preserved Lithia structure exists under a coating of amorphous SiO and $SiO_2$. Lithium can not be analyzed by EDS so no exact phase information could be determined in SEM.

## APPENDIX A

## LIST OF MATERIALS

| Material | Supplier |
|---|---|
| *Aulacoseira* $SiO_2$ Diatoms | Recreational Water Products, Stockbridge, GA |
| *Melosira* $SiO_2$ Diatoms | DiaSource Inc., Boise, ID |
| Mg flakes, 99.5% | Alfa Aesar |
| Tungstic acid | Alfa Aesar |
| Lithium granules | Alfa Aesar |
| Ammonium para-tungstate | Alfa Aesar |
| Ammonium para-molybdate | Alfa Aesar |
| 1020 Iron tubing | TW Metals, Easton, PA |
| $CaCO_3$ Sand dollars | The Shell Factory, Fort Myers, FL |
| $CaCO_3$ Coccolithophores | Scripps Oceanographic Institute, UCSD, San Diego, CA |
| Sodium hydroxide | Alfa Aesar |

# APPENDIX B

# ASSAY OF MATERIALS

## B.1. Assay of Sodium Hydroxide

The sodium hydroxide pellets, used for dissolution of Si in MgO/Si diatom frustules, were assayed for NaOH and $Na_2CO_3$ content by the ACS assay method. In the method, NaOH content was determined for a given mass of NaOH pellets by titrating in deionized, carbon dioxide free water with the drop-wise addition of 1 N hydrochloric acid using phenolphthalein as the indicator. Each 1 ml of 1 N HCl corresponded to 0.04000 g of NaOH. At the phenolphthalein endpoint, methyl orange was added to the solution. Additional 1 N HCl was added drop-wise until the methyl orange endpoint was reached. Each 1 ml of 1 N HCl added from the phenolphthalein endpoint to the methyl orange endpoint corresponded to 0.05300 g of $Na_2CO_3$. The results of the titration of the sodium hydroxide pellets yielded 95.9% NaOH and 0.4% $Na_2CO_3$ with the balance assumed to be adsorbed water.

## B.2. TGA Assay of Tungsten and Molybdenum Oxide Precursors

Tungstic acid, ammonium para-tungstate and ammonium para-molybdate precursors were assayed using thermogravimetric analysis (TGA) and differential thermogravimetric analysis (DTG). The tungstic acid and ammonium para-molybdate were heated separately to 400°C in 20% oxygen, 80% nitrogen atmosphere at a rate of 5° C per minute. The ammonium para-tungstate was heated to 500°C under the same conditions before removal of the volatile species was complete. The TGA and DTG profiles for tungstic acid, ammonium para-tungstate and ammonium para-molybdate are

provided in Figures B.1, B.2, and B.3, respectively. The tungstic acid assayed as 94.0% $WO_3$, indicating that the $H_2WO_4$ may have lost some water previously, as the predicted $WO_3$ content was 92.7%. The ammonium para-tungstate assayed as 89.1% $WO_3$. This compared with a calculated assay of 89.1% for $(NH_4)_{10}W_{12}O_{41}\cdot 4.5H_2O$. The ammonium molybdate assayed as 81.68% $MoO_3$, which compares with a calculated value of 81.54% for $(NH_4)_6Mo_7O_{24}\cdot 4H_2O$.

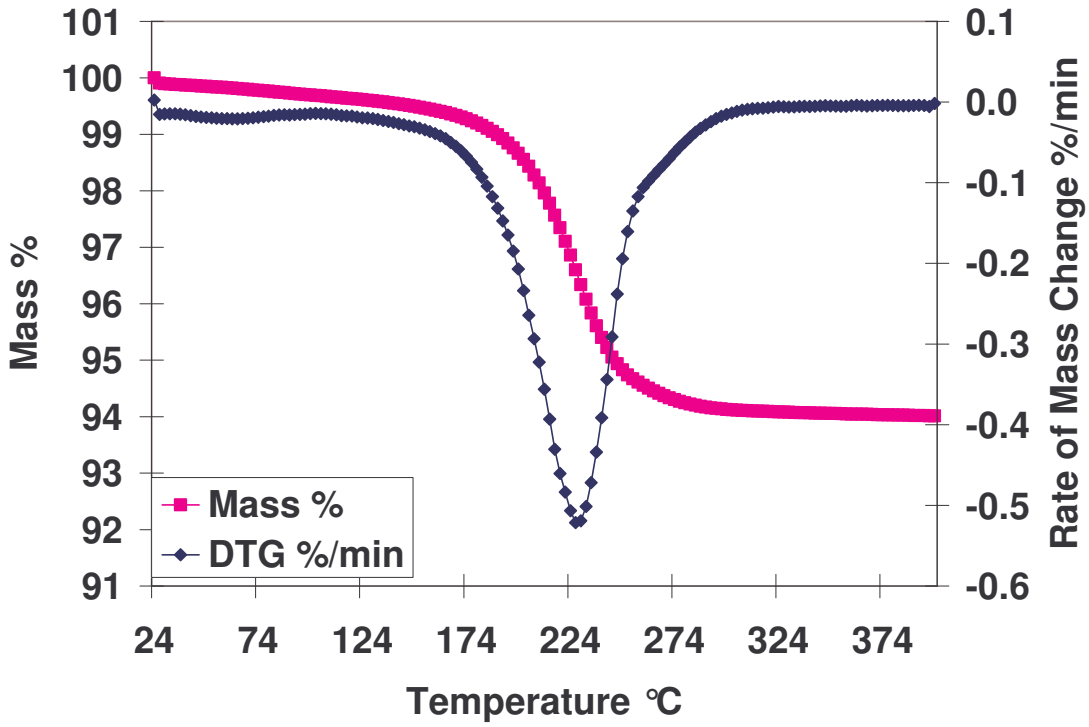


Figure B.1. TGA and DTG profiles for tungstic acid heated at 5°C/min in 20% oxygen, balance nitrogen atmosphere.

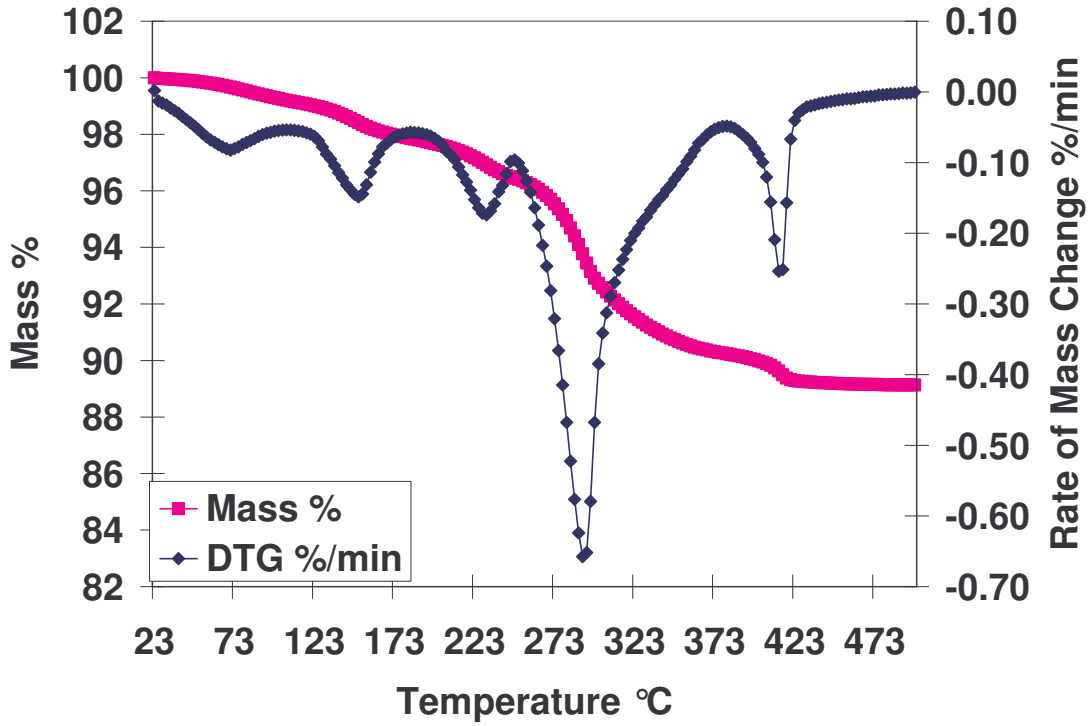


Figure B.2. TGA and DTG profiles for ammonium para-tungstate heated at 5°C/min in 20% oxygen, balance nitrogen atmosphere.

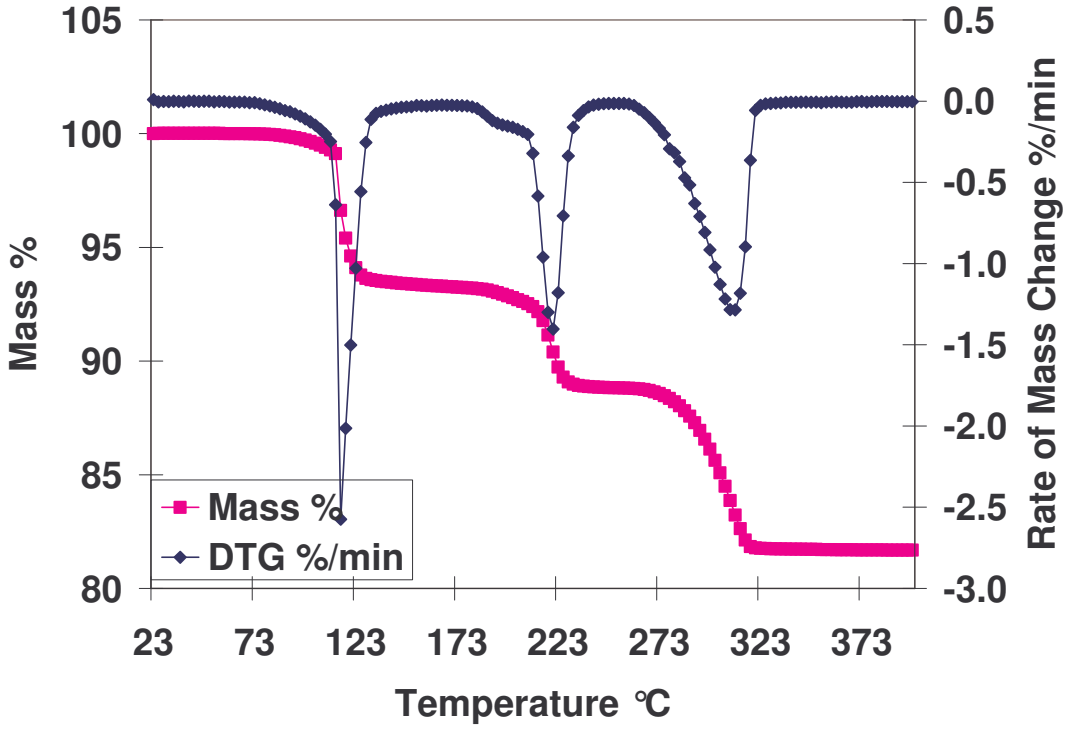


Figure B.3. TGA and DTG profiles for ammonium para-molybdate heated at 5°C/min in 20% oxygen, balance nitrogen atmosphere.

**APPENDIX C**

MgO PROCESS: TIME, TEMPERATURE, REACTANT RATIO MAPS FOR 800°C TO 900°C CONVERSION

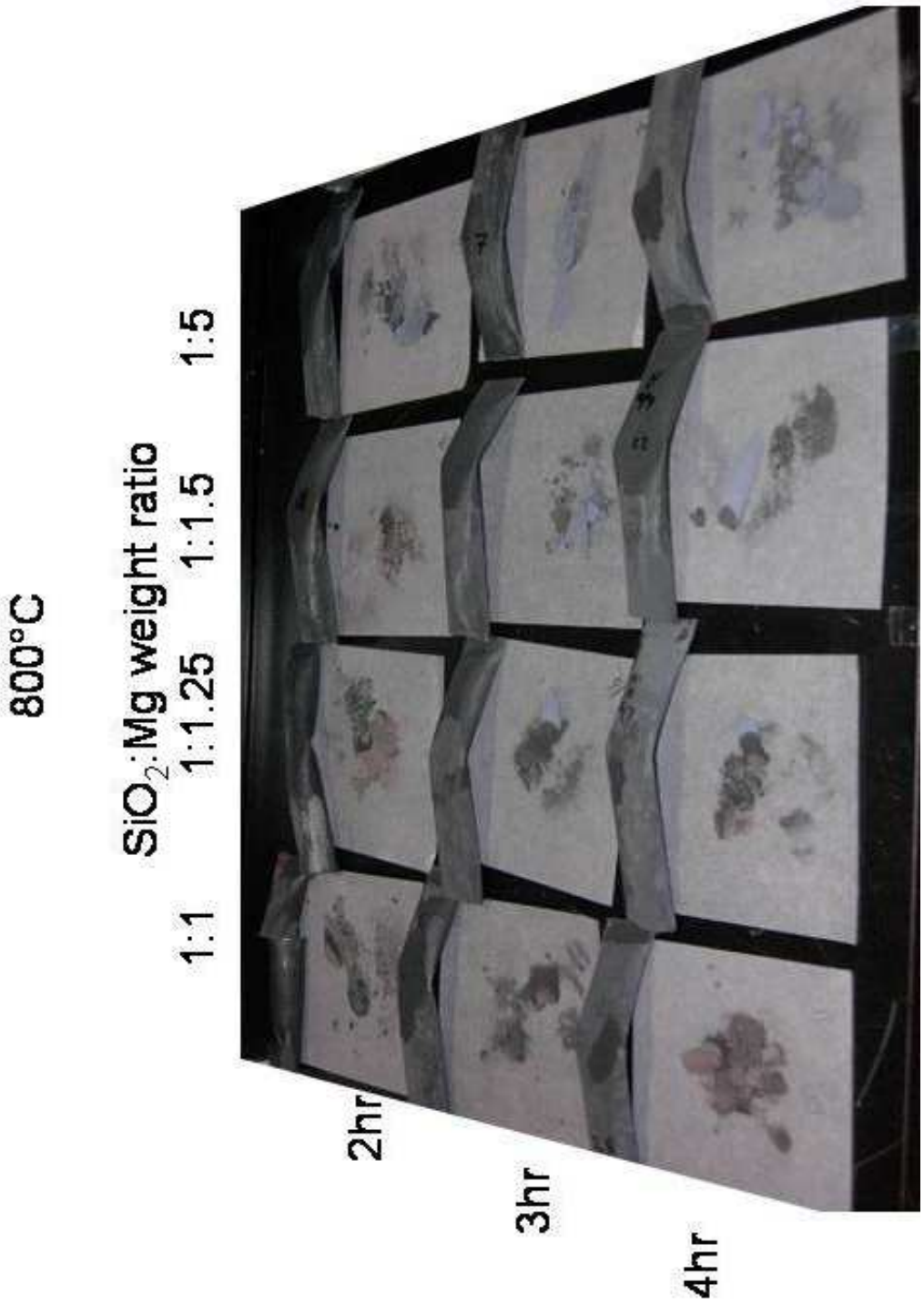


Figure C.1. Matrix of 800°C MgO reaction runs showing progression of reaction by color of powder bed. Higher ratios of Mg to $SiO_2$, and longer run times resulted in greater amounts of $Mg_2Si$ as seen by blue colored powder beds.

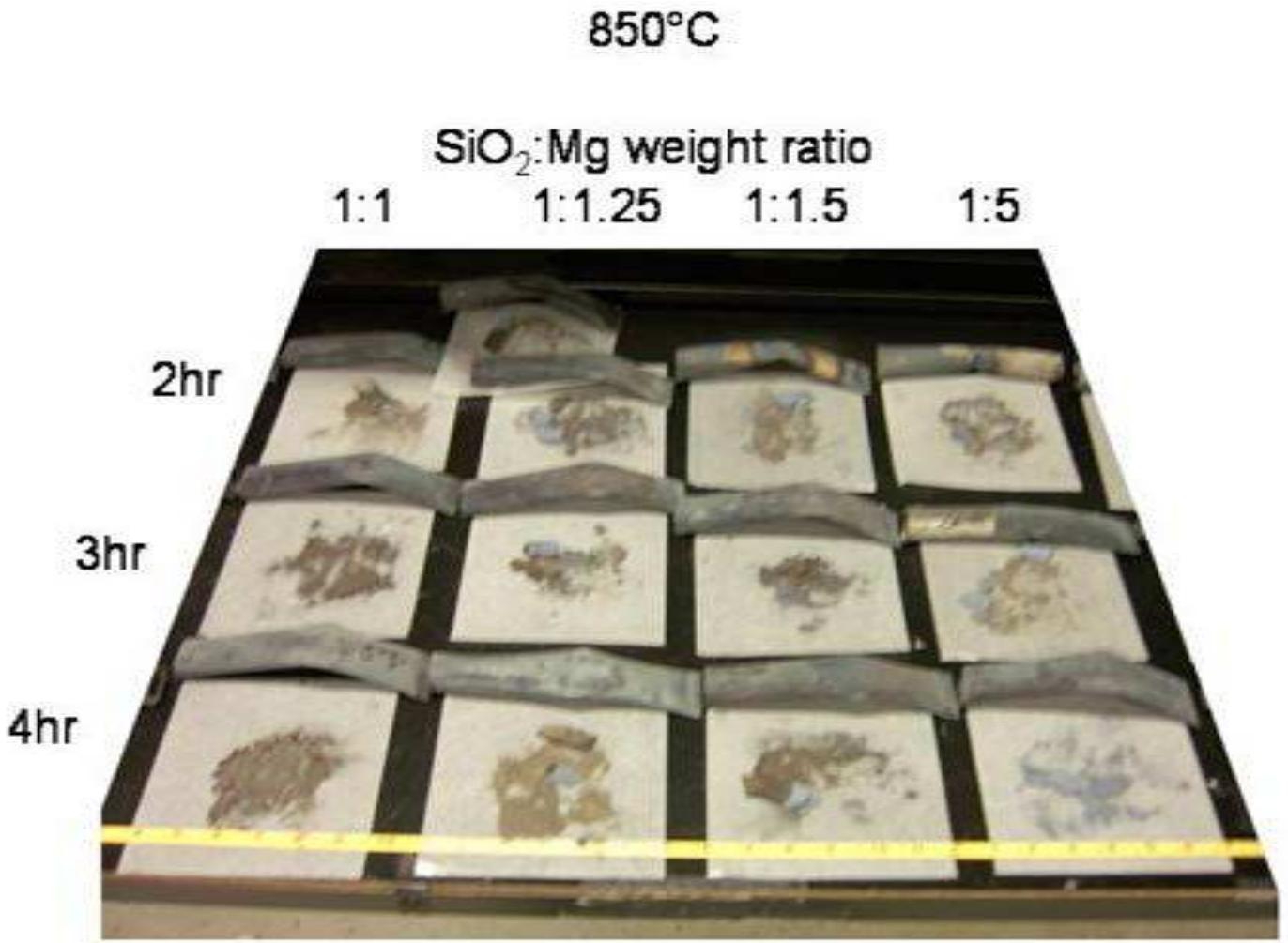


Figure C.2. Matrix of 850°C MgO reaction runs showing progression of reaction by color of powder bed. Higher ratios of Mg to $SiO_2$, and longer run times resulted in greater amounts of $Mg_2Si$ as seen by blue colored powder beds.

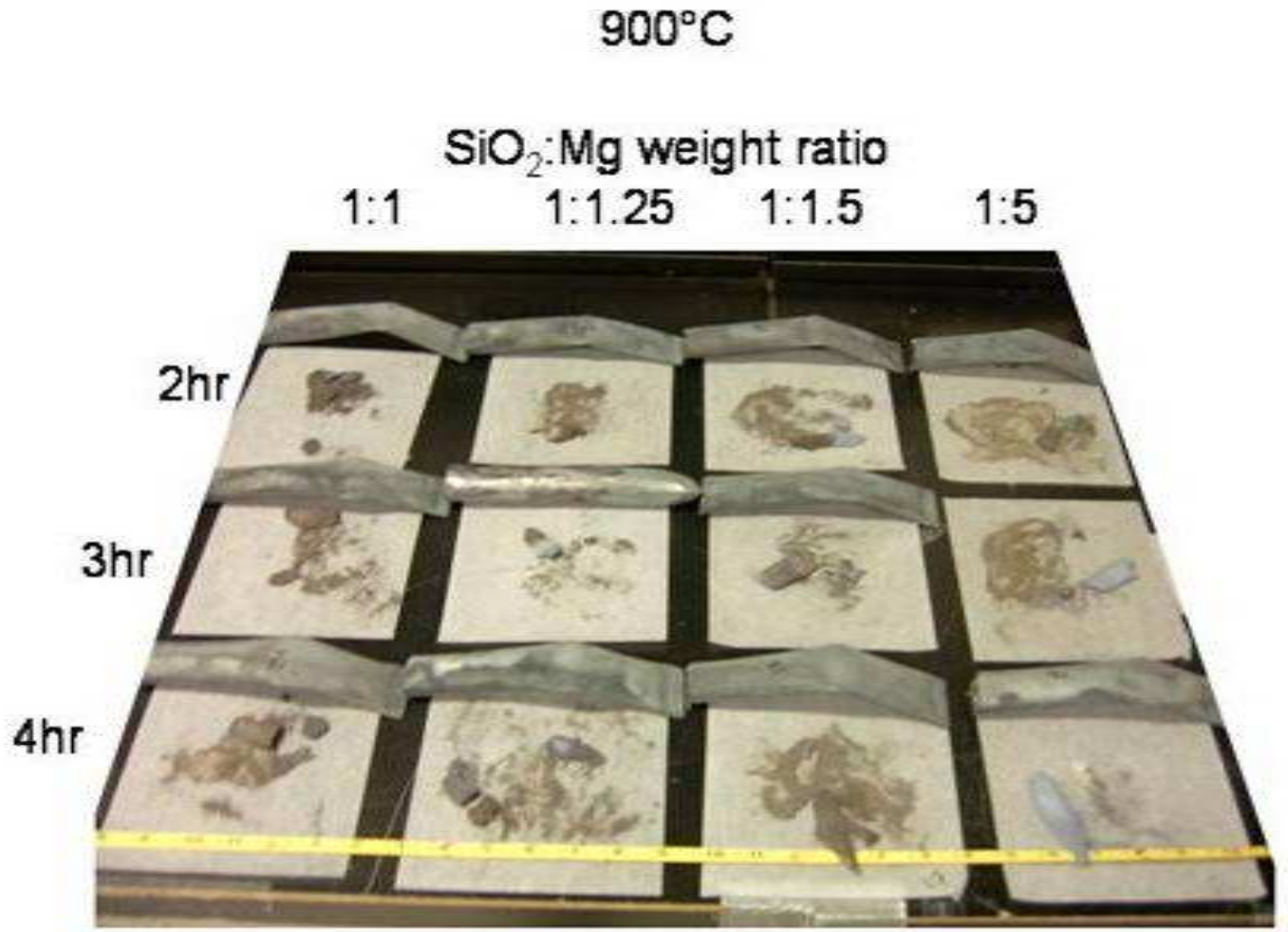


Figure C.3. Matrix of 800°C MgO reaction runs showing progression of reaction by color of powder bed. Higher ratios of Mg to $SiO_2$, and longer run times resulted in greater amounts of $Mg_2Si$ as seen by blue colored powder beds.

## REFERENCES


1. Chen, H.-J.; Chen, Y.-W., Hydrothermal synthesis of barium titanate. *Ind. Eng. Chem. Res.* **2003,** *42*, 473-483.

2. Gu, F.; Wang, S. F.; Lu, M. K.; Zou, W. G.; Zhou, G. J.; Xu, D.; Yuan, D. R., Combustion synthesis and luminescence properties of $Dy^{+3}$ -doped MgO nanocrystals. *J. Cryst. Growth* **2004,** *260*, 507-10.

3. Hreniak, D.; Strek, W.; Amami, J.; Guyot, Y.; Boulon, G.; Goutaudier, C.; Pazik, R., The size-effect on luminescence properties of $BaTiO_3$: $Eu^{3+}$ nanocrystallites prepared by the sol-gel method. *Journal of Alloys and Compounds* **2004,** *380*, 348-351.

4. Nho, J.-S.; Cho, S.-B.; Ryoo, C.-S.; Lee, K.-H.; Kwon, T.-H. Method for preparing single crystalline ZnS powder for phosphor. WO02090262, 2002.

5. Madou, M. J., *Fundamentals of Microfabrication: The Science of Miniaturization*. 2 ed.; CRC Press: Boca Raton, FL, 2002.

6. Kim, S.; Hishita, S., Growing $BaTiO_3$ thin films on Si(100) with MgO-buffer layers by sputtering. *Thin Solid Films* **1996,** *281-282*, 449-452.

7. Becker; al, e., Fabrication of Microstructures with High Aspect Ratios and Great Structural Heights by Synchrotron Radiation Lithography, Galvanoforming, and Plastic Moulding (LIGA Process). *Microelectronic Engineering* **1986,** *4*, (1), 35-36.

8. Hruby; al., e. In *LIGA: Metals, Plastics, and Ceramics*, SPIE Conference on Micromachining and Microfabrication Process Technology V, 1999; 1999; pp 32-43.

9. Morales, A. M.; Winter, M. R.; Domeier, L. A.; Allan, S. M.; Skala, D. M. Fabrication of metallic microstructures by micromolding nanoparticles. 6,472,459, October 29, 2002, 2002.

10. Sandhage, K. H.; Dickerson, M. B.; Huseman, P. M.; Caranna, M. A.; Clifton, J. D.; Bull, T. A.; Heibel, T. J.; Overton, W. R.; Schoenwaelder, M. E. A., Novel, Bioclastic Route to Self-Assembled 3D, Chemically Tailored Meso/Nanostructures: Shape-Preserving Reactive Conversion of Biosilica (Diatoms) Microshells. *Advanced Materials* **2002,** *14*, (6), 429-433.

11. Round, F. E.; Crawford, R. M.; Mann, D. G., *The Diatoms: Biology & Morphology of the Genera*. Cambridge University Press: Cambridge, England, 1990.

12. Lebeau, T.; Robert, J. M., Diatom cultivation and biotechnologically relevant products. Part I: Cultivation at various scales. *Appl. Microbiol. Biotechnol.* **2003,** *60*, 612-23.

13. Lewin, J. C.; Guillard, R. R. L., Diatoms. *Annual review of microbiology* **1963,** *17*, 373-414.

14. Martin-Jezequel, V.; Hildebrand, M.; Brzezinski, M. A., Silicon metabolism in diatoms: Implications for growth. *J. Phycology* **2000,** *36*, 821-40.

15. Werner, D., *The Biology of Diatoms*. Blackwell Scientific: Oxford, England, 1997.

16. Dolley, T. P., *Minerals Yearbook: Volume I. -- Metals and Minerals*. U. S. Government Printing Office: Washington, DC, 2002; p 24.1-24.6.

17. Wee, K. M.; Rogers, T. N.; Altan, B. S.; Hackney, S. A.; Hamm, C., Engineering and medical applications of diatoms. *Journal of Nanoscience and Nanotechnology* **2005,** *5*, (1), 88-91.

18. Parkinson, J.; Gordon, R., Beyond Micromachining: The potential of diatoms. *Trends in Biotechnology* **1999,** *17*, 190-6.

19. Sandhage, K. H.; Dickerson, M. B.; Huseman, P. M.; Caranna, M. A.; Clifton, J. D.; Bull, T. A.; Heibel, T. J.; Overton, W. R.; Schoenwaelder, M. E. A., Novel, Bioclastic Route to Self-Assembled, 3D, Chemically Tailored Meso/Nanostructures: Shape-Preserving Reactive Conversion of Biosilica (Diatom) Microshells. *Advanced Materials* **2002,** *14*, (6), 429-433.

20. Unocic, R. R.; Zalar, F. M.; Sarosi, P. M.; Cai, Y.; Sandhage, K. H., Anatase assemblies from algae: coupling biological self-assembly of 3-D nanoparticle structures with synthetic reaction chemistry. *Chemical Communications* **2003,** *7*, 796-7.

21. Weatherspoon, M. R.; Allan, S. M.; Hunt, E.; Cai, Y.; Sandhage, K., Sol-gel synthesis on self replicating single-cell scaffolds: applying complex chemistries to nature's 3-D nanostructured templates. *ChemComm* **2005**, 651-653.

22. Buchal, C.; Beckers, L.; Eckau, A.; Schubert, J.; Zander, W., Epitaxial $BaTiO_3$ thin films on MgO. *Materials Science and Engineering* **1998,** *B56*, 234-238.

23. Lisoni, L. G.; Siegert, M.; Lei, C. H.; Biegel, W.; Schubert, J.; Zander, W.; Buchal, C., The growth of MgO buffer layers on sapphire for the epitaxy of BaTiO3 optical thin films. *Thin Solid Films* **2001,** *389*, (1,2), 219-26.

24. Blanchard, G.; Bordes, E.; Ferre, G. Ammoxidation of saturated hydrocarbons. 5,556,984, 1996.

25. Lee, E.-K.; Jung, K.-D.; Joo, O.-S.; Shul, Y.-G., Catalytic activity of Mo/MgO catalyst in the wet oxidation of $H_2S$ to sulfur at room temperature. *Applied Catalysis, A* **2004,** *268*, 83-88.

26. Choudary, B. M.; Kantam, M. L.; Ranganath, K. V. S.; Mahendar, K.; Sreedhar, B., Bifunctional nanocrystalline MgO for chiral epoxy ketones via Claisen-Schmidt condensation-assymetric epoxidation reactions. *Journal of the American Chemical Society* **2004,** *126*, (11), 3396-7.

27. Copp, A. N., Magnesia/Magnesite. *Bull. Am. Ceram. Soc.* **1995,** *74*, (6), 135-7.

28. Fenelonov, V. B.; Mel'gunov, M. S.; Mishakov, I. V.; Richards, R. M.; Chesnokov, V. V.; Volodin, A. M.; Klabunde, K. J., Changes in texture and catalytic activity of nanocrystalline MgO during it's transformation to $MgCl_2$ in the reaction with 1-chlorobutane. *J. Phys. Chem. B* **2001,** *105*, (18), 3937-41.

29. Frith, M.; Buffrey, T.; Strawbridge, I., Magnesia: A Refractories Manufacturer Perspective. *Br. Ceram. Trans.* **1998,** *97*, (1), 29-34.

30. Frost, M. T.; Jones, M. H.; Flann, R. C.; Hart, R. L.; Strode, P. R.; Urban, A. J.; Tassios, S., Application of caustic calcined mangesia to effluent treatment. *Trans. Inst. Mining Metall.* **1990,** *99*, C117-24.

31. Giroud, F.; Nocerino, C. Cosmetic compositions comprising magnesium oxide particles. 2,822,684, 2002.

32. Hobson, S. T.; Jr., E. H. B.; Lehnert, E. K.; Klabunde, K. J.; Koper, O. P.; Decker, S. Active topical skin protectants using reactive nanoparticles. 2002.

33. Kizuka, T.; Ichinose, H.; Ishida, Y., Structure and mechanical properties of nanocrystalline Ag/MgO composites. *J. Mater. Sci.* **1994,** *29*, (12), 3107-12.

34. Kon, R.; Miyazaki, M., Application of the Nano-Technology for antiperspirants. Development of the novel deodorant powder. *Fragrance Journal* **2003,** *31*, (8), 63-68.

35. Koper, O. B.; Klabunde, J. S.; Marchin, G. L.; Klabunde, K. J.; Stoimenov, P.; Bohra, L., Nanoscale powders and formation s with biocidal activity toward spores and vegetative cells of Bacillus species, viruses, and toxins. *Curr. Microbiol.* **2002,** *44*, 49-55.

36. Mortvedt, J. J.; Kelsoe, J. J., Crop Response to Fine and Granular Magnesium Fertilizers. *Fertilizer Research* **1988,** *15*, (2), 155-61.

37. Nakayama, T.; Kim, B. S.; Kondo, H.; Choa, Y. H.; Sekine, T.; Nagashima, M.; Kusunose, T.; Hayashi, Y.; Niihara, K., Fabrication of MgO based nanocomposites with multifunctionality. *J. Eur. Ceram. Soc* **2004,** *24*, 259-64.

38. Palmer, J. Removing sulfur dioxide from a gaseous stream. 4,867,961, 1989.

39. Shimizu, Y.; Terasaki, M.; Kashihara, S., Magnesia porous particle separators for lithium-aluminum/iron sulfide batteries. *J. Power Sources* **1984,** *13*, (3), 235-44.

40. Spychaj, S.; Balta-Calleja, F. J., Mechanical properties of hardened unsaturated polyester resins thickened with magnesium oxide. *J. Mater. Sci. Lett.* **1993,** *12*, (16), 1255-7.

41. Steger, J. F.; Palmer, J. W. Magnesia-based coatings for preventing silicon-steel sheets from acquiring hard silicate surfaces during annealing. 3,582,407, 1971.

42. Mishakov, I. V.; Zaikovskii, V. I.; Heroux, D. S.; Bedilo, A. F.; Chesnokov, V. V.; Volodin, A. M.; Martyanov, I. N.; Filimonova, S. V.; Parmon, V. N.; Klabunde, K. J., $CF_2Cl_2$ Decomposition over nanocrystalline MgO: Evidence for long induction periods. *Journal of Physical Chemistry B* **2005,** *109*, 6982-6989.

43. Zalar, F. Shape-preserving conversion of silica-based bioclastic structures into magnesia and calcia via the BaSIC process. The Ohio State University, Columbus, OH, 2003.

44. Allan, S.; Weatherspoon, M.; Graham, P.; Cai, Y.; Haluska, M.; Snyder, R.; Sandhage, K. In *Shape-preserving chemical conversion of self-assembled 3-D bioclastic mciro/nanostructures via low-temperature displacement reactions*, 29th International Cocoa Beach Conference on Advanced Ceramics and Composites, Cocoa Beach, FL, 2005; Kriven, W., 'Ed." Cocoa Beach, FL, 2005.

45. Cai, Y.; Allan, S. M.; Sandhage, K. H.; Zalar, F., Three-dimensional magnesia-based nanocrystal assemblies via low-temperature magnesiothermic reaction of diatom microshells. *Journal of the American Ceramic Society* **2005,** *88*, (7), 2005-2010.

46. Dickerson, M. B.; Naik, R. R.; Sarosi, P. M.; Agarwal, G.; Stone, M. O.; Sandhage, K. H., Ceramic nanoparticle assemblies with tailored shapes and tailored chemistries via biosculpting and shape-preserving inorganic conversion. *Journal of Nanoscience and Nanotechnology* **2005,** *5*, (1), 1-4.

47. Razmyslov, V. I. Method for reducing silicon. 2036143, May 27, 1995, 1995.

48. Banerjee, H. D.; Sen, S.; Acharya, H. N., Investigations on the Production of Silicon from Rice Husks by the Magnesium Method. *Materials Science and Engineering* **1982,** *52*, 173-179.

49. Acharya, H. N.; Dutta, S. K.; Banerjee, H. D., Production of magnesium silicide and silane from rice husk ash. *Solar Energy Materials* **1980,** *3*, 441-445.

50. Wynnyckyj, J. R.; Bhogeswara Rao, D., The Mechanism of Reduction of silica by Magnesium Vapor. *High Temperature Science* **1976,** *8*, (3), 203-217.

51. Cutler, R. A.; Rigtrup, K. M., Synthesis, Sintering, Microstructure, and Mechanical Properties of Ceramics Made by Exothermic Reactions. *Journal of the American Ceramic Society* **1992,** *75*, (1), 36-43.

52. Williamson, G. K.; Hall, W. H., X-ray Line Broadening from Filed Aluminium and Wolfram. *Acta Metallurgica* **1953,** *1*, 22-31.

53. Flörke, O. W., The modification of silica. *Fortschritte der Mineralogie* **1967,** *44*, (2), 181-230.

54. Schnurre, S. M.; Grobner, J.; Schmid-Fetzer, R., Thermodynamics and phase stability in the Si-O system. *Journal of non-crystalline solids* **2004,** *336*, 1-25.

55. Evons, D., DiaSource Chemical Analysis Data Sheet. In Allan, S., 'Ed."; DiaSource, Inc.: Boise, ID, 2004.

56. Potter, H. N., *Transactions of the American Electrochemical Society* **1907,** *12*, 191.

57. Winkler, C., *Ber. Dt. Chem. Ges.* **1890,** *22*, 2652.

58. Barin, I., *Thermochemical data of Pure Substances, 3rd edition*. VCH Verlagsgesellschaft mbH: Weinheim, Germany, 1995; 'Vol.' I and II.

59. Nayeb-Hashemi, A. A.; Clark, J. B., The silicon-magnesium system. *Bull. Alloy Phase Diagr.* **1984,** *5*, 584.

60. Unocic, R. R.; Zalar, F. M.; Sarosi, P. M.; Cai, Y.; Sandhage, K. H., Anatase assemblies from algae: coupling biological self-assembly of 3-D nanoparticle structures with synthetic reaction chemistry. *Chemical Communications* **2004,** *7*, 796-7.

61. Flamm, D. L., Mechanisms of silicon etching in fluorine- and chlorine-containing plasmas. *Pure & Appl. Chem.* **1990,** *62*, (9), 1709-1720.

62. Gourishankar, K. V.; Ranjbar, M. K.; St. Pierre, G. R., Revision of the enthalpies and Gibbs energies of formation of calcium oxide and magnesium oxide. *Journal of Phase Equilibria* **1993,** *14*, (5), 601-11.

63. Seiter, H.; Sirtl, E., Removal of silicon in the system silicon-chlorine-hydrogen. *Zeitschrift fuer Naturforschung, Teil A: Astrophysik, Physik und Pysikalische Chemie* **1966,** *21*, (10), 1696-702.

64. Kobayashi, M.; Matsuo, Y.; Nishiwaki, K.; Ono, K.; Yamamoto, K. Production of silicon tetrachloride from chlorine and silicon. 2002173313, 2002.

65. Removal of silicon in silicon nitride. 59035008, 1984.

66. Lee, R. Y.; Zhang, F. L.; Penczek, J.; Wagner, B. K.; Yocom, P. N.; Summers, C. J., Investigation of Ce-doped silicates for low voltage field emission displays. *Journal of Vacuum Science & Technology B: Microelectronics and Nanometer Structures* **1998,** *16*, (2), 855-857.

67. Jung, H.-K.; Lee, D.-W.; Jung, K. Y.; Boo, J.-H., Fabrication of dense $BaMgAl_{10}O_{17}:Eu^{2+}$ phosphor particles by spray pyrolysis. *Journal of Alloys and Compounds* **2005,** *390*, 189-193.

68. Kang, Y. C.; Kim, E. J.; Lee, D. Y.; Park, H. D., High brightness LaPO4:Ce,Tb phosphor particles with spherical shape. *Journal of Alloys and Compounds* **2002,** *347*, (1-2), 266-270.

69. Gordon, R.; Sterrenburg, F. A. S.; Sandhage, K. H., A special issue on diatom nanotechnology. *Journal of Nanoscience and Nanotechnology* **2005,** *5*, (1), 1-4.

70. Wolfe, R. W.; Lenox, J. J.; Tomlinson, T. J. Stir-in fluorescent lamp phosphor and method of making same. 5,207,948, 1993.

71. Complete-spectrum daylight fluorescent lamps. 01143133, 1989.

72. Foulke, T. E. Luminescent material and the method of producing the same. 2,203,682, 6/11/1940, 1940.

73. Fonda, G. R., The Magnesium Tungstate Phosphor. *The Journal of Physical Chemistry* **1944,** *48*, 303-307.

74. Cullity, B. D., *Elements of X-ray Diffraction*. 2 ed.; Addison-Wesley: Reading, MA, 1976.

75. Bludsuss, W.; Reichert, K.; Sulkowski, U. Metal Tungstates and method of preparing them and their use. 5,874,056, 2/23/1999, 1999.

76. Hwang, D. W.; Kim, J.; Park, T. J.; Lee, J. S., Mg-doped WO3 as a novel photocatalyst for visible light-induced water splitting. *Catalysis Letters* **2002,** *80*, (1-2), 53-57.

77. Kubaschewski, O., *Iron - Binary Phase Diagrams*. Springer-Verlag: Berlin, 1982; p 185.

78. Powder Diffraction File. In; International Center on Diffraction Data, Newtown Square, PA.

79. Buitenhuis, E. T. Interactions between *Emiliania huxleyi* and the dissolved inorganic carbon system. Groningen University, Rotterdam, 2000.

80. Rioual, P.; Andrieu-Ponel, V.; Rietti-Shati, M.; Battarbee, R. W.; de Beaulieu, J.-L.; Cheddadi, R.; Reille, M.; Svobodova, H.; Shemesh, A., High Resolution record of climate stability in France during the last interglacial period. *Nature* **2001,** *413*, 293-296.

81. Stanley, S. M.; Hardie, L. A., Hypercalcification: Paleontology links plate tectonics and geochemistry to sedimentology. *GSA Today* **1999,** *9*, (2), 1-7.

82. Stoll, H. M.; Ziveri, P.; Geisen, M.; Probert, I.; Young, J. R., Potential and limitations of Sr/Ca ratios in coccolith carbonate: new perspectives from cultures and monospecific samples from sediments. *Phil. Trans. R. Soc. Lond. A* **2002,** *360*, 719-747.

83. Kolobanov, V. N.; Kamenskikh, I. A.; Mikhailin, V. V.; Shpinkov, I. N.; Spassky, D. A.; Zadneprovsky, B. I.; Potkin, L. I.; Zimmerer, G., Optical and luminescent properties of anisotropic tungstate crystals. *Nuclear Instruments and Methods in Physics Research A* **2002,** *486*, 496-503.

84. Hohl, A.; Wieder, T.; Aken, P. A. v.; Weirich, T. E.; Denninger, G.; Vidal, M.; Oswald, S.; Deneke, C.; Mayer, J.; Fuess, H., An interface clusters mixture model for the structure of amorphous silicon monoxide (SiO). *Journal of non-crystalline solids* **2003,** *320*, (1-3), 255-80.

85. Schulmeister, K.; Mader, W., TEM investigation on the structure of amorphous silicon monoxide. *Journal of non-crystalline solids* **2003,** *320*, (1-3), 143-150.

86. Weider, T., Research on the structure of amorphous SiO. In http://homepages.tu-darmstadt.de/~wieder/sio.html, 'Ed." 2001.

87. Hohl, A.; Wieder, T.; Joco, V.; Fuess, H., On the Structure of Amorphous Silicon Monoxide.

88. Kingery, W. D.; Bowen, H. K.; Uhlman, D. R., *Introduction to Ceramics*. 2nd Edition ed.; John Wiley & Sons: New York, 1976; p 394.

## LIST OF PUBLICATIONS

Three dimensional magnesia-based nanocrystal assemblies via low-temperature magnesiothermic reaction of diatom microshells. Y. Cai; S. Allan; K. Sandhage, F. Zalar. Journal of the American Ceramic Society (2005) [In Print].

Merging Biological Self-Assembly with Synthetic Chemical Tailoring: The Potential for 3-D Genetically-Engineered Micro/nano-devices (3-D GEMS). K. Sandhage, S. Allan, M. Dickerson, C. Gaddis, S. Shian, M. Weatherspoon, Y. Cai, G. Ahmad, M. Haluska, R. Snyder, R. Unocic, F. Zalar, Y. Zhang, R. Rapp, M. Hildebrand, B. Palenik. International Journal of Applied Ceramic Technology (2005) [In Print].

Shape-preserving chemical conversion of silica diatoms via displacement reaction. S. Allan (presentor), S. Shian, P. Graham, Y. Cai, K. Sandhage, M. Haluska, R. Snyder. 29$^{th}$ International Conference on Advanced Ceramics and Composites, Cocoa Beach, FL (2005).

Sol-gel synthesis on self-replicating single-cell scaffolds: applying complex chemistries to nature's 3-D nanostructured templates. M. Weatherspoon, S. Allan, E. Hunt, Y. Cai, K. Sandhage. Chemical Communications (Cambridge, United Kingdom) (2005), (5), 651-653.